EXPLOITING IMPULSIVE INPUTS FOR STABILIZATION OF UNDERACTUATED ROBOTIC SYSTEMS: THEORY AND EXPERIMENTS

By

Nilay Kant

A DISSERTATION

Submitted to
Michigan State University
in partial fulfillment of the requirements
for the degree of

Mechanical Engineering – Doctor of Philosophy

2020

ABSTRACT

EXPLOITING IMPULSIVE INPUTS FOR STABILIZATION OF UNDERACTUATED ROBOTIC SYSTEMS: THEORY AND EXPERIMENTS

By

Nilay Kant

Robots have become increasingly popular due to their ability to perform complex tasks and operate in unknown and hazardous environments. Many robotic systems are underactuated *i.e.*, they have fewer control inputs than their degrees-of-freedom (DOF). Common examples of underactuated robotic systems are legged robots such as bipeds, flying robots such as quadrotors, and swimming robots. Due to limited control authority, underactuated systems are prone to instability. This work includes impulsive inputs in the set of admissible controls to address several challenging control problems. It has already been shown that continuous-time approximation of impulsive inputs can be realized in physical hardware using high-gain feedback.

Stabilization of an equilibrium point is an important control problem for underactuated systems. The ability of the system to remain stable in the presence of disturbances depends on the size of the region of attraction of the stabilized equilibrium. The sum of squares and trajectory reversing methods are combined to generate a large estimate of the region of attraction. This estimate is then effectively enlarged by applying the impulse manifold method to stabilize equilibria from points lying outside the estimated region of attraction. Simulation results are provided for a three-DOF tiptoebot and experimental validation is carried out on a two-DOF pendubot. Impulsive inputs are also utilized to control the underactuated inertia-wheel pendulum (IWP). When subjected to impulsive inputs, the dynamics of the IWP can be described by algebraic equations. Optimal sequences of inputs are designed to achieve rest-to-rest maneuvers and the results are applied to the swing-up control problem. The novel problem of juggling a devil-stick using impulsive inputs is also investigated. Impulsive forces are applied to the stick intermittently and the impulse of the force and its point of application are modeled as inputs to the system. A dead-beat design for one of the inputs simplifies the control problem and results in a discrete linear time invariant system. To

achieve symmetric juggling, linear quadratic regulator (LQR) and model predictive control (MPC) based designs are proposed and validated through simulations.

A repetitive motion is described by closed orbits and therefore, stabilization of closed orbits is important for many applications such as bipedal walking and steady swimming. We first investigate the problem of energy-based orbital stabilization using continuous inputs and intermittent impulsive braking. The orbit is a manifold where the active generalized coordinates are fixed and the total mechanical energy of the system is equal to some desired value. Simulation and experimental results are provided for the tiptoebot and the rotary pendulum, respectively. The problem of orbital stabilization using virtual holonomic constraints (VHC) is also investigated. VHCs are enforced using a continuous controller which guarantees existence of closed orbits. A Poincaré section is constructed on the desired orbit and the orbit is stabilized using impulsive inputs which are applied intermittently when the system trajectory crosses the Poincaré section. This approach to orbital stabilization is general, and has lower complexity and computational cost than control designs proposed earlier.

This dissertation is lovingly dedicated to parents; my father Shri. Rajni Kant, and to my mother Smt. Kumari Jyotsna Kant as without their sacrifices, I would not have been able to accomplish this. I would also like to dedicate this work to Swami Vivekananda, an Indian yogi whose life, works and teachings have greatly transformed my life.

ACKNOWLEDGEMENTS

I would like to express my utmost gratitude to my PhD advisor, Dr. Ranjan Mukherjee, as his influence is as profound on this dissertation as it is in my life. In the ancient Indian civilization, education was not very formal as it is today and a student spent several years at a teacher's house to attain knowledge. The close association with the teacher resulted in a strong human relationship and the student mastered the most subtle aspect of a subject along with the desired human values. I am extremely lucky to have experienced such a process in the last five years, and this has been possible due to my association with Dr. Mukherjee. His office was always open during the day and I could simply walk inside anytime if I was stuck in a proof. There were countless occasions where both of us brainstormed together on a topic and hours just passed by. I vividly remember that he once showed me how to derive the Lagrange's equation on a notebook with minute details such as defining suitable coordinate system and drawing clear diagrams using a pencil. These instances may appear insignificant, but for me, they were life changing. It was only due to such involved and patient training, I became capable enough to accomplish this work. Despite over twenty five years of being a professor, Dr. Mukherjee unfailingly comes to office every weekend. Such hard work coupled with a genius mind inspired me throughout to push my boundaries and would forever continue to do so. I have experienced a transformation in the last five years - admirable traits of mine, if any, are due to Dr. Mukherjee, and the rest are my fault. Additionally, I am sincerely thankful to my PhD committee members Dr. Hassan Khalil, Dr. Vaibhav Srivastava and Dr. Gouming Zhu for their continued guidance, motivation and support. I am also very grateful to my lab mates; Sheryl, Mahmoud, Sanders, Connor, Krissy and Amer as their friendship did not let me miss my family back in India. I would also like to thank Mr. Roy Bailiff of the mechanical engineering department whose help in the machine shop ensured me to build my experimental setup.

I would like to express my gratitude to my parents are they have made several sacrifices to ensure that I get the best education possible. If it was not their conditional love and support, I

would not have come this far. I am also very thankful to my brother Dr. Kislay Kant as he has always set a high standard due to his achievements and conduct which has greatly inspired me to dream big and sincerely work towards it. I would also like to pay my salutations to my late grandparents Shri. Ramaeshward Prasad, Shri Hari Narayan Prasad, Smt. Rajkishori Devi and Smt. Gyneshwari Devi as their morals and life struggles were the source of inspiration in difficult times. Lastly, I would like to express my deepest gratitude to my wife Priyanka, as she was my strongest support throughout, and her love made me finish this journey with ease.

TABLE OF CONTENTS

LIST OF TABLES

LIST OF FIGURES

LIST OF ALGORITHMS

KEY TO SYMBOLS

g	acceleration due to gravity, (m/s^2)
ℓ_1	distance of center-of-mass of pendulum from the passive joint, (m)
ℓ_2	length of the pendulum, (m)
m_1	mass of the pendulum, (kg)
m_2	combined mass of the motor and the wheel, (kg)
t_0	initial time, (s)
t_i	instant of time at which the i-th impulsive torque, is applied, $i = 1, 2, \cdots, N$, (s)
t_f	final time, (s)
xy	inertially fixed Cartesian coordinate frame
I_1	mass moment of inertia of the pendulum about its center of mass, (kg.m^2)
I_2	mass moment of inertia of the wheel about its center of mass, (kg.m^2)
N	number of impulsive torques applied
θ	angular position of the pendulum, measured CCW with respect to the x axis, (rad)
ϕ	angular position of the wheel, measured CCW with respect to the pendulum, (rad)
$\dot{\theta}$	angular velocity of the pendulum, (rad/s)
$\dot{\phi}$	angular velocity of the wheel, (rad/s)
θ_i	value of θ at time t_i
$\dot{\theta}_i^-$	value of $\dot{\theta}$ immediately before application of impulsive torque at time t_i
$\dot{\theta}_i^+$	value of $\dot{\theta}$ immediately after application of impulsive torque at time t_i
$\dot{\phi}_i^-$	value of $\dot{\phi}$ immediately before application of impulsive torque at time t_i

$\dot{\phi}_i^+$ value of $\dot{\phi}$ immediately after application of impulsive torque at time t_i

τ torque applied by the motor on the wheel, (Nm)

τ_i impulsive torque applied at time t_i, (Nm)

τ_{hg} continuous-time implementation of impulsive torque using high-gain feedback, (Nm)

$\mathscr{I}_i$ angular impulse of impulsive torque τ_i applied at time t_i, (Nm-s)

$\mathscr{I}^N$ the N-dimensional vector $[\mathscr{I}_1\ \mathscr{I}_2\ \cdots\ \mathscr{I}_N]$

CHAPTER 1

INTRODUCTION

1.1 Motivation

A few decades ago, robots were primarily used for doing repetitive tasks in manufacturing lines and were supposed to work in risk-free and familiar environments. In recent times, there has been an increasing interest among engineers and scientists to create robotic systems which can operate in non-familiar environments. The applications of such robotic systems are immense as they can be used in application where human health is at risk such as in extra-terrestrial space explorations, rescue operations in the aftermath of disasters, construction in hostile environments such as deep sea etc. The new-age robots must be capable of locomotion and as a result, design, control and stability of robotic systems such as legged robots have gained popularity.

Legged robots fall under the category of underactuated systems as there is no actuation at the ground-foot contact point. While underactuation is inherent in legged robots, it is purposely introduced in bio-inspired models such as in the pendubot [4], acrobot [5], tiptoebot [6] etc. Several control objectives have been studied for underactuated robotic systems such as stabilization about an equilibrium configuration, swing-up to an equilibrium configuration corresponding to highest potential energy and generating stable repetitive motion. Since the dynamics of such systems are typically nonlinear, and due to the presence of fewer control inputs than their degree-of -freedom, their control design is often very challenging. Due to this reason, it is difficult to design general control methodologies for underactuated systems.

Impulsive inputs are theoretically modeled as Dirac-delta functions which causes discontinuous change in the velocity of a dynamical system. Impulsive forces occur naturally in several mechanical systems that experience impacts; for example walking [7] and hopping robots [8], juggling systems [9] etc. Modeling of such systems have been widely investigated in the framework of hybrid dynamical systems [10]. However, the use of impulsive inputs for control of systems, especially

underactuated mechanical systems have been rather limited. Few works that have previously proposed the use of impulsive inputs in control of some underactuated systems can be found in [11,12]. Impulsive inputs can be extremely useful where sudden change in system's configuration is required to attain certain control objective. This work presents several control problem where impulsive inputs are exploited to simplify the control of underactuated robotic systems; these problems are discussed next.

1.2 Estimating and Enlarging the Region of Attraction of Equilibria

Underactuated mechanical systems typically have multiple isolated equilibria and often the control design objective is to stabilize one of the equilibrium points that is unstable. Several methods have been proposed for stabilizing an equilibrium point for underactuated systems. These include the controlled Lagrangian method [13, 14], the interconnection and damping assignment passivity-based control (IDA-PBC) method [15], and the λ-method [16]. Other than these general methods, control designs have been proposed for stabilizing equilibrium points of specific underactuated systems such as the pendubot [17–19], acrobot [5,20], inverted pendulum on a cart [21], the reaction-wheel pendulum [1, 2], and the ball on beam system [22]. Irrespective of the control method used, a stabilized equilibrium of an underactuated system will have a finite region of attraction since the majority of all control designs cannot guarantee global stabilization. It is not trivial to obtain a non-conservative estimate of the region of attraction; and with a conservative estimate, it is only possible to guarantee stable behavior for small disturbances. To enable underactuated systems remain stable for large disturbances, we first present a method for obtaining a non-conservative estimate of the region of attraction. Then, the impulse manifold method (IMM) [23] is used to identify the region that lies outside this estimate and from where the equilibrium can be stabilized. A portion of this region may lie outside the region of attraction implying that the IMM can effectively enlarge the estimate of the region of attraction.

For underactuated systems, the IMM [23] uses impulsive inputs to move the configuration of the system from outside the estimated region of attraction to inside the region. Impulsive

inputs have been used for control of underactuated systems[1] [11, 12, 19, 24] and experimental investigations [23, 25] have relied on high-gain feedback for continuous approximation of the impulsive inputs. In an early work [26], high-gain control was used to force the trajectory of an acrobot into the region of attraction of a stabilizing controller. The limitations of this work are that the stabilizing controller must be pseudolinear [27] and the system cannot have more than one input. In [23], impulsive inputs were used to move the configuration of the system from a point lying immediately outside the region of attraction to inside the region; the boundary of the region was found iteratively by trial and error. Since it is not possible to determine the region of attraction for the general case, the IMM is used here in conjunction with an estimate of the region.

Both analytical and numerical methods have been used for estimating regions of attraction, [28–30], for example. The sum of squares (SOS) method uses a polynomial approximation of the system dynamics to maximize the estimate of the region of attraction [31–34]. It can also be used to enlarge the region of attraction by optimizing the controller in polynomial form [35,36]. Starting from an initial estimate, the trajectory reversing method enlarges an estimate using time-reversed trajectories of the system, [37–40], for example. The points obtained by time-reversal of trajectories lie on the surface of a larger estimate but it is challenging to obtain an analytical description of that surface in the general case.

Both the SOS method and the method of trajectory reversing have been used with the IMM in our earlier work [41, 42]. We combine the two methods in this work to enhance the applicability of the IMM. For a given order of the controller polynomial, the SOS method is first used to obtain the largest estimate of the region of attraction. Using this estimate as the initial estimate, a larger estimate is obtained using trajectory reversing. The generality of the combined method is illustrated using the example of the Tiptoebot - a three-link underactuated system with one passive joint. The result is notable since the trajectory reversing method has been illustrated in the literature using systems with two states only; the system considered here has six states. In addition to simulations, experimental validation is provided by stabilizing an equilibrium of a pendubot from a point lying

[1] Impulsive control of underactuated systems should be differentiated from control of underactuated systems subjected to impulsive disturbances.

outside the region of attraction estimated using the SOS and trajectory reversing methods. The impulse manifold passing through this point does not intersect the region of attraction estimated using the SOS method alone; this illustrates the usefulness of combining the SOS and trajectory reversing methods for application of the IMM.

1.3 Rest-to-Rest Maneuver of the Inertia Wheel Pendulum

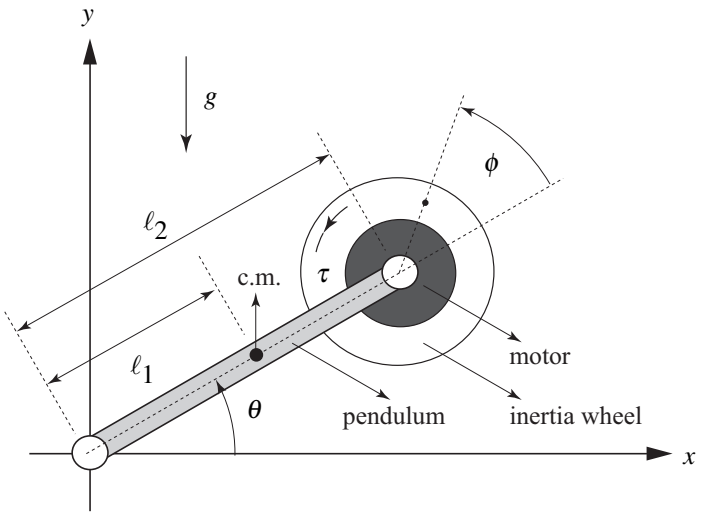

Figure 1.1: The inertia wheel pendulum.

The IWP is comprised of a simple pendulum and a motor mounted at its distal end; the motor drives a wheel - see Fig.1.1. The torque produced by the motor can be used to accelerate the wheel in both CW and CCW directions and the resulting reaction torque can be used to control the pendulum angle. The IWP bears similarity to the underactuated Acrobot [5] where in place of the the wheel, a link is driven by the motor. Since the wheel is symmetric, the angular displacement of the wheel is not included in the state-space representation and unlike the Acrobot, the only source of nonlinearity in the equation of motion is the gravity term. The IWP is an ideal candidate for impulsive control since the dynamics of the system can be described by simple algebraic equations: the effect of impulsive forces can be described by changes in the velocities of the system along the impulse manifold [23], and conservation of energy and conservation of wheel momentum describe the dynamics when no torque is applied by the motor.

For the IWP, stabilization of its upright posture and swing-up to this configuration have been investigated in the literature, [1, 2, 15, 43–46], for example. Some of the early work on the IWP can be found in [2] where a hybrid controller comprised of separate swing-up and balancing controllers was designed using energy methods. Swing-up and stabilization was achieved using a single controller using the IDA-PBC method [15, 43] and a global change of coordinates that converted the dynamics of the IWP into strict feedback form [1]. The IDA-PBC method based controllers [15, 43] and the globally stabilizing controller [1] result in high wheel velocities and actuator torques.

The swing-up problem of the IWP is a rest-to-rest maneuver between its lowest and highest potential energy configurations. In this work, we address the general problem of designing rest-to-rest maneuvers using a sequence of impulsive inputs. The use of impulsive inputs simplifies the dynamics of the IWP and permits the design of optimal sequences under some general assumptions. It is found that a sequence with an odd number of inputs is less optimal than the two adjacent sequences with even number of inputs. The high wheel velocities and/or actuator torques associated with some results in the literature [1, 15, 43], is explained using the analysis based on two impulsive inputs. An optimal sequence of impulsive inputs, implemented using high-gain feedback [23], is used for swing-up of the IWP; the simulations results show similarities with the energy-based methods in [2]. It is shown that an optimal input sequence can be designed to accommodate torque constraint of the actuator; this has not been discussed in earlier works.

1.4 Devil-Stick Juggling

A devil-stick is typically juggled using two hand sticks and several tricks can be performed depending on the proficiency of the juggler. Some of the common tricks are: *standard-idle*, *flip-idle*, *airplane-spin* or *propeller*, *top-only idle*, and *helicopter* [47]. The *top-only idle* is one of the simplest tricks and is the focus of this investigation; a video tutorial for learning this trick can be found in [48]. In top-only idle, intermittent forces are applied to the devil-stick. Since the devil-stick is never grasped, the juggling problem can be viewed as a non-prehensile manipulation

problem. If robots are to perform this trick, the motion of the end-effectors would have to be coordinated and controlled to apply the correct magnitude of impulsive forces to the devil-stick at appropriate locations. We do not focus on the end-effector motion control problem (see [49, 50] for application to ball juggling); instead, we investigate the magnitude and location of the forces needed to perform the *top-only idle* trick.

Many juggling tasks, including the *top-only idle* trick, involve intermittent application of impulsive forces and several researchers [51–55] have studied the controllability and stability of such systems. Although impulsive control of the devil-stick has not been investigated, the control problem associated with juggling of balls and air-hockey pucks has seen several solutions [9,56–58]. In all of these solutions, the object being juggled has been modeled as a point mass and its orientation is excluded from the dynamic model. In contrast, for devil-stick tricks such as *top-only idle*, the stick is shuffled between two symmetric configurations about the vertical; therefore, the orientation of the stick must be included in the dynamic model.

In earlier works on the devil-stick [59, 60], controllers have been designed for *airplane-spin* or *propeller*-type motion; a single hand-stick is used to rotate the devil-stick about a virtual horizontal axis using continuous-time inputs. The dynamics model and control design of *top-only idle* motion of the devil-stick has not appeared in the literature; to the best of our knowledge, it is presented here for the first time. It is assumed that impulsive forces are applied intermittently to the devil-stick and the control inputs are the impulse of the force and its point of application on the stick. The control inputs are designed to juggle the stick between two symmetric configurations about the vertical, starting from an arbitrary initial configuration.

1.5 Energy-Based Orbital Stabilization

For underactuated mechanical systems, the problem of stabilization of an equilibrium has been investigated widely, see [2, 13–16, 18, 21, 61], for example, and the references therein. In many applications, such as in legged locomotion, the system is required to undergo periodic motion; therefore, the control objective is to stabilize an orbit rather than an equilibrium. To achieve

repetitive motion, the virtual holonomic constraint (VHC) approach [3, 62, 63] has been proposed. The VHC imposes a set of geometric constraints on the generalized coordinates of the system and has been demonstrated in bipedal locomotion [7, 64]. Experimental validation of orbital stabilization using VHC can be found in [65, 66].

Orbital stabilization has also been used for swing-up control of underactuated systems with one passive degree-of-freedom (DOF). Some examples include two-DOF systems such as the pendubot [17], the acrobot [67], the reaction-wheel pendulum [68], inverted pendulum on a cart [69, 70], the rotary pendulum [71], and the three-DOF gymnast robot [72]. These controllers stabilize an orbit that include the equilibrium, which is typically unstable. The controllers are designed to gradually pump energy in and out of the system and converge the active DOFs to their desired configuration. Such control designs are typically based on a Lyapunov-like function that is comprised of terms involving positions and velocities of the active DOFs and the total mechanical energy of the system. The passivity property of the system is used to make the time derivative of the Lyapunov-like function negative semidefinite. A stability analysis is then carried out using LaSalle's invariance principle [73]; this typically results in certain restrictions on controller gains and initial conditions. In all of these prior works, the control strategies for orbital stabilization have been designed separately for individual systems. Although the structure of the Lyapunov-like function is identical, the stability analysis is different for each system due to the difference in the nature of their nonlinear dynamics. Despite the effectiveness of the individual controllers, a general methodology for energy-based orbital stabilization does not exist. We present a control strategy for n-DOF underactuated systems with one passive DOF based on continuous time inputs and impulsive braking.

A combination of continuous and impulsive inputs have been recently used for stabilization of a homoclinic orbits of two-DOF underactuated systems [74]. The current work provides a generalization of the theory to n-DOF systems and experimental validation. The main contributions of this work are as follows:

1. The control design is applicable to a class of underactuated systems which include a majority

of the commonly investigated underactuated systems.

2. The stability analysis is presented for the general case and it results in sufficient conditions that are not restrictive and can be checked for a given system.

3. Experimental validation is provided.

4. Impulsive braking is accomplished using a friction brake; this eliminates the need for high-gain feedback [23] which may result in actuator saturation.

1.6 Orbital Stabilization using Virtual Holonomic Constraints

For underactuated systems, Virtual Holonomic Constraint (VHC) based control designs have gained popularity due to their conceptual simplicity and applicability to control of repetitive motion. They have been used for stabilization of gaits in bipeds [64, 75–80], which undergo impacts, and trajectory control for systems with open kinematic chains that are not subjected to impacts [3, 62, 63, 65, 66, 81–84]. VHCs parameterize the active joint variables in terms of the passive joint variables and confine system trajectories to a constraint manifold [62]. To enforce the VHC, the constraint manifold has to be stabilized using feedback. Typically, a constraint manifold contains a dense set of periodic orbits and the choice of repetitive motion determines the specific orbit that has to be stabilized. To stabilize gaits in bipeds, for example, Grizzle et.al [64, 76, 79] enforced the VHC and periodic loss of energy due to ground-foot interaction was exploited for orbital stabilization.

A special class of underactuated systems are those with open kinematic chains and one passive DOF. For such systems, Shiriaev and collaborators [3, 65, 66] used VHC to select the desired orbit. For an n-DOF system, the $2n$ dimensional dynamics is linearized about the desired orbit; this results in a $2n-1$ dimensional system. A periodic Ricatti equation is then solved to design a time-varying controller that stabilizes the orbit. It should be noted that the control designs in [3, 65, 66] stabilize the orbit but do not enforce the VHC. A control scheme that enforces the VHC and simultaneously stabilizes the orbit was recently proposed in [63]. The key idea is that the VHC is made time-

varying using a scalar parameter which is controlled via feedback. The stabilization problem involves solving a periodic Ricatti equation; however, unlike [3,65,66], where the dimension of the system is $2n-1$, the dimension of the system in [63] is always three. For systems with more than two DOF, the method in [63] reduces the computational complexity of control implementation. Also, by enforcing the VHC, it improves control over transient characteristics of the trajectory [85]. Similar to [63,85], we design a continuous controller with the objective of enforcing the VHC and stabilizing the constraint manifold. We then design impulsive inputs that work in tandem with the continuous inputs to stabilize a desired periodic orbit on the constraint manifold. Compared to the methods proposed earlier [3, 63, 65, 66], where periodic Ricatti equations have to be solved, our method has lower computational cost and complexity. Since impulsive inputs are used to control the Poincaré map, the dynamics of the closed-loop system can be described by the Impulse Controlled Poincaré Map (ICPM). The simplicity and generality of the ICPM approach to orbital stabilization is demonstrated using the examples of the 2-DOF cart-pendulum and the 3-DOF tiptoebot.

CHAPTER 2

ESTIMATION OF THE REGION OF ATTRACTION OF EQUILIBRIA AND ITS ENLARGEMENT USING IMPULSIVE INPUTS

2.1 Introduction

Stabilization of an equilibrium point is an important control problem for underactuated systems. For a given stabilizing controller, the ability of the system to remain stable in the presence of disturbances depends on the size of the region of attraction of the stabilized equilibrium. The sum of squares (SOS) and trajectory reversing methods are combined together to generate a large estimate of the region of attraction. Then, this estimate is effectively enlarged by applying the impulse manifold method (IMM), which can stabilize equilibria from points lying outside the estimated region of attraction. The IMM and the SOS method are reviewed in section 2.2. The Tiptoebot is introduced in section 2.3 and the IMM is used to stabilize its equilibrium from a point lying outside the region of attraction estimated by the SOS method. A convex hull algorithm for estimating the region of attraction using trajectory reversing is presented in section 2.4. The benefit of using the SOS method, the convex hull algorithm, and IMM together is illustrated using the example of the Tiptoebot in section 2.5. Experimental results are presented in section 2.6.

2.2 Background

2.2.1 The Impulse Manifold Method

For an n degree-of-freedom dynamical system, Lagrange's equations have the form:

$$M(q)\ddot{q} + H(q,\dot{q}) = T \tag{2.2.1}$$

where $q \in R^n$ and $T \in R^n$ represent the vectors of generalized coordinates and generalized forces; $M(q) \in R^{n\times n}$ denotes the generalized mass matrix; and $H(q,\dot{q}) \in R^n$ denotes the vector of centrifugal, Coriolis, gravitational and friction forces. If the system is underactuated with m active and

$(n-m)$ passive degrees-of-freedom, $m < n$, (2.2.1) can be rewritten in the form:

$$\begin{bmatrix} M_{11}(q) & M_{12}(q) \\ M_{12}^T(q) & M_{22}(q) \end{bmatrix} \begin{bmatrix} \ddot{q}_1 \\ \ddot{q}_2 \end{bmatrix} + \begin{bmatrix} h_1(q,\dot{q}) \\ h_2(q,\dot{q}) \end{bmatrix} = \begin{bmatrix} 0 \\ u \end{bmatrix} \tag{2.2.2}$$

where $q = (q_1^T, q_2^T)^T$, and $q_1 \in R^{(n-m)}$ and $q_2 \in R^m$ denote the generalized coordinates corresponding to the passive and active degrees-of-freedom, respectively, and $u \in R^m$ is the vector of control inputs.

We assume that $(q,\dot{q}) = (0,0)$ is an equilibrium point of the unforced system and $u = u_s$ is a stabilizing controller. If $\mathscr{R}_{\mathrm{A}}$ is the region of attraction of the equilibrium with $u = u_s$, the equilibrium cannot be stabilized from configurations that lie outside $\mathscr{R}_{\mathrm{A}}$. However, it may be possible to stabilize the equilibrium after moving the configuration of the system from outside $\mathscr{R}_{\mathrm{A}}$ to inside $\mathscr{R}_{\mathrm{A}}$ using the Impulse Manifold Method (IMM) [23]. In the IMM, impulsive inputs are applied to the active degrees-of-freedom. Ideal impulsive inputs cause no change in the generalized coordinates but result in discontinuous changes in both active and passive generalized velocities. These changes can be computed from the following equation which is obtained by integration of (2.2.2) over the infinitesimal interval of time Δt, during which the impulsive inputs act [86]:

$$\begin{bmatrix} M_{11} & M_{12} \\ M_{12}^T & M_{22} \end{bmatrix} \begin{bmatrix} \Delta\dot{q}_1 \\ \Delta\dot{q}_2 \end{bmatrix} = \begin{bmatrix} 0 \\ I \end{bmatrix}, \quad I \triangleq \int_0^{\Delta t} u\, dt \tag{2.2.3}$$

In the above equation, $I \in R^m$ is the vector of impulses, and the velocity jumps, $\Delta\dot{q}_1$ and $\Delta\dot{q}_2$, are defined as

$$\Delta\dot{q}_1 \triangleq (\dot{q}_1^+ - \dot{q}_1^-), \qquad \Delta\dot{q}_2 \triangleq (\dot{q}_2^+ - \dot{q}_2^-)$$

where $\dot{q}^-$ and $\dot{q}^+$ are the generalized velocities immediately before and after application of the impulsive inputs. Due to the underactuated nature of the system, the discontinuous changes in the velocities of the passive coordinates are dependent on those of the active coordinates; this dependence is obtained from (2.2.3) as follows:

$$(\dot{q}_1^+ - \dot{q}_1^-) = -M_{11}^{-1} M_{12} (\dot{q}_2^+ - \dot{q}_2^-) \tag{2.2.4}$$

In the n-dimensional velocity space, the impulse manifold is the m-dimensional manifold represented by (2.2.4). It was stated earlier that the generalized coordinates do not change under the application of an impulse. Hence, for a fixed value of q, the impulse manifold passing through the point $(\dot{q}_1^-, \dot{q}_2^-)$ is defined by the set

$$\mathscr{I}_{\mathrm{M}}(\dot{q}_1^-, \dot{q}_2^-) = \{\dot{q}_1^+, \dot{q}_2^+ \mid (\dot{q}_1^+ - \dot{q}_1^-) = -M_{11}^{-1} M_{12} (\dot{q}_2^+ - \dot{q}_2^-)\} \tag{2.2.5}$$

The IMM is explained with the help of Fig.2.1. The region of attraction $\mathscr{R}_{\mathrm{A}}$ is shown in Fig.2.1 (a). An arbitrary point outside $\mathscr{R}_{\mathrm{A}}$ is denoted by $(q^*, \dot{q}^*)$. For $q = q^*$, the slice of $\mathscr{R}_{\mathrm{A}}$ in the n-dimensional velocity space is denoted by $\widetilde{\mathscr{R}}_{\mathrm{A}}(q^*)$ and is shown in Fig.2.1 (b). Since $(q^*, \dot{q}^*)$ lies outside $\mathscr{R}_{\mathrm{A}}$, the point $\dot{q}^*$ lies outside $\widetilde{\mathscr{R}}_{\mathrm{A}}(q^*)$. The m-dimensional impulse manifold $\mathscr{I}_{\mathrm{M}}(\dot{q}^*)$ is depicted by the plane in Fig.2.1 (c); its intersection with $\widetilde{\mathscr{R}}_{\mathrm{A}}(q^*)$ is shown by the hatched region and is mathematically defined by the set

$$\widehat{\mathscr{R}}_{\mathrm{A}}(q^*, \dot{q}^*) = \mathscr{I}_{\mathrm{M}}(\dot{q}^*) \cap \widetilde{\mathscr{R}}_{\mathrm{A}}(q^*) \tag{2.2.6}$$

Impulsive inputs can be applied to change the velocity of the system from $\dot{q}^*$ to any other point (desired velocity) on the impulse manifold. However, to move the configuration of the system to a point inside $\mathscr{R}_{\mathrm{A}}$, the desired velocity should be chosen to lie in $\widehat{\mathscr{R}}_{\mathrm{A}}(q^*, \dot{q}^*)$. For the IMM to be applicable, $\widehat{\mathscr{R}}_{\mathrm{A}}(q^*, \dot{q}^*)$ should not be a null set and the desired velocity should be chosen such that the magnitude of the impulse I does not violate actuator constraints.

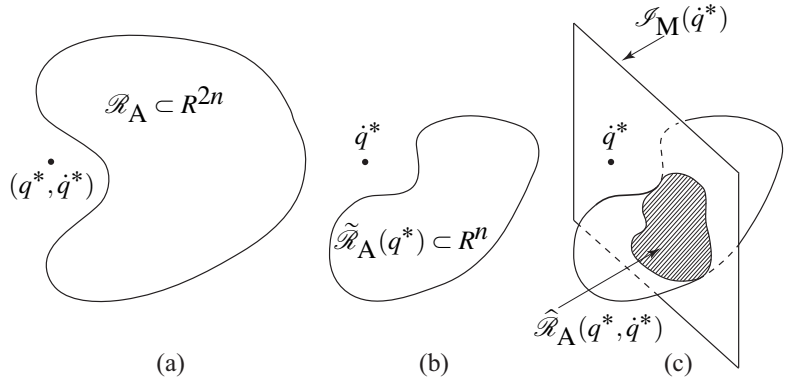

Figure 2.1: (a) $\mathscr{R}_{\mathrm{A}}$ and a point $(q^*, \dot{q}^*)$ that lies outside $\mathscr{R}_{\mathrm{A}}$, (b) $\widetilde{\mathscr{R}}_{\mathrm{A}}(q^*)$ and the point $\dot{q}^*$, (c) $\mathscr{I}_{\mathrm{M}}(\dot{q}^*)$, $\widetilde{\mathscr{R}}_{\mathrm{A}}(q^*)$ and $\widehat{\mathscr{R}}_{\mathrm{A}}(q^*, \dot{q}^*)$.

Ideal impulsive inputs, which are Dirac-delta functions, cannot be implemented in real physical systems. For an underactuated system of the form as in (2.2.2), impulsive inputs can be implemented using high-gain feedback [23]; the control law is given by[1]

$$u = u_{hg} = [C^T M^{-1} C]^{-1} \left[C^T M^{-1} H + \frac{1}{\mu} \Lambda \left(\dot{q}_2^{des} - \dot{q}_2 \right) \right] \tag{2.2.7}$$

where $C \in R^{n \times m}$ is the matrix $C = \begin{bmatrix} 0 & E \end{bmatrix}^T$, $E \in R^{m \times m}$ is the identity matrix, $\dot{q}_2^{des}$ is the vector of desired velocities of the active joints, $\Lambda \triangleq diag \begin{bmatrix} \lambda_1 & \lambda_2 & \cdots & \lambda_m \end{bmatrix}$, where λ_i, $i = 1, 2, \cdots, m$ are positive numbers, and μ is a small positive number.

In general, an exact determination of $\mathscr{R}_A$ is not possible and an estimate of the region of attraction $\mathscr{R}_A^e$, $\mathscr{R}_A^e \subset \mathscr{R}_A$, has to be used. As we replace $\mathscr{R}_A$ with $\mathscr{R}_A^e$, we define $\widetilde{\mathscr{R}}_A^e$ and $\widehat{\mathscr{R}}_A^e$ in the same manner that $\widetilde{\mathscr{R}}_A$ and $\widehat{\mathscr{R}}_A$ were defined in relation to $\mathscr{R}_A$.

From the discussion in this section it is obvious that the IMM will be more effective for larger $\mathscr{R}_A^e$. When applicable, the IMM will effectively enlarge the $\mathscr{R}_{\mathrm{A}}^e$ of the equilibrium.

2.2.2 The Sum of Squares Method

The simplest way to obtain an $\mathscr{R}_A^e$ is through linearization [73]: the dynamics of the closed-loop underactuated system in (2.2.2) is first represented in state-space form

$$\dot{x} = f[x, u = u_s(x)] = g(x) \tag{2.2.8}$$

where $x = (q^T, \dot{q}^T)^T$ and $u_s(x)$ is a stabilizing controller. The $\mathscr{R}_A^e$ of the asymptotically stable equilibrium $x = 0$ can be defined with the help of the quadratic Lyapunov function $V_0(x)$ as follows

$$\mathscr{R}_A^e = \{x \mid V_0(x) \leqslant c\} \triangleq \Omega_{lin}, \qquad V_0(x) \triangleq x^T P x \tag{2.2.9}$$

where P is the positive definite matrix obtained by solving the Lyapunov equation

$$PA + A^T P = -Q, \qquad A \triangleq \left[\frac{\partial g}{\partial x} \right]_{x=0}, \quad Q = Q^T > 0$$

[1]The high-gain feedback in [23] has been modified here for its applicability to systems with more than one active joint: the diagonal matrix Λ has been introduced to provide flexibility in choosing different gains for the different active joints. It can be easily shown that this modification does not affect the continuous approximation of the impulsive inputs.

and c is the largest number that satisfies

$$\{V_0(x) \leqslant c\} \subseteq \{\dot{V}_0(x) \leqslant 0\}$$

The Sum of Squares (SOS) method [31] automates the process of finding a Lyapunov function using numerical tools from convex optimization. Subsequently, an $\mathscr{R}_A^e$ can be obtained by solving the following optimization problem [36]:

$$\textbf{maximize } \rho$$

$$\text{subject to } \begin{cases} V(x) & \text{is SOS} \\ L(x) & \text{is SOS} \\ -\dot{V}(x) + L(x)(V(x) - \rho) & \text{is SOS} \end{cases}$$

where $V(x)$ is the Lyapunov function and $L(x)$ is a polynomial multiplier. The decision variables in this optimization problem are $L(x)$, $V(x)$ and ρ. The third constraint guarantees

$$\{V(x) \leqslant \rho\} \subseteq \{\dot{V}(x) \leqslant 0\}$$

and therefore an estimate of the region of attraction is

$$\mathscr{R}_A^e = \{x \mid V(x) \leqslant \rho\} \triangleq \Omega_{sos} \tag{2.2.10}$$

In the above optimization problem, $\mathscr{R}_A^e$ is maximized for a pre-determined stabilizing controller. The controller can also be optimized to further enlarge $\mathscr{R}_A^e$. The controller $u(x)$ is introduced as another decision variable in the third constraint of the SOS optimization problem:

$$\dot{V}(x) = \frac{\partial V}{\partial x} f[x, u(x)]$$

This non-convex optimization problem was studied in [35, 36], where the following steps are performed sequentially and repeatedly till no further enlargement of $\mathscr{R}_A^e$ is observed:

- $V(x)$ is fixed; $L(x)$ and $u(x)$ are varied to maximize ρ
- $L(x)$ and $u(x)$ are fixed; $V(x)$ is varied to maximize ρ

The SOS algorithm requires an initial guess of the Lyapunov function $V(x)$. If this initial guess is chosen to be $V_0(x)$ in (2.2.9), we can guarantee

$$\Omega_{sos} \supseteq \Omega_{lin}$$

which implies that the SOS method can improve upon the $\mathscr{R}_A^e$ obtained through linearization.

2.3 Enlarging the Region of Attraction Using SOS and IMM

2.3.1 An Illustrative Example

From our discussion in section 2.2 it is clear that an $\mathscr{R}_A^e$ can be obtained using the SOS method and that this estimate can be effectively enlarged using the IMM. In this section we demonstrate the effective enlargement of the $\mathscr{R}_A^e$ for a three-link underactuated system with two active joints and one passive joint. A majority of articulated underactuated systems that have been considered in the literature have two degrees-of-freedom with one passive joint; examples include the pendubot, the

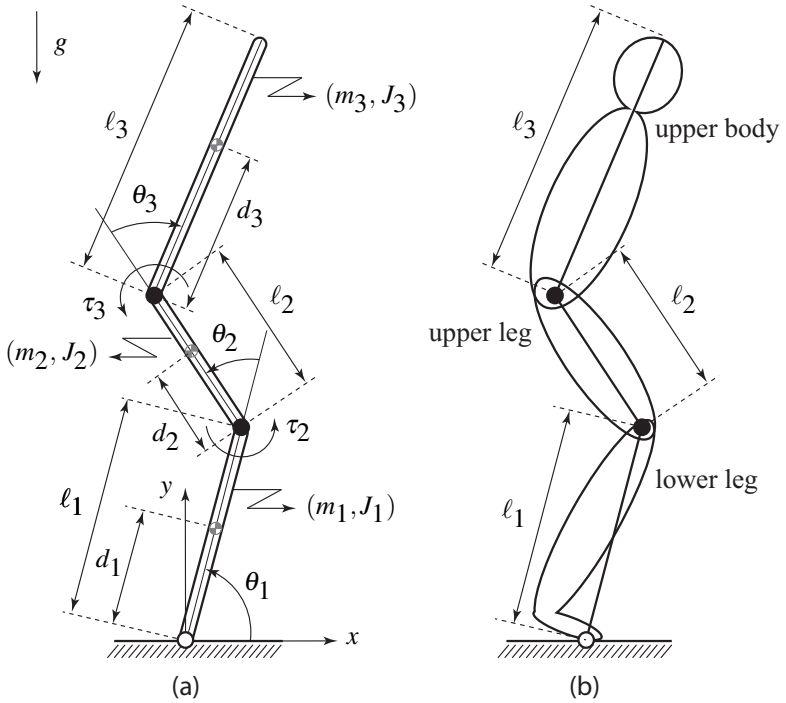

Figure 2.2: (a) The Tiptoebot - a three-link underactuated system with two active joints at the hip and knee, and one passive joint at the toe (b) a simple model of a human balancing on the tip of the toe.

acrobot, the rotary pendulum, inverted pendulum on a cart, etc. The three-link system is purposely chosen to demonstrate the applicability of the method to more complex systems.

Consider the three-link underactuated system[2] in Fig 2.2 (a). We have christened it the Tiptoebot since it models a human balancing on the tip of its toe - see Fig 2.2 (b). The three links are analogous to the lower leg, the upper leg, and the upper body comprised of the torso and head. The knee joint connecting the upper and lower legs, and the hip joint connecting the upper body and upper leg are actuated; the torques applied by the actuators in these joints are assumed to be positive in the counter-clockwise direction and are denoted by τ_2 and τ_3. The toe provides a simple point of support and is modeled as a passive joint. The lower leg, upper leg, and upper body have link lengths ℓ_1, ℓ_2 and ℓ_3; their center-of-masses are located at distances d_1, d_2 and d_3 as shown in Fig.2.2 (a); their mass and mass moments of inertia about their individual center-of-mass are denoted by (m_1,J_1), (m_2,J_2) and (m_3,J_3). The joint angles of the links are measured positive in the counter-clockwise direction and are denoted by θ_1, θ_2 and θ_3; θ_1 is measured relative to the x-axis whereas θ_2 and θ_3 are measured relative to the second and third links.

Table 2.1: Kinematic and Dynamic Parameters for Tiptoebot in SI units

m_1	m_2	m_3	ℓ_1	ℓ_2	ℓ_3
0.20	0.20	0.30	0.20	0.20	0.30
J_1	J_2	J_3	d_1	d_2	d_3
6.66×10^{-4}	6.66×10^{-4}	15.0×10^{-4}	0.10	0.10	0.15

The kinematic and dynamic parameters of the Tiptoebot in Fig.2.2 are provided in Table 6.1. For these set of parameters, the equations of motion are of the form given by (2.2.2), where $n=3$, $m=2$ and $u=(\tau_2\ \tau_3)^T$. The vertically upright posture or configuration $(\theta_1,\theta_2,\theta_3,\dot\theta_1,\dot\theta_2,\dot\theta_3) = (\pi/2,0,0,0,0,0)$ is the desired equilibrium and hence $q_1=(\theta_1-\pi/2)$, $q_2=(\theta_2\ \theta_3)^T$. The matrices M_{11}, M_{12}, M_{22}, h_1 and h_2, which can be described as functions of θ_k, $\dot\theta_k$, $k=1,2,3$, are

[2]This system is a special case of the N-link system considered in [87].

provided below:

$$M_{11} = 0.018\,C_{23} + 0.032\,C_2 + 0.018\,C_3 + 0.046$$

$$M_{12} = \begin{bmatrix} 0.009\,C_{23} + 0.016\,C_2 + 0.018\,C_3 + 0.023 \\ 0.009\,C_{23} + 0.018\,C_3 + 0.009 \end{bmatrix}^T$$

$$M_{22} = \begin{bmatrix} 0.018\,C_3 + 0.023 & 0.009\,C_3 + 0.009 \\ 0.009\,C_3 + 0.009 & 0.009 \end{bmatrix}$$

$$\begin{aligned} h_1 &= 0.100\,\dot{\theta}_1 + 0.441\,C_{123} + 0.784\,C_{12} + 1.177\,C_1 - 0.016\,\dot{\theta}_2^2\,S_2 - 0.009\,\dot{\theta}_3^2\,S_3 \\ &\quad - 0.009(\dot{\theta}_2 + \dot{\theta}_3)^2\,S_{23} - 0.018\,\dot{\theta}_1(\dot{\theta}_2 + \dot{\theta}_3)\,S_{23} - 0.018\,(\dot{\theta}_1 + \dot{\theta}_2)\dot{\theta}_3\,S_3 - 0.032\,\dot{\theta}_1\,\dot{\theta}_2\,S_2 \\ h_2 &\triangleq \begin{bmatrix} h_{21} & h_{22} \end{bmatrix}^T \\ h_{21} &= 0.100\,\dot{\theta}_2 + 0.441\,C_{123} + 0.784\,C_{12} + 0.016\,\dot{\theta}_1^2\,S_2 - 0.009\,\dot{\theta}_3^2\,S_3 + 0.009\,\dot{\theta}_1^2\,S_{23} \\ &\quad - 0.018(\dot{\theta}_1 + \dot{\theta}_2)\,\dot{\theta}_3\,S_3 \\ h_{22} &= 0.100\,\dot{\theta}_3 + 0.441\,C_{123} + 0.009\,\dot{\theta}_1^2\,S_{23} + 0.009(\dot{\theta}_1 + \dot{\theta}_2)^2\,S_3 \end{aligned}$$

where S_i and C_i denote $\sin\theta_i$ and $\cos\theta_i$, S_{ij} and C_{ij} denote $\sin(\theta_i+\theta_j)$ and $\cos(\theta_i+\theta_j)$, and C_{ijk} denotes $\cos(\theta_i+\theta_j+\theta_k)$. We assumed the presence of viscous friction in the joints of the Tiptoebot. This accounts for the terms linearly proportional to the angular velocities in the expressions for h_1, h_{21} and h_{22}.

The stabilizing controller u_s in (2.2.8) was obtained through linearization by placing the poles of the closed-loop system at -8, -3, -2, -1, -0.7, -0.4. The controller has the form $u_s = [\tau_2\ \tau_3]^T$ where

$$\begin{aligned} \tau_2 &= -10.204\,(\theta_1 - \pi/2) - 5.789\,\theta_2 - 2.140\,\theta_3 - 2.114\,\dot{\theta}_1 - 1.144\,\dot{\theta}_2 - 0.496\,\dot{\theta}_3 \\ \tau_3 &= -7.996\,(\theta_1 - \pi/2) - 4.284\,\theta_2 - 1.878\,\theta_3 - 1.632\,\dot{\theta}_1 - 0.974\,\dot{\theta}_2 - 0.295\,\dot{\theta}_3 \end{aligned}$$

The Lyapunov function V_0 was obtained using (2.2.9); the matrices P and Q are

$$P = \begin{bmatrix} 5271.9 & 2668.5 & 973.5 & 1054.4 & 626.9 & 241.7 \\ 2668.5 & 1350.7 & 492.7 & 533.75 & 317.3 & 122.3 \\ 973.55 & 492.80 & 179.8 & 194.73 & 115.7 & 44.65 \\ 1054.4 & 533.75 & 194.7 & 210.91 & 125.3 & 48.35 \\ 626.90 & 317.33 & 115.7 & 125.39 & 74.55 & 28.75 \\ 241.75 & 122.37 & 44.65 & 48.359 & 28.75 & 11.09 \end{bmatrix}, \; Q = 0.01 \times diag \begin{bmatrix} 3 & 3 & 3 & 1 & 1 & 1 \end{bmatrix}$$

The estimated region of attraction Ω_{lin} in (2.2.9) was defined by the value of $c = 0.020$; this value was determined by following the steps [73] given below:

1. Find a set of points α_i, $i = 1, 2, \cdots, M$, where $\dot{V}(\alpha_i) = 0$.

2. Choose $c < \bar{c} = \min_i V(\alpha_i)$.

The SOS method was used to improve upon the estimate Ω_{lin}. By fixing $V = V_0$, L and u were varied to maximize ρ and determine Ω_{sos} in (2.2.10). The input u was chosen to be a first-order polynomial of the states and the maximum value of ρ was found to be 0.044. The SOS controller was obtained as follows:

$$\tau_2 = -3.866\,(\theta_1 - \pi/2) - 2.603\,\theta_2 - 1.025\,\theta_3 - 0.898\,\dot{\theta}_1 - 0.417\,\dot{\theta}_2 - 0.259\,\dot{\theta}_3$$

$$\tau_3 = 10.157\,(\theta_1 - \pi/2) + 4.887\,\theta_2 + 1.410\,\theta_3 + 1.942\,\dot{\theta}_1 + 1.156\,\dot{\theta}_2 + 0.476\,\dot{\theta}_3$$

2.3.2 Simulation Results

To demonstrate the enlargement of the $\mathscr{R}_A^e = \Omega_{sos}$ using the IMM, we consider the following initial configuration that lies outside Ω_{sos}:

$$x = \begin{bmatrix} q^{*T} & \dot{q}^{*T} \end{bmatrix}^T = \begin{bmatrix} 0.0 & 0.0 & 0.0 & 0.00 & 0.00 & 0.21 \end{bmatrix}^T \tag{2.3.1}$$

For this configuration, it can be verified that $V_0(x) = 0.48 > \rho = 0.044$. Following the discussion in section 2.2.1, the slices $\widetilde{\mathscr{R}}_{\mathrm{A}}^e(q^* = 0)$ corresponding to Ω_{lin} and Ω_{sos} can be expressed as

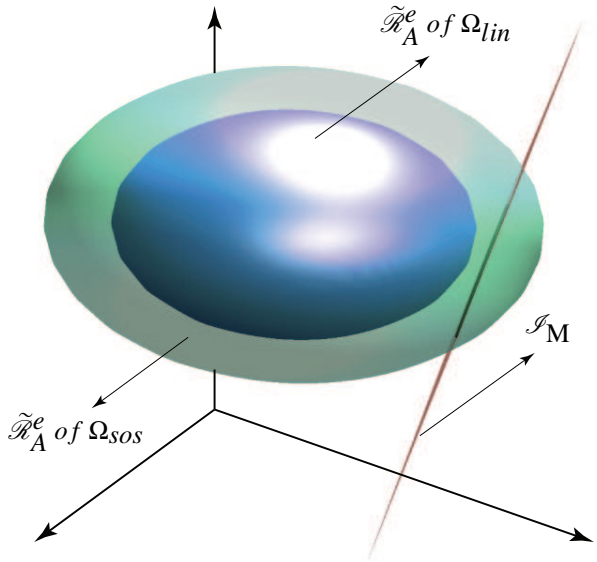

Figure 2.3: Slices of Ω_{sos} and Ω_{lin}, and their intersection with the impulse manifold, $\mathscr{I}_M$. A transformed coordinate system is used for better visualization.

$V_0\,|_{q=q^*=0} \leqslant c$ and $V_0\,|_{q=q^*=0} \leqslant \rho$, respectively. Both these slices are ellipsoids and are shown in Fig.2.3; the coordinates were scaled and transformed for better visualization. The impulse manifold $\mathscr{I}_M(0,0,0.21)$ is a plane (two-dimensional manifold) in the three-dimensional velocity space; it is shown in Fig.2.3 in the transformed coordinates and mathematically described by the relation:

$$\dot{q}_1 + 0.583\,\dot{q}_2 + 0.236\,\dot{q}_3 - 0.049 = 0 \tag{2.3.2}$$

It can be seen from Fig.2.3 that the impulse manifold intersects the slice $\tilde{\mathscr{R}}^e_A(q^* = 0) = \{\dot{q} \mid V_0(0,\dot{q}) < \rho\}$ obtained using the SOS method but not the slice $\tilde{\mathscr{R}}^e_A(q^* = 0) = \{\dot{q} \mid V_0(0,\dot{q}) < c\}$ obtained using linearization. Consequently, the set $\hat{\mathscr{R}}^e_A$ in (2.2.6) obtained using the SOS method is non-empty whereas that obtained using linearization is a null set; this illustrates the benefit of using a larger $\mathscr{R}^e_A$ in terms of applicability of the IMM.

The $\hat{\mathscr{R}}^e_A$ obtained using the SOS method is an ellipse in the three-dimensional velocity space; it is shown together with the impulse manifold $\mathscr{I}_M$ in Fig.2.4 in the original coordinates. To take the configuration of the Tiptoebot from outside $\mathscr{R}^e_A$ to inside $\mathscr{R}^e_A$, we choose the following desired velocity configuration that lies in the interior of $\hat{\mathscr{R}}^e_A$:

$$\begin{bmatrix} \dot{q}_1 & \dot{q}_2^T \end{bmatrix} = \begin{bmatrix} 2.36 & -4.04 & 0.16 \end{bmatrix} \tag{2.3.3}$$

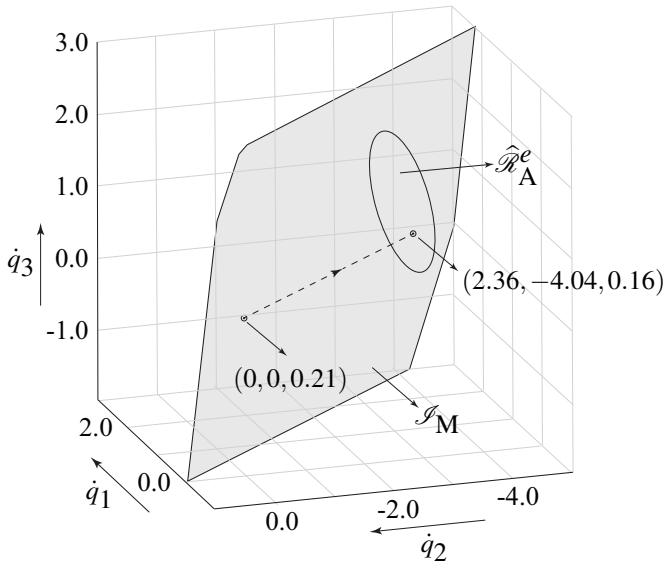

Figure 2.4: Intersection of the slice of Ω_{sos} with the impulse manifold $\mathscr{I}_{\mathrm{M}}$ in the original coordinates; the intersection set $\widehat{\mathscr{R}}^e_{\mathrm{A}}$ is an ellipse.

The desired effect of the impulsive inputs is shown by the dotted line joining the initial and desired velocity configurations, both of which lie on $\mathscr{I}_{\mathrm{M}}$ - see Fig.2.4. To implement the IMM, the high-gain feedback in (2.2.7) was used with $\dot{q}_2^{des} = \dot{q}_2$ in (2.3.3), $\mu = 0.0004$, $\lambda_1 = 10$ and $\lambda_2 = 1$; the results are shown in Fig.2.5. Figure 2.5 plots the joint angles, their velocities, and the control inputs with time. The high-gain controller is active over $t \in [0, 0.004]$; its effect is shown using a dilated time scale. It can be seen that the change in the joint angles are negligible but there are significant changes in the joint velocities. At $t = 0.004$ when $\dot{q}_2 \approx \dot{q}_2^{des}$, the high-gain controller is switched off and the stabilizing controller is switched on; at this time, the system configuration is inside $\mathscr{R}^e_{\mathrm{A}}$ and therefore the equilibrium can be stabilized. The stabilization of the equilibrium after $t > 0.004$ is shown using a normal time scale.

The high-gain feedback was based on $\mu = 0.0004$. The change in the joint angles were negligible, of the order of 0.01 rad. A larger value of μ could be used to reduce the magnitude of the control inputs but it would result in larger changes in the joint angles. The computation of $\widehat{\mathscr{R}}^e_{\mathrm{A}}$ is based on the assumption that there is no change in the joint angles and therefore a small value of μ is necessary to ensure the applicability of the IMM.

For the general case, if δ denotes the small change in the joint angles due to high-gain feedback,

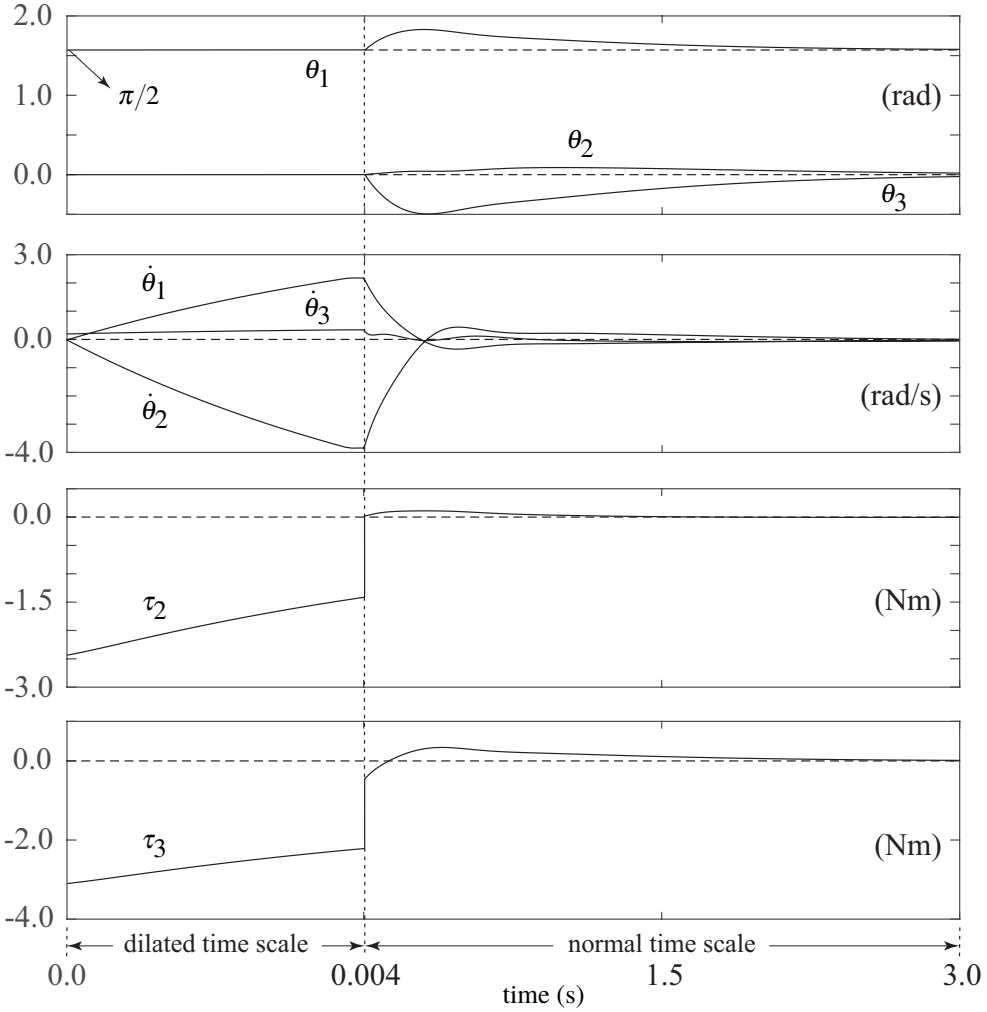

Figure 2.5: Effective enlargement of $\mathscr{R}_A^e$ using SOS-IMM: Plot of joint angles, their velocities, and control inputs with time for stabilization of the Tiptoebot from the initial configuration given by (2.3.1). The effect of high-gain feedback is shown using a dilated time scale; the effect of the stabilizing controller is shown using a normal time scale.

we should ensure that the desired velocity $\dot{q}_2^{des}$, which was chosen to lie in the interior of $\widehat{\mathscr{R}}_{\mathrm{A}}(q^*, \dot{q}^*)$, also lies in the interior of $\widehat{\mathscr{R}}_{\mathrm{A}}(q^* + \delta, \dot{q}^*)$. To this end, the desired velocity $\dot{q}_2^{des}$ should be chosen sufficiently far from the boundary of $\widehat{\mathscr{R}}_{\mathrm{A}}(q^*, \dot{q}^*)$.

There is significant flexibility in the choice of the desired velocity $\dot{q}_2^{des}$. This choice can be used judiciously to minimize the overall control effort or some other cost function.

It was mentioned in section 2.2.1 that the IMM will be more effective for larger $\mathscr{R}_A^e$. To this end, we present an algorithm in the next section for obtaining large estimates of $\mathscr{R}_A^e$; the algorithm

is based on the method of trajectory reversing [37].

2.4 Algorithm for Computing $\mathscr{R}_{\mathbf{A}}^{e}$ Using the Method of Trajectory Reversing

2.4.1 Definitions

For the closed-loop system in (2.2.8), an $\mathscr{R}_A^e$ of $x = 0$ is given by Ω_{lin} in (2.2.9) and Ω_{sos} in (2.2.10). The method of trajectory reversing [37] can be used to obtain a larger $\mathscr{R}_A^e$ starting from a conservative $\mathscr{R}_A^e$ such as Ω_{lin} or Ω_{sos}. The larger $\mathscr{R}_A^e$ is a convergent sequence of simply connected domains generated by backward integration from a discrete set of points on the boundary of the conservative estimate. In the literature, the method of trajectory reversing has been used to obtain $\mathscr{R}_A^e$ for example systems described by two state variables. Here, we present an algorithm [42] that has been shown to provide larger estimates for the two-state systems considered in the literature; additionally, it will be used to obtain an $\mathscr{R}_A^e$ for the Tiptoebot, whose dynamics is described six state variables. To the best of our knowledge, estimation of the region of attraction using the method of trajectory reversing has not been reported in the literature for systems with more than two states. Before we present the algorithm, we present the following definitions:

Definition 1. *Convex Hull: A convex hull of a set of points $S = \{x_1, x_2, \cdots, x_N\}$ in R^n, denoted by Conv(S), is the smallest convex set that contains all the points.*

A convex hull can be mathematically represented by a set of equations and inequalities. In the two-dimensional plane, a convex hull is described by line segments which can be represented by equations of the lines and inequalities based on their lengths. For higher dimensions, the convex hull is represented by planes/hyper-planes and inequalities. The Quick Hull Algorithm [88] in Matlab can be used to compute the convex hull of a set of points efficiently. For a given convex hull, the Matlab function *inhull* [89] can be used to determine whether an arbitrary point lies in the interior of the hull or not.

Definition 2. *Slice of a Convex Hull: The slice of a convex hull is the set obtained by intersecting*

the convex hull with a hyper-plane.

The slice of a convex hull is also convex. It can be computed using the Matlab function *intersectionhull* [90].

Definition 3. *Cluster: For a given set of points, a cluster is a subset where any two points in the subset is density-reachable for some pre-defined distance metric* ε.

Simply stated, two points are said to be density-reachable if there is a chain of intermediate points and the distance between neighboring points does not exceed ε. A more formal definition of cluster and a cluster identification algorithm can be found in [91]. A cluster of points can be identified using the Matlab function *DBSCAN* [92].

2.4.2 Algorithm

We choose a discrete set of points $S_0 = \{x_1^0, x_2^0, \cdots, x_N^0\}$ on the boundary of the conservative $\mathscr{R}_A^e$ at time t_0, where N is a sufficiently large number. The conservative $\mathscr{R}_A^e$, denoted by Ω_0, can be Ω_{lin} or Ω_{sos}, for example. Now consider the time sequence t_i, $i = 0, 1, 2, \cdots$, where $t_k = t_0 + k\Delta t$, and Δt is some pre-defined time interval. Define the set $S_i = \{x_1^i, x_2^i, \cdots, x_N^i\}$, $i = 0, 1, 2, \cdots$, which is obtained by reversing the trajectories of the points in S_0 for $i\Delta t$ interval of time. Conv(S_i) is an enlarged $\mathscr{R}_A^e$ if:

1. none of the points in S_{i+k}, where k is some pre-defined positive integer, lies in the interior of Conv(S_i), and

2. the vertices of Conv(S_i) form a single cluster around the origin with distance metric ε [42].

For $i, j = 0, 1, 2, \cdots$, let m_i^{i+j} denote the number of points which remain in the interior of Conv(S_i) at a time t_{i+j} and $\mathscr{N}_C$(Conv(S_i)) represent the number of clusters formed by the vertices of Conv(S_i). The complete algorithm for obtaining a large estimate of $\mathscr{R}_A^e$, which we refer to as CHART (Convex Hull Algorithm Using Reversal of Trajectories), is presented next.

Algorithm CHART
(Convex Hull Algorithm Using Reversal of Trajectories)

Initialization: Choose a sufficiently large integer N which represents the number of points located uniformly on the boundary of Ω_0 and a sufficiently small distance metric ε.

Step 1: Select a suitable time interval Δt and sufficiently large positive integers k_1 and k_2, $k_1 < k_2$.

Step 2:

Let $\ell = 0$
For $i = 1$ to k_1
  If $\ell = i - 1$
    For $j = 1$ to k_2
      If $m_i^{i+j} = 0$ and $\mathscr{N}_C(\text{Conv}(S_i)) = 1$
        $\ell = i$
        Break (exit from the inner **For** loop which
              checks the condition on j)
      End If
    End For
  End If
End For

Step 3: If $\ell = 0$, repeat **Steps 1 to 2** with a lower value of Δt than chosen in **Step 1**

Result: $\text{Conv}(S_\ell)$ is the enlarged $\mathscr{R}_A^e$.

Parameter Selection: The choice of k_1 and k_2 is a trade-off between the enlargement of the $\mathscr{R}_A^e$ and the computation time. A few examples showing the choice of N, ε, Δt, k_1, k_2 are provided in [42].

For the ease of understanding, the CHART is explained for a system with two state variables with the help of Fig.2.6. At time $t = t_0$, the boundary of the conservative estimate Ω_0 is discretized into the set of points $S_0 = \{x_1^0, x_2^0, \cdots, x_N^0\}$, where N is a large number - see Fig.2.6 (a). At time $t = t_1$, it is found that some points in S_1 lie in the interior of $\text{Conv}(S_1)$, *i.e.* $m_1^1 \neq 0$ - see Fig.2.6 (b). However, after k intervals of time Δt, it is found that none of the points in S_{1+k} lie in the interior of $\text{Conv}(S_1)$, *i.e.* $m_1^{1+k} = 0$. Additionally, the vertices of $\text{Conv}(S_1)$ form a single cluster, *i.e.* $\mathscr{N}_C(\text{Conv}(S_1)) = 1$. Therefore, $\mathscr{R}_A^e = Conv(S_1)$ - see Fig.2.6 (c). The single cluster requirement ensures that the vertices of the convex hull are sufficiently close to one another and hence the boundary of the convex hull is a positively invariant set.

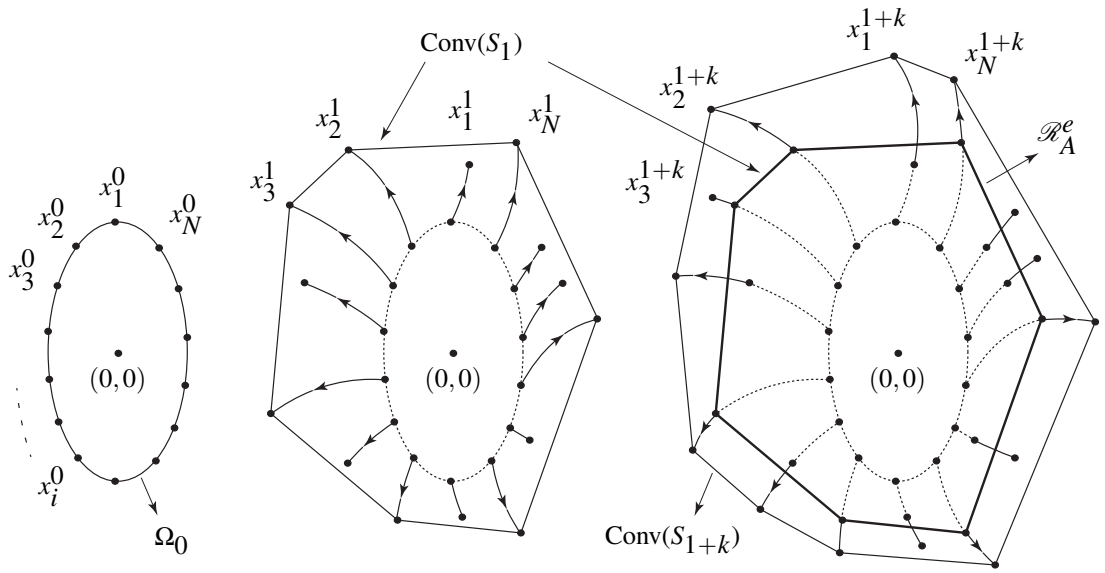

$t = t_0$ $\quad$ $t = t_1 = (t_0 + \Delta t)$ $\quad$ $t = t_{1+k} = (t_1 + k\Delta t)$

$S_0 = \{x_1^0, \cdots, x_N^0\}$ $\quad$ $S_1 = \{x_1^1, \cdots, x_N^1\}$ $\quad$ $S_{1+k} = \{x_1^{1+k}, \cdots, x_N^{1+k}\}$

(a) (b) (c)

Figure 2.6: (a) Discretization of the boundary of conservative $\mathscr{R}_A^e = \Omega_0$ at $t = t_0$ yields S_0, (b) Convex hull Conv(S_1) constructed at time $t = t_1$, (c) Enlarged $\mathscr{R}_A^e$ obtained as Conv(S_1) at time $t = t_{1+k}$.

2.5 Enlarging the Region of Attraction Using SOS, CHART and IMM

In the last section, we presented CHART for obtaining a larger $\mathscr{R}_A^e$ starting from a conservative $\mathscr{R}_A^e$. To improve the effectiveness of the IMM, we now apply CHART to obtain an $\mathscr{R}_A^e$ for the Tiptoebot starting from the conservative estimate Ω_{sos}. It should be noted that the SOS method optimizes the stabilizing controller to obtain the largest $\mathscr{R}_A^e$ and the CHART improves upon this estimate further without changing the controller.

The CHART was implemented for the Tiptoebot equilibrium configuration $(\theta_1, \theta_2, \theta_3, \dot{\theta}_1, \dot{\theta}_2, \dot{\theta}_3) =$

$(\pi/2, 0, 0, 0, 0, 0)$ using the following parameter values, which were selected by trial and error:

$$N \approx 3 \times 10^6, \quad \varepsilon = 0.01, \quad \Delta t = 0.0026, \quad k_1 = 10, \quad k_2 = 65$$

The enlarged estimate $\mathscr{R}_A^e$, which is a convex hull in a six-dimensional space, was obtained as $\Omega_{chart} = Conv(S_4)$.

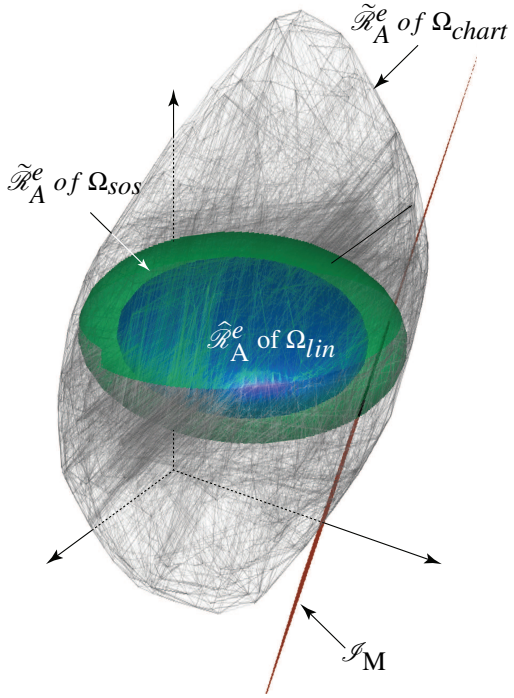

Figure 2.7: Slices of Ω_{chart}, Ω_{sos} and Ω_{lin}, and their intersection with the impulse manifold, $\mathscr{I}_M$. For better visualization and for ease of comparison, the same coordinate system of Fig.2.3 is used.

We now reconsider the simulation in section 2.3.2. For the initial configuration of the Tiptoebot given by (2.3.1), the slice $\widetilde{\mathscr{R}}^e_A(q^* = 0)$ of Ω_{chart} is shown in Fig.2.7 together with the slices of Ω_{lin} and Ω_{sos} that were previously shown in Fig.2.3. It can be seen that $\widetilde{\mathscr{R}}^e_A$ of Ω_{chart} is significantly larger than that of Ω_{sos}. The impulse manifold $\mathscr{I}_M(0,0,0.21)$ described by (2.3.2), shown previously in Fig.2.3, can be seen to intersect $\widetilde{\mathscr{R}}^e_A$ of both Ω_{chart} and Ω_{sos} in Fig.2.7.

The $\widehat{\mathscr{R}}^e_A$ of Ω_{chart} is a convex region on the impulse manifold and is shown in Fig.2.8 in the original coordinates. The $\widehat{\mathscr{R}}^e_A$ of Ω_{sos}, shown previously in Fig.2.4 and now shown in Fig.2.8, lies in the interior of $\widehat{\mathscr{R}}^e_A$ of Ω_{chart}. To take the configuration of the Tiptoebot from outside $\mathscr{R}^e_A$ to inside $\mathscr{R}^e_A$, we now choose the following velocity configuration that lies in the interior of $\widehat{\mathscr{R}}^e_A$ of Ω_{chart}:

$$\begin{bmatrix} \dot{q}_1 & \dot{q}_2^T \end{bmatrix} = \begin{bmatrix} 1.57 & -2.69 & 0.18 \end{bmatrix} \tag{2.5.1}$$

The desired effect of the impulsive inputs is shown by the dotted line joining the initial and desired velocity configurations, both of which lie on $\mathscr{I}_M$ - see Fig.2.8. To implement the IMM, the high-gain feedback in (2.2.7) was used with $\dot{q}_2^{des} = \dot{q}_2$ in (2.5.1), $\mu = 0.0004$, $\lambda_1 = 10$ and $\lambda_2 = 1$; the

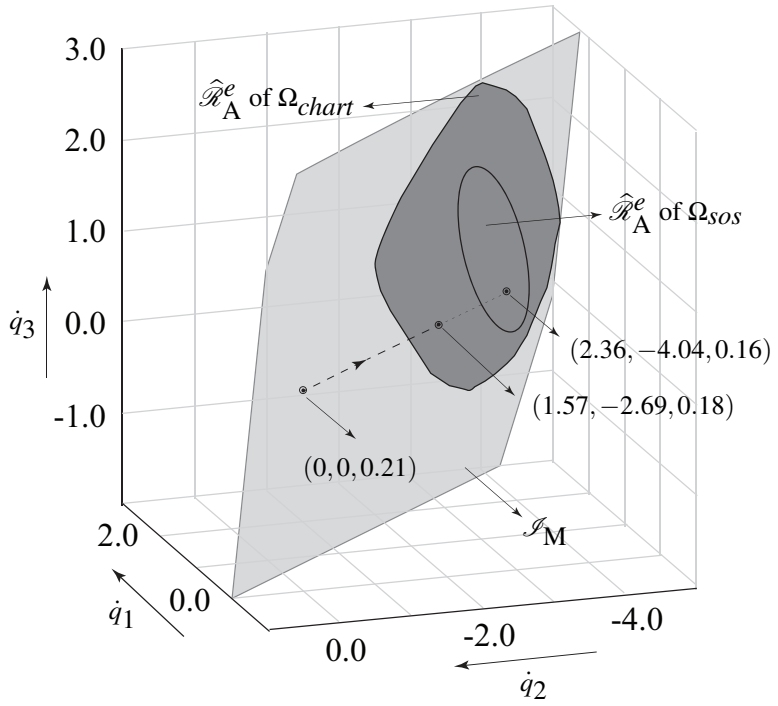

Figure 2.8: Intersection of the slices of Ω_{chart} and Ω_{sos} with the impulse manifold $\mathscr{I}_{\mathrm{M}}$ in the original coordinates; the intersection set $\widehat{\mathscr{R}}^e_{\mathrm{A}}$ of Ω_{chart} is a convex region and encloses the $\widehat{\mathscr{R}}^e_{\mathrm{A}}$ of Ω_{sos}.

results are shown in Fig.2.9. The high-gain controller is active over $t \in [0, 0.004]$; its effect is shown using a dilated time scale. The high-gain controller is switched off and the stabilizing controller is switched on at $t = 0.004$ when the system configuration is inside $\mathscr{R}^e_{\mathrm{A}}$. The stabilization of the equilibrium after $t > 0.004$ is shown using a normal time scale.

The desired velocity configuration in (2.5.1) was chosen to lie on the line joining the initial velocity configuration $(0.0, 0.0, 0.21)$ and the desired velocity configuration chosen for the SOS-IMM method in section 2.3, given by (2.3.3). It can be seen from Fig.2.8 that the initial velocity configuration is closer to the desired velocity configuration in (2.5.1) than the desired velocity configuration in (2.3.3). Consequently, the magnitudes of the high-gain feedback for the SOS-CHART-IMM method are less than that of the SOS-IMM method - see plots of τ_2 and τ_3 in Figs.2.5 and 2.9 for $t \in [0.00, 0.004]$.

We complete this section with a second example that further illustrates the benefit of using SOS-CHART-IMM for enlarging the $\mathscr{R}^e_A$ over SOS-IMM. In this example, the initial configuration

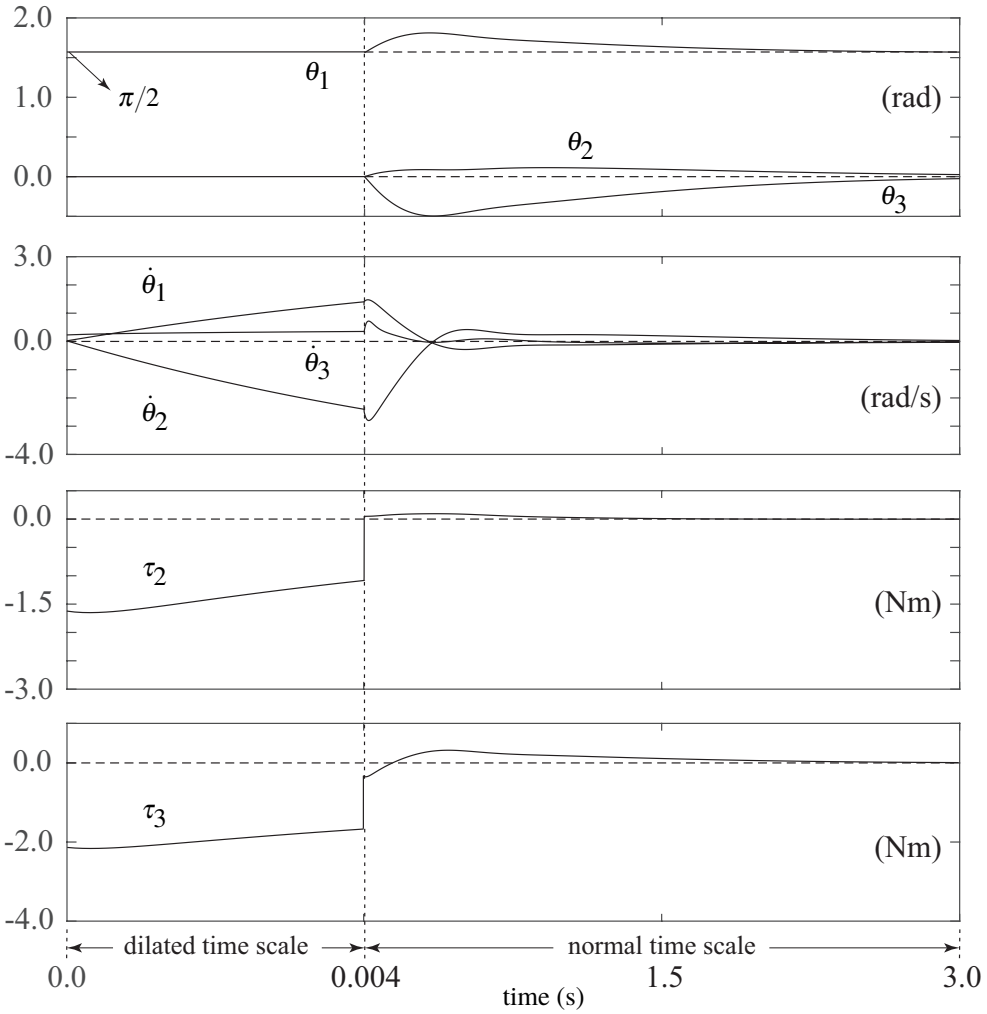

Figure 2.9: Effective enlargement of $\mathscr{R}_A^e$ using SOS-CHART-IMM: Plot of joint angles, their velocities, and control inputs with time for stabilization of the Tiptoebot from the initial configuration given by (2.3.1).

of the Tiptoebot is chosen to be

$$x = \begin{bmatrix} q^* & \dot{q}^* \end{bmatrix}^T = \begin{bmatrix} -0.2 & 0.3 & 0.3 & 0.0 & 0.0 & 0.0 \end{bmatrix}^T \tag{2.5.2}$$

This initial configuration, shown in Fig.2.10 (a), lies outside Ω_{chart}, and hence outside Ω_{sos}. The $\widetilde{\mathscr{R}}_{\mathrm{A}}^e(q^*)$ of Ω_{sos} is found to be a null set and consequently $\widehat{\mathscr{R}}_{\mathrm{A}}^e(q^*)$ of Ω_{sos} is also a null set. Therefore, the IMM cannot be used to enlarge Ω_{sos}. However, it can be seen from Fig.2.10 (b) that $\widetilde{\mathscr{R}}_{\mathrm{A}}^e(q^*)$ of Ω_{chart} is not a null set and the $\mathscr{I}_{\mathrm{M}}$ intersects it. The $\widehat{\mathscr{R}}_{\mathrm{A}}^e$ of Ω_{chart} is a convex region on $\mathscr{I}_{\mathrm{M}}$ and is shown in Fig.2.10 (c). To take the configuration of the Tiptoebot from outside $\mathscr{R}_{\mathrm{A}}^e = \Omega_{chart}$ to inside Ω_{chart}, we choose the following velocity configuration that lies in the interior

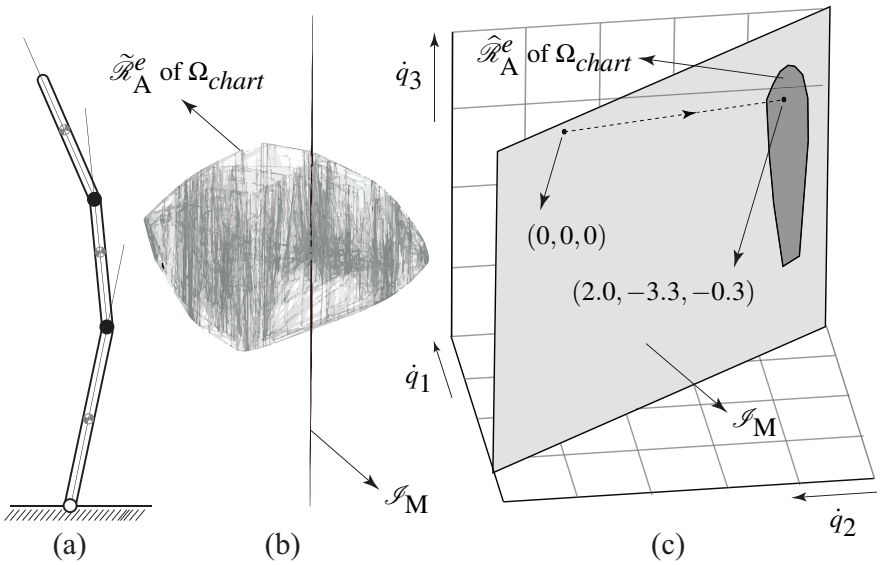

Figure 2.10: (a) Initial configuration of the Tiptoebot, given by (2.5.2), lies outside Ω_{chart}, (b) $\widetilde{\mathscr{R}}^e_{\mathrm{A}}$ of Ω_{chart} (shown in transformed coorrdinates for better visualization) is a convex hull whereas $\widetilde{\mathscr{R}}^e_{\mathrm{A}}$ of Ω_{sos} is a null set, (c) intersection of the slice of Ω_{chart} with the impulse manifold $\mathscr{I}_{\mathrm{M}}$, shown in the original coordinates.

of $\widehat{\mathscr{R}}^e_{\mathrm{A}}$ of Ω_{chart}:

$$\begin{bmatrix} \dot{q}_1 & \dot{q}_2^T \end{bmatrix} = \begin{bmatrix} 2.0 & -3.3 & -0.3 \end{bmatrix} \tag{2.5.3}$$

The desired effect of the impulsive inputs is shown by the dotted line joining the initial and desired velocity configurations on the $\mathscr{I}_{\mathrm{M}}$ - see Fig.2.10 (c). To avoid repetition, the simulation results of high-gain feedback followed by stabilization are not presented.

2.6 Experimental Verification of Enlargement of $\mathscr{R}^e_{\mathrm{A}}$ using SOS, CHART and IMM

2.6.1 Hardware Description

Experiments were done with a two-link Pendubot system. A schematic of the pendubot is shown in Fig.2.11. The equations of motion of the pendubot are in the form of (2.2.2) where $n = 2$, $m = 1$ and

$$q = \begin{bmatrix} q_1 \\ q_2 \end{bmatrix} = \begin{bmatrix} \theta_2 - \pi \\ \theta_1 \end{bmatrix}, \qquad u = \tau \tag{2.6.1}$$

The equations of motion in terms of the variables q_1 and q_2 can be found in [23]; the lumped parameters of the pendubot that appear therein are given in Table 2.2.

The torque τ in the shoulder joint (joint with angle $q_2 = \theta_1$) of the pendubot is applied by a 90-volt direct-drive permanent magnet brushed DC motor[3] The motor is driven by a power amplifier[4] with a maximum current limit of 25 A, operating in current mode. The motor torque constant is 0.4 Nm/A and the amplifier gain is 11.5 A/volt. The torque constant and the current limit together imply that the maximum torque that can be applied by the motor is 10 Nm. The pendubot was interfaced with a dSpace DS1104 board and the controller was implemented in the Matlab/Simulink environment for real-time control.

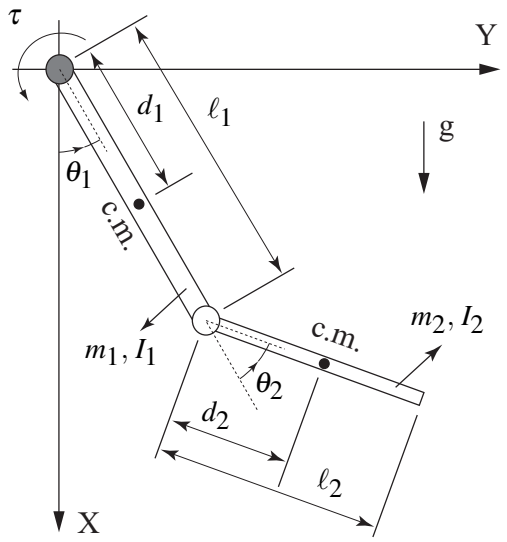

Figure 2.11: An arbitrary configuration of the two-link pendubot.

Table 2.2: Lumped Parameters for Pendubot in SI units

β_1	β_2	β_3	β_4	β_5
0.0147	0.0051	0.0046	0.1001	0.0302

[3]The motor manufacturer is Minnesota Electric Technology.

[4]The amplifier is a product of Advanced Motion Control.

2.6.2 Design of Experiment

The equilibrium configuration chosen for stabilization was $x = (q^T, \dot{q}^T)^T = 0 \Rightarrow (\theta_1, \theta_2, \dot{\theta}_1, \dot{\theta}_2) = (0, \pi, 0, 0)$. The SOS method was used to design a stabilizing second-order polynomial controller $u_s(x)$; the controller is given below

$$\begin{aligned}\tau = &-14.926\theta_1 - 1.951{\theta_1}^2 - 17.728(\theta_2 - \pi) - 2.514(\theta_2 - \pi)^2 - 4.469\theta_1(\theta_2 - \pi) - 1.224\dot{\theta}_1 \\ &+ 0.003{\dot{\theta}_1}^2 - 0.105\theta_1\dot{\theta}_1 - 0.121(\theta_2 - \pi)\dot{\theta}_1 - 2.813\dot{\theta}_2 - 0.055{\dot{\theta}_2}^2 - 0.671\theta_1\dot{\theta}_2 \\ &- 0.766(\theta_2 - \pi)\dot{\theta}_2 - 0.018\dot{\theta}_1\dot{\theta}_2 \end{aligned} \tag{2.6.2}$$

The corresponding estimated region of attraction, Ω_{sos} in (2.2.10), was obtained as $V(x) \leqslant \rho = 0.083$ where

$$\begin{aligned}V(q, \dot{q}) = &\, 1.24{q_2}^2 + 3.01\, q_1 q_2 + 0.15\, q_2\dot{q}_2 + 0.43\, q_2\dot{q}_1 + 2.03{q_1}^2 + 0.18\, q_1\dot{q}_2 + 0.54\, q_1\dot{q}_1 \\ &+ 0.005{\dot{q}_2}^2 + 0.026\,\dot{q}_1\dot{q}_2 + 0.040{\dot{q}_1}^2 \end{aligned} \tag{2.6.3}$$

Subsequently, the enlarged estimated region of attraction was obtained as $\Omega_{chart} = Conv(S_8)$ using the following parameter values:

$$N = 729000, \quad \varepsilon = 0.01, \quad \Delta t = 0.0035, \quad k_1 = 10, \quad k_2 = 18$$

To demonstrate the enlargement of the $\mathscr{R}_A^e = \Omega_{chart}$ using the IMM, we consider the following initial configuration that lies outside Ω_{chart}:

$$x = \begin{bmatrix} q^{*T} & \dot{q}^{*T} \end{bmatrix}^T = \begin{bmatrix} 0.00 & -0.72 & 0.25 & 0.00 \end{bmatrix}^T \tag{2.6.4}$$

For the initial configuration of the pendubot given by (2.6.4), the slice $\widetilde{\mathscr{R}}_{\mathrm{A}}^e(q_1^* = 0.00, q_2^* = -0.72)$ of Ω_{chart} is shown in Fig.2.12 together with the slice of Ω_{sos}. It can be seen that $\widetilde{\mathscr{R}}_{\mathrm{A}}^e$ of Ω_{chart} is significantly larger than that of Ω_{sos}. The impulse manifold $\mathscr{I}_{\mathrm{M}}(0.25, 0.00)$, which is line, is given by the relation

$$\dot{q}_1 + (1 - \beta_3/\beta_2)\,\dot{q}_2 - 0.25 = 0 \tag{2.6.5}$$

and is found to intersect $\widetilde{\mathscr{R}}_{\mathrm{A}}^e$ of Ω_{chart} but not that of Ω_{sos}. Therefore, $\widehat{\mathscr{R}}_{\mathrm{A}}^e$ of Ω_{chart} is a line segment of the impulse manifold (shown in Fig.2.12 using a thicker line) whereas $\widehat{\mathscr{R}}_{\mathrm{A}}^e$ of Ω_{sos} is a

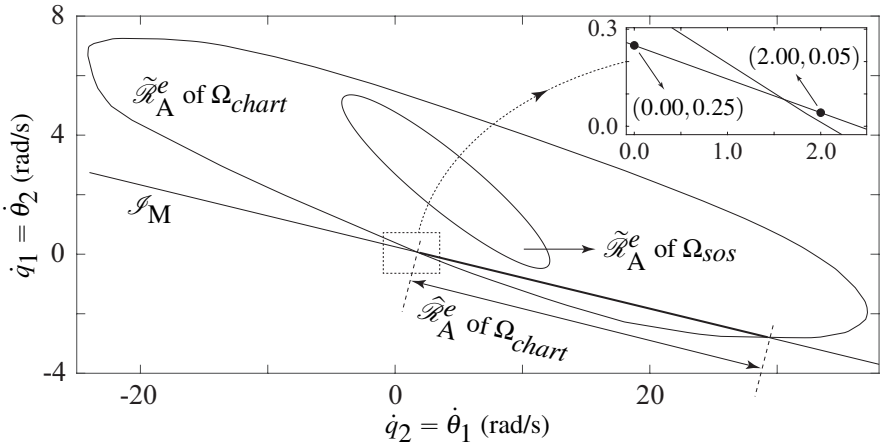

Figure 2.12: Intersection of $\widetilde{\mathscr{R}}^e_{\rm A}$ of Ω_{chart} with $\mathscr{I}_{\rm M}$; the intersection set $\widehat{\mathscr{R}}^e_{\rm A}$ of Ω_{chart} is the dark line segment. The impulse manifold $\mathscr{I}_{\rm M}$ was determined by the initial velocity configuration $(\dot{q}_2, \dot{q}_1) = (0.00, 0.25)$. The desired velocity configuration $(\dot{q}_2, \dot{q}_1) = (2.00, 0.05)$ was chosen to lie on $\widehat{\mathscr{R}}^e_{\rm A}$ of Ω_{chart}. A zoomed-out scale has been used to show the entire $\widetilde{\mathscr{R}}^e_{\rm A}$ of Ω_{chart}; due to this scaling the initial and desired velocity configurations appear to be close.

null set. To take the configuration of the pendubot from outside $\mathscr{R}^e_{\rm A}$ to inside $\mathscr{R}^e_{\rm A}$, we now choose the following velocity configuration that lies in the interior of $\widehat{\mathscr{R}}^e_{\rm A}$ of Ω_{chart}:

$$\begin{bmatrix} \dot{q}_1 & \dot{q}_2 \end{bmatrix} = \begin{bmatrix} \dot{\theta}_2 & \dot{\theta}_1 \end{bmatrix} = \begin{bmatrix} 0.05 & 2.00 \end{bmatrix} \tag{2.6.6}$$

Our experimental verification involved the following steps:

1. *Feedback Linearization:* A controller was designed using feedback linearization [73] to fix the configuration of the first link at $(q_2, \dot{q}_2) = (\theta_1, \dot{\theta}_1) = (-0.72, 0.00)$. With the first link fixed, the second link behaves as a simple pendulum. To achieve the configuration $(q_1, \dot{q}_1) = (\theta_2 - \pi, \dot{\theta}_2) = (0.00, 0.25)$, the second link was manually taken to an angle (at time t_0) and released from rest; this angle was determined through trial and error. At time t_1^-, the configuration in (2.6.4) is achieved - see Fig.2.13 (a), and the feedback linearizing controller was switched off.

2. *High-Gain Control:* To implement the IMM, the high-gain controller in (2.2.7) was switched on at time t_1^-. For the high-gain controller, we used $\dot{q}_2^{des} = \dot{q}_2$ in (2.6.6), $\mu = 0.001$, and $\lambda_1 = 1$. The high-gain controller was switched off at time t_1^+ when the joint velocities reached a small neighborhood of (2.6.6) - see Fig.2.13 (b).

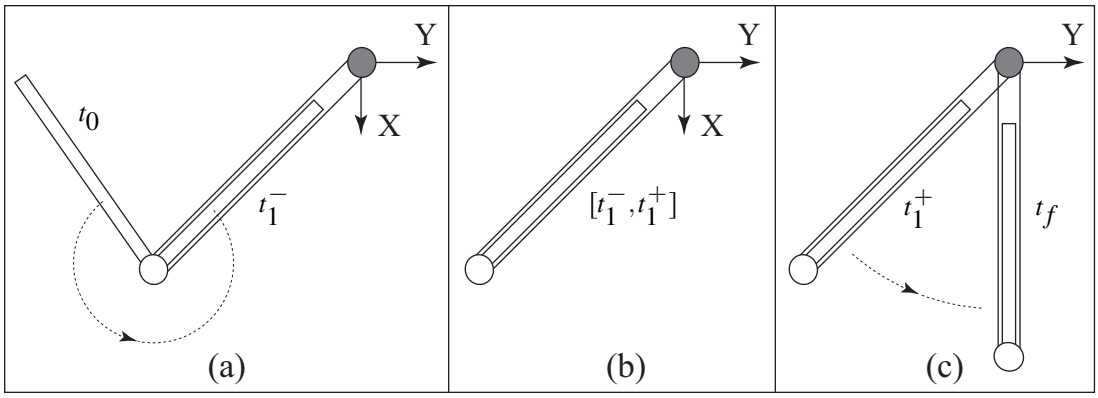

Figure 2.13: Steps of experimental verification using the pendubot shown in Fig.2.11: (a) $[t_0, t_1^-)$ - feedback linearizing control, (b) $[t_1^-, t_1^+]$ - high-gain feedback, (c) $(t_1^+, t_f]$ - SOS stabilizing control

3. *Stabilizing Control:* The SOS controller in (2.6.2) was invoked at time t_1^+. The pendubot configuration reaches the desired equilibrium at time t_f - see Fig.2.13 (c).

2.6.3 Experimental Results

The experimental results are shown in Fig.2.14. Simulation results are presented in Fig.2.15 to compare the experimental results with the ideal behavior. The total time scale is divided into three intervals corresponding to the three steps discussed in the last section. In the experiment, the purpose of first step was to create the initial configuration of the pendubot in (2.6.4). In the simulation, the first step was not necessary as the pendubot was simply assumed to have this configuration. In the experiment, at time t_0, the second link was released from $\theta_2 = -2.28$ rad ≈ -131 deg with the feedback linearizing controller active. At time t_1^-, the feedback linearizing controller was switched off and the high-gain controller switched on since the configuration of the pendubot was close to the desired initial configuration in (2.6.4); the pendubot configuration was $(\theta_1, \theta_2, \dot{\theta}_1, \dot{\theta}_2) = (-0.72, \pi, 0.00, 0.42)$ - see Fig.2.14.

For both the experiment and the simulation, the high gain controller was switched on at time t_1^-. For better visualization, the effect of high-gain control is illustrated using a dilated time scale. Due to the initial error in the actual and desired velocities of the actuated joint, the high-gain controller invokes a large torque at time t_1^-. Through our simulation, this torque was found to be

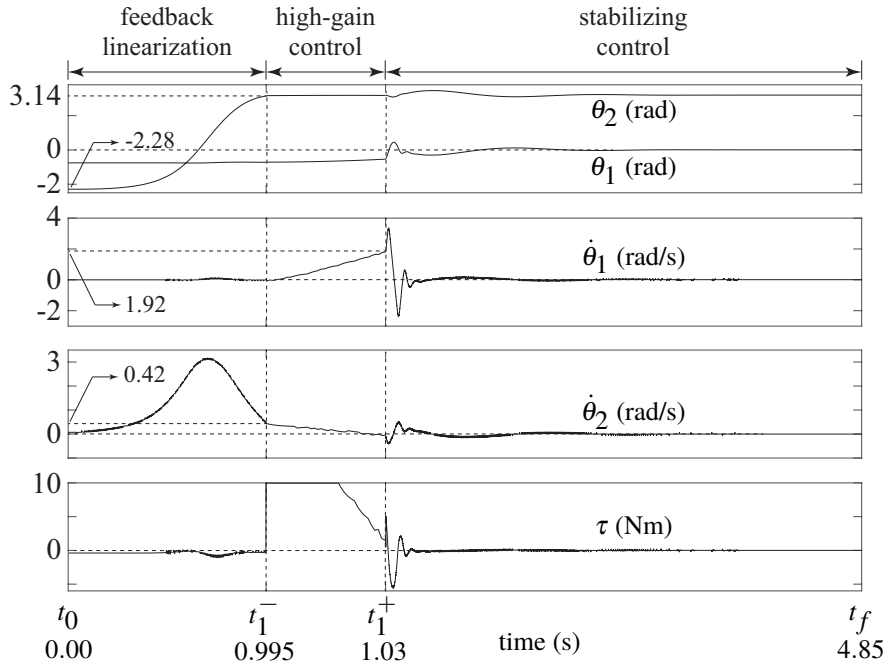

Figure 2.14: Experimental verification of enlargement of $\mathscr{R}_A^e$ of pendubot: Plot of joint angles, their velocities, and control input with time. The effect of high-gain feedback is shown using a dilated time scale; the effect of the stabilizing controller is shown using a normal time scale.

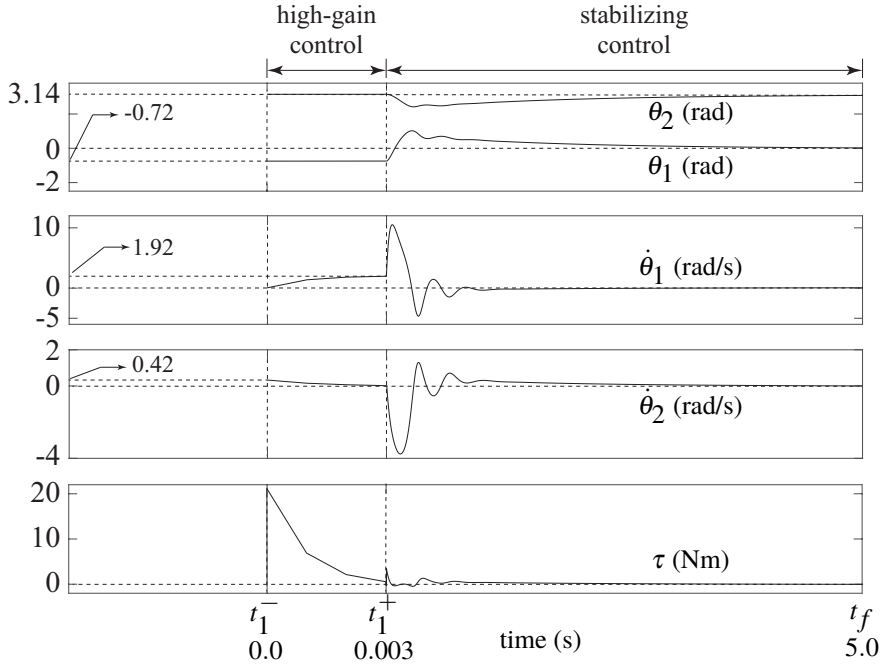

Figure 2.15: Simulation results of ideal pendubot behavior for comparison with experimental results presented in Fig.2.14.

of the order of 20 Nm. In the ideal case, the high-gain controller remains active for a very short interval of time and the control input decays exponentially during this interval [23]. This can be verified from the simulation where the time interval is equal to 0.003 s. In our experiment, due to the current limit (25 A) of the power amplifier (see section 2.6.1), the torque applied by the motor was saturated at 10 Nm. Therefore, the high-gain controller remained active for a longer duration of time 0.035 s and the control torque decays after remaining saturated for a significant fraction of that interval. The high-gain torque was switched off at time t_1^+ when the joint velocities were close to the desired values in (2.6.6); these values are $(\dot{\theta}_1, \dot{\theta}_2) = (1.92, 0.00)$ for our experiment and $(\dot{\theta}_1, \dot{\theta}_2) = (1.96, 0.05)$ for our simulation. The changes in the joint angles for both the simulation and the experiment were negligible, as expected. Although small, the difference in the joint velocities between the experiment and the simulation at time t_1^+ can be attributed to several factors. These include: (a) error between the actual and desired configuration at time t_1^-, (b) saturation of the high-gain torque, and (c) sensitivity of the slope of the impulse manifold (line) $\mathscr{I}_{\mathrm{M}}$ to the system parameters - see (2.6.5).

The SOS stabilizing controller was switched on at time t_1^+ and the pendubot reached its equilibrium configuration shortly thereafter. The time required for stabilization and the transient behavior of the system are similar for both the experiment and the simulation. A video of the experiment can be found on the weblink:

`https://www.egr.msu.edu/~mukherji/RofAEnlargeStableUnstable.mp4`

CHAPTER 3

IMPULSIVE DYNAMICS AND CONTROL OF THE INERTIA-WHEEL PENDULUM

3.1 Introduction

The problem of designing rest-to-rest maneuvers for the inertia-wheel pendulum using a sequence of impulsive inputs is addressed. The use of impulsive inputs simplifies the dynamics of the IWP and permits the design of optimal sequences under some general assumptions[1]. This chapter is organized as follows: the mathematical model of the inertia-wheel pendulum and the formal problem statement is presented in section 3.2. In section 3.3, rest-to-rest maneuver is designed using a sequence of two impulsive inputs and a generalization of this result which utilizes a sequence of N impulsive inputs is presented in section 3.4. In section 3.4, it is also proven that a sequence with an odd number of inputs is less optimal than the two adjacent sequences with even number of inputs. Finally simulation results are presented in section 3.5 which provides insights into high wheel velocity for the inertia-wheel pendulum obtained in prior works.

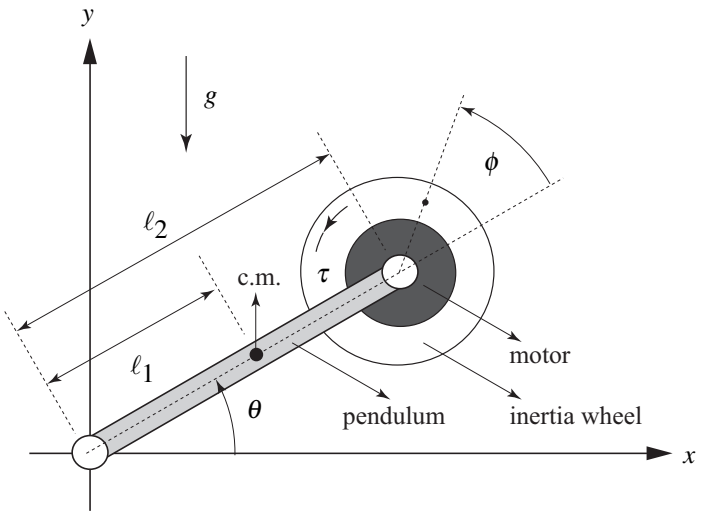

Figure 3.1: The inertia wheel pendulum is shown in an arbitrary configuration.

[1]The frequently used symbols in this chapter are defined earlier - see key to symbols before chapter 1.

3.2 Mathematical Model and Problem Statement

3.2.1 Equations of Motion

The Inertia-Wheel Pendulum (IWP), shown in Fig.3.1, is an underactuated system comprised of a simple pendulum and an inertia wheel. The inertia wheel, also referred to as a reaction wheel, is driven by a motor mounted at the distal end of the pendulum. The kinetic energy T and the potential energy V of the IWP are given by the relations:

$$T = m_{11}\dot{\theta}^2 + m_{22}(\dot{\theta}+\dot{\phi})^2, \qquad V = \beta \sin\theta \tag{3.2.1}$$

$$m_{11} = \left(m_1 l_1^2 + m_2 l_2^2 + I_1\right)/2, \qquad m_{22} = I_2/2$$
$$\beta = (m_1 l_1 + m_2 l_2) g$$

Using (3.2.1), the Euler-Lagrange equation of motion of the IWP can be written as:

$$2\,(m_{11}+m_{22})\ddot{\theta} + 2\,m_{22}\ddot{\phi} + \beta\,\cos\theta = 0 \tag{3.2.2a}$$

$$2\,m_{22}\ddot{\theta} + 2\,m_{22}\ddot{\phi} = \tau \tag{3.2.2b}$$

Note that the angle ϕ does not appear in (3.2.2a) or (3.2.2b) - this is because the wheel is symmetric about its axis of rotation.

3.2.2 Effect of Impulsive Input and Constants of Free Motion

The application of an ideal impulsive torque τ_i by the motor at time t_i results in discontinuous jumps in the velocities of both the pendulum and the wheel while their angular positions remain unchanged. By integrating (3.2.2a) with respect to time over the infinitesimal interval $[t_i^-, t_i^+]$, it can be shown [23] that these jumps satisfy the relation:

$$(\dot{\theta}_i^+ - \dot{\theta}_i^-) = -C(\dot{\phi}_i^+ - \dot{\phi}_i^-), \qquad C \triangleq \frac{m_{22}}{(m_{11}+m_{22})} \tag{3.2.3}$$

Using (3.2.2b), the jump in the pendulum velocity can be shown to be related to the angular impulse as follows:

$$\mathscr{I}_i \triangleq \int_{t_i^-}^{t_i^+} \tau_i \, dt = 2m_{22}\left[(\dot{\theta}_i^+ - \dot{\theta}_i^-) + (\dot{\phi}_i^+ - \dot{\phi}_i^-)\right] \tag{3.2.4a}$$

$$\Rightarrow \quad \mathscr{I}_i = -2m_{11}(\dot{\theta}_i^+ - \dot{\theta}_i^-) \tag{3.2.4b}$$

where (3.2.4b) was obtained from (3.2.4a) using (3.2.3).

If $\tau = 0$, the dynamics of the IWP described by (3.2.2a) or (3.2.2b) simplifies to the form

$$2m_{11}\ddot{\theta} + \beta \cos\theta = 0 \tag{3.2.5a}$$

$$\ddot{\theta} + \ddot{\phi} = 0 \tag{3.2.5b}$$

The above equations are the differential forms for conservation of energy of the IWP and conservation of angular momentum of the wheel, namely

$$m_{11}\dot{\theta}^2 + \beta \sin\theta = constant \tag{3.2.6a}$$

$$\dot{\theta} + \dot{\phi} = constant \tag{3.2.6b}$$

It can be seen from (3.2.6a) and (3.2.6b) that the dynamics of the pendulum and wheel are decoupled and simplified when $\tau = 0$. For controlling the IWP, this motivates the use of impulsive torques at discrete instants of time.

3.2.3 Problem Statement: Rest-to-Rest Maneuvers

We consider the problem of designing a set of discrete impulsive inputs over the time interval $[t_0, t_f]$ for rest-to-rest maneuvers of the IWP between two configurations where the final configuration has higher potential energy than the initial configuration, *i.e.*

$$\dot{\theta}_0 = \dot{\phi}_0 = 0 \tag{3.2.7a}$$

$$\dot{\theta}_f = \dot{\phi}_f = 0 \tag{3.2.7b}$$

$$\beta\,(\sin\theta_f - \sin\theta_0) > 0 \tag{3.2.7c}$$

and θ lies in the range $(-3\pi/2, \pi/2]$. For a given value of N, the task is to design the vector $\mathscr{I}^N = [\mathscr{I}_1\ \mathscr{I}_2\ \cdots\ \mathscr{I}_N]$ where

$$sign(\mathscr{I}_k) = -sign(\mathscr{I}_{k-1}), \quad k = 2, 3, \cdots, N \tag{3.2.8}$$

and $t_0 < t_1 < t_2 < \cdots < t_N < t_f$. The rationale for imposing the constraint in (3.2.8) will be provided later, at the beginning of section 3.4. For the sake of simplicity, it is assumed that the time instants t_i are such that the angular velocity of the pendulum is momentarily zero, *i.e.*,

$$\dot{\theta}_i^- \triangleq \dot{\theta}(t_i^-) = 0, \quad i = 1, 2, \cdots, N \tag{3.2.9}$$

Without loss of generality, it is assumed that the first impulsive torque is applied at time t_1, where $t_1^- = t_0$. Therefore,

$$\dot{\theta}_1^- = \dot{\theta}_0 = 0, \qquad \dot{\phi}_1^- = \dot{\phi}_0 = 0 \tag{3.2.10}$$

Since the angular positions of the pendulum and the wheel do not change during application of an impulsive torque, we have

$$\theta_1 = \theta_0, \qquad \phi_1 = \phi_0 \tag{3.2.11}$$

3.3 Rest-to-Rest Maneuvers: Case of One and Two Impulsive Inputs

3.3.1 Case of One Impulsive Input ($N = 1$)

Using (3.2.3) and (3.2.10), we can write

$$\dot{\theta}_1^+ = -C\dot{\phi}_1^+ \tag{3.3.1}$$

The main result can now be stated as follows:

Result 1: (One Impulsive Input) The rest-to-rest maneuver described by (3.2.7) cannot be accomplished using $\mathscr{I}^1 = [\mathscr{I}_1]$.

Discussion: Since $\tau = 0$ for $[t_1^+, t_f]$, we get from (3.2.6), and (3.2.11):

$$m_{11}\dot{\theta_1^+}^2 + \beta \sin\theta_0 = m_{11}\dot{\theta_f}^2 + \beta \sin\theta_f \tag{3.3.2a}$$

$$\dot{\theta}_1^+ + \dot{\phi}_1^+ = \dot{\theta}_f + \dot{\phi}_f \tag{3.3.2b}$$

Using (3.2.7b), (3.3.2b), and (3.3.1), it can be shown that $\dot{\theta}_1^+ = 0$. From (3.3.2a) we now get $\beta(\sin\theta_f - \sin\theta_0) = 0$, which violates (3.2.7c). This establishes Result 1 by contradiction.

A single impulsive torque can always be chosen to impart sufficient angular momentum to the pendulum such that it reaches its desired configuration with zero angular velocity. However, this impulsive torque will also cause the wheel to have a nonzero angular velocity in the inertial reference frame. This implies that $\dot{\phi} \neq 0$ when $\dot{\theta} = 0$.

3.3.2 Case of Two Impulsive Inputs ($N = 2$)

It is assumed that the first impulse is applied at time t_1 and therefore (3.3.1) is still valid. Two results are presented next. In the first result (Result 2), we relax the assumption in (3.2.9) and design a more general sequence of impulses that satisfies (3.2.7). We will show that the second result (Result 3), which is a special case of the first, automatically satisfies the assumption in (3.2.9).

Result 2: (Two Impulsive Inputs) The rest-to-rest maneuver described by (3.2.7) can be accomplished using $\mathscr{I}^2 = [\mathscr{I}_1 \ \mathscr{I}_2]$, where $\mathscr{I}_2 = -\mathscr{I}_1$.

Discussion: From (3.2.4a) and (3.2.7a) we have

$$\mathscr{I}_1 = 2m_{22}(\dot{\theta}_1^+ + \dot{\phi}_1^+)$$

and since (3.2.6b) holds good for $[t_1^+, t_2^-]$, we can write

$$\mathscr{I}_1 = 2m_{22}(\dot{\theta}_1^+ + \dot{\phi}_1^+) = 2m_{22}(\dot{\theta}_2^- + \dot{\phi}_2^-) \tag{3.3.3}$$

From (3.2.7b) we have $(\dot{\theta}_f + \dot{\phi}_f) = 0$ and since (3.2.6b) holds good for $[t_2^+, t_f]$, we can write $(\dot{\theta}_2^+ + \dot{\phi}_2^+) = 0$. Using (3.2.4a), we can now write

$$\mathscr{I}_2 = -2m_{22}(\dot{\theta}_2^- + \dot{\phi}_2^-) \tag{3.3.4}$$

It is clear from (3.3.3) and (3.3.4) that the conditions in (3.2.7b) require $\mathscr{I}_2 = -\mathscr{I}_1$.

For $[t_1^+, t_2^-]$ and $[t_2^+, t_f]$, the conservation laws in (3.2.6), together with (3.2.7b) and (3.2.11), give

$$m_{11}\dot{\theta}_1^{+\,2} + \beta \sin\theta_0 = m_{11}\dot{\theta}_2^{-\,2} + \beta \sin\theta_2 \tag{3.3.5a}$$

$$\dot{\theta}_2^- + \dot{\phi}_2^- = \dot{\theta}_1^+ + \dot{\phi}_1^+ \tag{3.3.5b}$$

$$m_{11}\dot{\theta}_2^{+\,2} + \beta \sin\theta_2 = \beta \sin\theta_f \tag{3.3.5c}$$

$$\dot{\theta}_2^+ + \dot{\phi}_2^+ = \dot{\theta}_f + \dot{\phi}_f = 0 \tag{3.3.5d}$$

For the second impulse, the relationship between the velocity jumps can be obtained from (3.2.3) as:

$$(\dot{\theta}_2^+ - \dot{\theta}_2^-) = -C(\dot{\phi}_2^+ - \dot{\phi}_2^-) \tag{3.3.6}$$

By substituting the relations $\dot{\phi}_2^+ = -\dot{\theta}_2^+$ from (3.3.5d) and $\dot{\phi}_2^- = \dot{\theta}_1^+ + \dot{\phi}_1^+ - \dot{\theta}_2^-$ from (3.3.5b) into the right-hand side of (3.3.6) and simplifying using (3.3.1), we get

$$(\dot{\theta}_2^+ - \dot{\theta}_2^-) = -\dot{\theta}_1^+ \tag{3.3.7}$$

By combining (3.3.5a) and (3.3.5c) and substituting (3.3.7), we get

$$\begin{aligned}\beta\left(\sin\theta_f + \sin\theta_0 - 2\sin\theta_2\right) &= m_{11}\left[\dot{\theta}_2^{+\,2} + \dot{\theta}_2^{-\,2} - \dot{\theta}_1^{+\,2}\right] \\ &= 2m_{11}\dot{\theta}_2^-\dot{\theta}_2^+\end{aligned}$$

Substituting the expressions for $\dot{\theta}_2^+$ and $\dot{\theta}_2^-$ from (3.3.5a) and (3.3.5c) in the above equation and simplifying, we get

$$|\,\dot{\theta}_1^+\,| = \frac{1}{2}\sqrt{\frac{\beta}{m_{11}}}\,\frac{\left(\sin\theta_f - \sin\theta_0\right)}{\sqrt{\sin\theta_f - \sin\theta_2}} \tag{3.3.8}$$

From (3.2.7c) we know that $(\sin\theta_f - \sin\theta_0) > 0$ and it can be seen from (3.3.5c) that $(\sin\theta_f - \sin\theta_2) > 0$; therefore, the above equation is well-defined. For a given pair $\{\theta_0, \theta_f\}$, (3.3.8) provides a functional relationship between the initial angular velocity $\dot{\theta}_1^+$ (resulting from application of the first impulse $\mathscr{I}_1$) and the configuration θ_2 where the second impulse ($\mathscr{I}_2 = -\mathscr{I}_1$) is applied. There

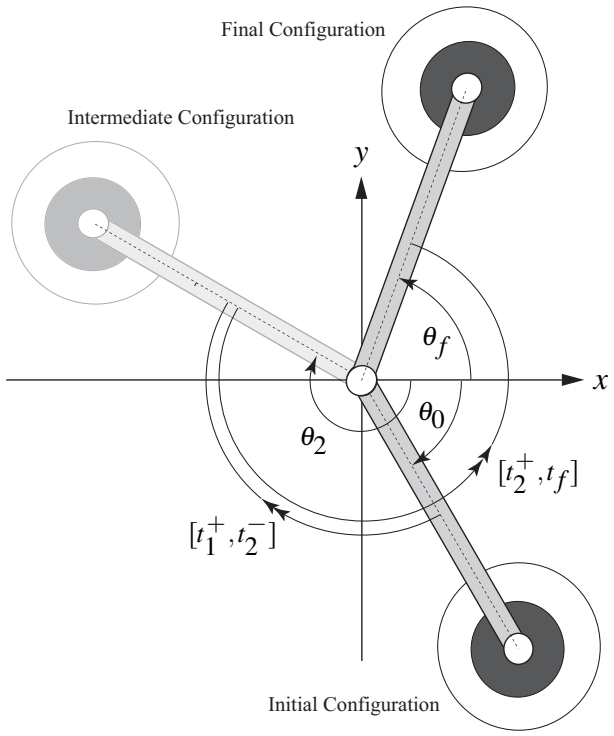

Figure 3.2: An example showing the initial, intermediate, and final configuration of the IWP for the case with two impulsive inputs ($N = 2$).

are infinite solutions given by the pair $\{\dot{\theta}_1^+, \theta_2\}$; for each solution, the value of $\dot{\theta}_1^+$ can be used to compute the impulses $\mathscr{I}_1$ and $\mathscr{I}_2$ ($\mathscr{I}_2 = -\mathscr{I}_1$), using (3.3.1), (3.3.3), and (3.3.4). An example showing the initial, intermediate, and final configuration of the IWP for the case with two impulsive inputs is shown in Fig.3.2. The next result pertains to the particular solution that minimizes the magnitude of the impulses.

Result 3: (Optimal Input $\mathscr{I}^2$) The minimum magnitude of the impulsive inputs required for the rest-to-rest maneuver described by (3.2.7) is

$$|\mathscr{I}_1| = |\mathscr{I}_2| = \sqrt{2m_{11}\beta\left(\sin\theta_f - \sin\theta_0\right)} \tag{3.3.9}$$

Discussion: Using (3.3.1) and (3.3.3), $\mathscr{I}_1$ can be expressed as

$$\mathscr{I}_1 = 2m_{22}(\dot{\theta}_1^+ + \dot{\phi}_1^+) = 2m_{22}(1-C)\dot{\theta}_1^+ \tag{3.3.10}$$

Therefore, the magnitude of $\mathscr{I}_1$ can be minimized by minimizing the magnitude of $\dot{\theta}_1^+$. From

(3.3.5a) it can be seen that

$$m_{11}\dot{\theta_1^+}^2 = m_{11}\dot{\theta_2^-}^2 + \beta\left(\sin\theta_2 - \sin\theta_0\right)$$

If $(\sin\theta_2 - \sin\theta_0) \leqslant 0$, $\dot{\theta}_2^- \neq 0$ but the minimum value of $\dot{\theta}_1^+$ is equal to zero. This implies $(\sin\theta_f - \sin\theta_0) = 0$ from (3.3.8), which contradicts (3.2.7c). Since $(\sin\theta_2 - \sin\theta_0)$ must be positive, the minimum magnitude of $\dot{\theta}_1^+$ can be obtained by choosing $\dot{\theta}_2^- = 0$[2]; this magnitude is equal to

$$|\ \dot{\theta}_1^+\ | = \sqrt{\frac{\beta}{m_{11}}\left(\sin\theta_2 - \sin\theta_0\right)} \tag{3.3.11}$$

By equating (3.3.8) and (3.3.11), we get

$$\sin\theta_2 = \frac{1}{2}(\sin\theta_0 + \sin\theta_f) \tag{3.3.12}$$

where θ_2 is the angle at which the second impulse is applied[3]. Substituting (3.3.12) into (3.3.10) and (3.3.11), and comparing (3.3.3) and (3.3.4) we get

$$|\ \dot{\theta}_1^+\ | = \sqrt{\frac{\beta}{2m_{11}}\left(\sin\theta_f - \sin\theta_0\right)} \tag{3.3.13a}$$

$$\Rightarrow \quad |\ \mathscr{I}_1\ | = |\ \mathscr{I}_2\ | = \sqrt{2m_{11}\beta\left(\sin\theta_f - \sin\theta_0\right)} \tag{3.3.13b}$$

This establishes Result 3.

From Result 3 it can be seen that the time instant t_2 is automatically known when the magnitudes of the individual impulses are minimized. This is different from Result 2, where the choice of t_2 is not unique and each feasible choice of t_2 (alternatively θ_2) uniquely determines the magnitudes of the impulses.

[2]This choice automatically satisfies the assumption in (3.2.9).

[3]It is clear that (3.3.12) can have multiple solutions for θ_2. The procedure for computing the correct solution will be discussed in section 3.4.2. Knowing the value of θ_2, it will be possible to determine the time instant t_2.

3.4 Rest-to-Rest Maneuvers: Generalization to N Inputs

3.4.1 Revisiting the Problem Statement

We start this section with the result that justifies the rationale for imposing the constraint in (3.2.8).
Result 4: (Sum of Two Consecutive Impulses) Consider two impulses $\mathscr{I}_k$ and $\mathscr{I}_{k+1}$ applied at times t_k and t_{k+1}. The net effect of these two impulses in terms of change in the velocities of the pendulum and wheel over the interval $[t_k^-, t_{k+1}^+]$ can be achieved by a single impulse $\bar{\mathscr{I}}$ at time t_k over the interval $[t_k^-, t_k^+]$ where

$$\bar{\mathscr{I}} = \mathscr{I}_k + \mathscr{I}_{k+1} \tag{3.4.1}$$

Discussion: From (3.2.4a) we have

$$\begin{aligned}
\mathscr{I}_k &= 2m_{22}\left[(\dot{\theta}_k^+ - \dot{\theta}_k^-) + (\dot{\phi}_k^+ - \dot{\phi}_k^-)\right] \\
\mathscr{I}_{k+1} &= 2m_{22}\left[(\dot{\theta}_{k+1}^+ - \dot{\theta}_{k+1}^-) + (\dot{\phi}_{k+1}^+ - \dot{\phi}_{k+1}^-)\right]
\end{aligned}$$

Since $\tau = 0$ for $[t_k^+, t_{k+1}^-]$, (3.2.6b) can be used to rewrite the above equations as follows

$$\begin{aligned}
\mathscr{I}_k &= 2m_{22}\left[(\dot{\theta}_{k+1}^- - \dot{\theta}_k^-) + (\dot{\phi}_{k+1}^- - \dot{\phi}_k^-)\right] \\
\mathscr{I}_{k+1} &= 2m_{22}\left[(\dot{\theta}_{k+1}^+ - \dot{\theta}_{k+1}^-) + (\dot{\phi}_{k+1}^+ - \dot{\phi}_{k+1}^-)\right] \\
\Rightarrow \quad \mathscr{I}_k + \mathscr{I}_{k+1} &= 2m_{22}\left[(\dot{\theta}_{k+1}^+ - \dot{\theta}_k^-) + (\dot{\phi}_{k+1}^+ - \dot{\phi}_k^-)\right]
\end{aligned}$$

The change in the velocities of the pendulum and wheel over the interval $[t_k^-, t_{k+1}^+]$ are $(\dot{\theta}_{k+1}^+ - \dot{\theta}_k^-)$ and $(\dot{\phi}_{k+1}^+ - \dot{\phi}_k^-)$, respectively. To achieve the same change over $[t_k^-, t_k^+]$, $\bar{\mathscr{I}}$ must satisfy

$$\begin{aligned}
\bar{\mathscr{I}} &= 2m_{22}\left[(\dot{\theta}_{k+1}^+ - \dot{\theta}_k^-) + (\dot{\phi}_{k+1}^+ - \dot{\phi}_k^-)\right] \\
\Rightarrow \quad \bar{\mathscr{I}} &= \mathscr{I}_k + \mathscr{I}_{k+1}
\end{aligned}$$

This establishes Result 4.

Result 4 clearly indicates that two consecutive impulses of the same sign can be replaced by a single impulse of the same sign. This justifies the constraint imposed in our problem statement that consecutive impulses must have opposite sign.

An extension of Result 4 is now considered. For a rest-to-rest maneuver using two impulsive inputs ($N = 2$), Result 4 implies that $\bar{\mathscr{I}} = \mathscr{I}_1 + \mathscr{I}_2 = 0$. This is true since (3.2.6b) and (3.2.7b) implies $(\dot{\theta}_{k+1}^{+} + \dot{\phi}_{k+1}^{+}) = (\dot{\theta}_2^{+} + \dot{\phi}_2^{+}) = (\dot{\theta}_f^{+} + \dot{\phi}_f^{+}) = 0$, and (3.2.7a) and (3.2.10) implies $(\dot{\theta}_k^{-} + \dot{\phi}_k^{-}) = (\dot{\theta}_1^{-} + \dot{\phi}_1^{-}) = 0$. This is consistent with Result 2, where it was shown that $\mathscr{I}_2 = -\mathscr{I}_1$. A generalization of this result in stated next.

Result 5: (Zero Sum of Impulses) For a rest-to-rest maneuver involving N impulsive inputs, $N \geqslant 2$, the following equation must hold.

$$\sum_{i=1}^{N} \mathscr{I}_i = 0 \tag{3.4.2}$$

Discussion: A sequence of N impulses, $N \geqslant 2$, can be replaced by two impulses by applying Result 4 iteratively. For a rest-to-rest maneuver, the sum of these two impulses is zero - this follows from our discussion above.

It is clear from the discussion above that both Result 4 and Result 5 are quite general and they do not require the assumption in (3.2.9) to be satisfied.

With the motivation of investigating the minimum values of the magnitudes of the impulsive torques, we investigate rest-to-rest maneuver of the IWP with $\mathscr{I}^3$ and $\mathscr{I}^4$. As in the cases with $\mathscr{I}^1$ and $\mathscr{I}^2$, (3.3.1) holds good.

3.4.2 Rest-to-Rest Maneuvers with Even Number of Impulsive Inputs

Theorem 1. *(Optimality of Even Impulse Sequence)*

For a rest-to-rest maneuver of the IWP that satisfies (3.2.7) and (3.2.9) and uses $2n$ impulsive inputs, $n = 1, 2, \cdots$, ${\mathscr{I}^{2n}}_{\infty}$ is minimized by the following choice of inputs:

$$|\mathscr{I}_i| = \frac{1}{\sqrt{n}} \sqrt{2 m_{11} \beta \left(\sin\theta_f - \sin\theta_0\right)}, \quad \forall\, i = 1, 2, \cdots, 2n \tag{3.4.3}$$

The angles where the impulsive inputs are applied satisfy the following relation

$$\sin\theta_i = \left[\frac{2n - i + 1}{2n}\right] \sin\theta_0 + \left[\frac{i - 1}{2n}\right] \sin\theta_f \quad i = 1, 2, \cdots, 2n \tag{3.4.4}$$

Proof: We use induction to first prove (3.4.3). Assuming that (3.4.3) is satisfied for $2m$ impulsive inputs, *i.e.*, $n = m$. We express the magnitudes of the impulses for the case with $(2m+2)$ inputs using the relation

$$|\mathscr{I}_i| = \frac{k_i}{\sqrt{m}}\sqrt{2m_{11}\beta\left(\sin\theta_f - \sin\theta_0\right)}, \quad i = 1,2,\cdots,(2m+2) \tag{3.4.5}$$

where k_i, $i = 1,2,\cdots,(2m+2)$, are arbitrary positive numbers. Using (3.2.4b) and (3.2.9) we can show

$$|\dot{\theta}_i^+| = \frac{k_i}{\sqrt{m}}\sqrt{\frac{\beta}{2m_{11}}\left(\sin\theta_f - \sin\theta_0\right)}, \quad i = 1,2,\cdots,(2m+2) \tag{3.4.6}$$

Using (3.2.9), the conservation law in (3.2.6a) for the time intervals $[t_1^+, t_2^-]$, $[t_2^+, t_3^-]$, $\cdots [t_j^+, t_{j+1}^-]$, $\cdots, [t_{2m+2}^+, t_f]$ can be written as:

$$\begin{aligned}
m_{11}\dot{\theta}_1^{+2} + \beta\,\sin\theta_0 &= \beta\,\sin\theta_2 \\
m_{11}\dot{\theta}_2^{+2} + \beta\,\sin\theta_2 &= \beta\,\sin\theta_3 \\
&\vdots \\
m_{11}\dot{\theta}_j^{+2} + \beta\,\sin\theta_j &= \beta\,\sin\theta_{j+1} \\
&\vdots \\
m_{11}\dot{\theta}_{2m+2}^{+2} + \beta\,\sin\theta_{2m+2} &= \beta\,\sin\theta_f
\end{aligned} \tag{3.4.7}$$

Addition of equations in (3.4.7) and substitution of $|\dot{\theta}_i^+|$ from (3.4.6) in the resulting equation gives the following

$$\sum_{i=1}^{2m+2} k_i^2 = [k_1\ k_2\ \cdots\ k_{2m+2}]_2^2 = 2m \tag{3.4.8}$$

Using (3.4.8) and the property of norms it can be shown that

$$\begin{aligned}
&\sqrt{2m+2}\,[k_1\ k_2\ \cdots\ k_{2m+2}]_\infty \geqslant [k_1\ k_2\ \cdots\ k_{2m+2}]_2 \\
\Rightarrow \quad &[k_1\ k_2\ \cdots\ k_{2m+2}]_\infty \geqslant \sqrt{\frac{m}{m+1}}
\end{aligned} \tag{3.4.9}$$

It can be shown that $k_i = \sqrt{m/(m+1)}$, $i = 1,2,\cdots,(2m+2)$, satisfy (3.4.8) and minimize $[k_1\ k_2\ \cdots\ k_{2m+2}]_\infty$. Substitution of these values of k_i in (3.4.5) shows that (3.4.3) is satisfied for $(2m+2)$ impulsive inputs, *i.e.* $n = (m+1)$. It has been shown earlier in (3.3.9) that (3.4.3) is

satisfied for $N = 2$ ($n = 1$). By induction we can now claim that (3.4.3) will be satisfied for any even number of impulsive inputs.

The values of $|\,\dot{\theta}_i^+\,|$, $i = 1,2,\cdots,2n$, can be obtained from (3.4.3), (3.2.4b), and (3.2.9), namely

$$|\,\dot{\theta}_i^+\,| = \frac{1}{\sqrt{n}}\sqrt{\frac{\beta}{2m_{11}}\left(\sin\theta_f - \sin\theta_0\right)} \tag{3.4.10}$$

By substituting (3.4.10) in the energy conservation laws (similar to (3.4.7)) for $2n$ impulses and solving sequentially as shown below, we get the relations between the angles where the impulsive inputs should be applied

$$\begin{aligned}
S_1 &= S_0 \\
S_2 &= \frac{1}{2n}(S_f - S_0) + S_0 = \left[\frac{2n-2+1}{2n}\right] S_0 + \left[\frac{2-1}{2n}\right] S_f \\
S_3 &= \frac{1}{2n}(S_f - S_0) + S_2 = \left[\frac{2n-3+1}{2n}\right] S_0 + \left[\frac{3-1}{2n}\right] S_f \\
&\vdots \\
S_i &= \frac{1}{2n}(S_f - S_0) + S_{i-1} = \left[\frac{2n-i+1}{2n}\right] S_0 + \left[\frac{i-1}{2n}\right] S_f
\end{aligned} \tag{3.4.11}$$

where $S_p = \sin\theta_p, p = 1,2,\cdots f$. It can be seen that these angles satisfy 3.4.4.

It follows from (3.4.3) in Theorem 1 and (3.2.8) that all the $2n$ impulses have the same magnitude and consecutive impulses have opposite signs. Since the pendulum and wheel are both at rest at the initial time, it follows that each pair of consecutive impulses (starting with $\mathscr{I}_1$ and $\mathscr{I}_2$) result in a rest-to-rest maneuver.

It follows from (3.2.4b), (3.2.8), and (3.2.9) that the velocity of the pendulum immediately after application of an impulsive input will have opposite sign for two consecutive impulses, *i.e.*, $sign(\dot{\theta}_{k+1}^+) = -sign(\dot{\theta}_k^+)$, $k = 1,2,\cdots,(2n-1)$. Using this fact, the following algorithm can be constructed to determine the unique value of θ_i, $i = 1,2,\cdots,2n$, from (3.4.4).

If θ_f belongs to quadrant I (includes $\theta = \pi/2$) or IV, then

For $m = 1,2,\cdots,n$, compute $\sin\theta_{2m}$ using (3.4.4)

If $\sin\theta_{2m} > 0$, θ_{2m} belongs to quadrant II

Elseif $\sin\theta_m < 0$, θ_{2m} belongs to quadrant III

Else $\theta_{2m} = -\pi$.

For $m = 0, 1, \cdots, (n-1)$, compute $\sin\theta_{2m+1}$ using (3.4.4)

If $\sin\theta_{2m+1} > 0$, θ_{2m+1} belongs to quadrant I

If $\sin\theta_{2m+1} < 0$, θ_{2m+1} belongs to quadrant IV

Else $\theta_{2m+1} = 0$.

Else θ_f belongs to quadrant II or III, then

For $m = 1, 2, \cdots, n$, compute $\sin\theta_{2m}$ using (3.4.4)

If $\sin\theta_{2m} > 0$, θ_{2m} belongs to quadrant I

Elseif $\sin\theta_m < 0$, θ_{2m} belongs to quadrant IV

Else $\theta_m = 0$.

For $m = 0, 1, \cdots, (n-1)$, compute $\sin\theta_{2m+1}$ using (3.4.4)

If $\sin\theta_{2m+1} > 0$, θ_{2m+1} belongs to quadrant II

If $\sin\theta_{2m+1} < 0$, θ_{2m+1} belongs to quadrant III

Else $\theta_{2m+1} = -\pi$.

Endif

3.4.3 Rest-to-Rest Maneuvers with Odd Number of Inputs

We generalize the result presented in Remark 4.

Theorem 2. *(Lack of Optimality of Odd Impulse Sequence)*
It is not possible to design an odd impulse sequence for which the magnitudes of all the impulsive inputs are less than the optimal magnitude for the preceding and succeeding even impulse sequence. In other words, the following inequality holds for $n = 1, 2, \cdots$.

$$\mathscr{I}^{2n+1}{}_\infty > \min \mathscr{I}^{2n}{}_\infty > \min \mathscr{I}^{2n+2}{}_\infty \tag{3.4.12}$$

Proof: It is clear from (3.4.3) that $\min \mathscr{I}^{2n}{}_{\infty} > \min \mathscr{I}^{2n+2}{}_{\infty}$. We proceed to prove the left inequality by contradiction and therefore assume

$$\begin{aligned} |\mathscr{I}_i| &= k_i \min \mathscr{I}^{2n}{}_{\infty} | \quad k_i \in (0,1] \\ \Rightarrow \quad |\dot{\theta}_i^+| &= \frac{k_i}{\sqrt{n}} \sqrt{\frac{\beta}{2m_{11}} \left(\sin\theta_f - \sin\theta_0\right)} \end{aligned} \tag{3.4.13}$$

From (3.2.8), (3.4.2), and (3.4.13) we can show

$$k_1 + k_3 + \cdots k_{2n+1} = k_2 + k_4 + \cdots k_{2n} \tag{3.4.14}$$

Substituting the expression for $\dot{\theta}_i^+$ from (3.4.13) in the energy conservation laws (similar to (3.4.7)) for the $(2n+1)$ impulses, we get

$$k_1^2 + k_2^2 + \cdots k_{2n+1}^2 = 2n \tag{3.4.15}$$

Since $k_i \in (0,1]$, the following inequality holds true

$$k_1^2 + k_2^2 + \cdots k_{2n+1}^2 \leqslant k_1 + k_2 + k_3 \cdots k_{2n+1} \tag{3.4.16}$$

Using (3.4.14), and (3.4.15) we get

$$\underbrace{k_2 + k_4 + \cdots k_{2n}}_{\text{n terms}} \geqslant n \tag{3.4.17}$$

The left hand side of the inequality above is equal its right hand side $\forall\, k_q = 1, q = 2,4,\cdots 2n$. However, this choice of k_q violates (3.4.14) and (3.4.15) to be satisfied simultaneously. Therefore, (3.4.17) can be modified as

$$\underbrace{k_2 + k_4 + \cdots k_{2n}}_{\text{n terms}} > n \tag{3.4.18}$$

There exist no choice of k_q such that the above inequality holds true $\forall k_q \in (0,1]$ and thus, completes the proof by contradiction.

3.5 The Swing-Up Problem

3.5.1 Optimal Swing-Up Using Even Impulse Sequences

The swing-up problem is a rest-to-rest maneuver where the final pendulum angle is $\theta_f = \pi/2$. We consider special case where the initial angle of the pendulum is in the vertically downward configuration, *i.e.*, $\theta_0 = -\pi/2$. For swing-up using an even number of impulsive inputs, the optimal solution can be obtained from (3.4.3). For $N = 2n$, $n = 1, 2, \cdots$, the optimal solution is given by a sequence of equal and opposite impulses of the following magnitude:

$$|\mathscr{I}_i| = \frac{1}{\sqrt{n}}\mathbb{I}, \quad \forall\, i = 1, 2, \cdots, 2n, \quad \mathbb{I} \triangleq 2\sqrt{m_{11}\beta} \tag{3.5.1}$$

Since the magnitude of the impulses is inversely proportional to $\sqrt{n}$, it is clear that if the number of impulsive inputs are increased by an even number, the magnitude of each impulse in the sequence is reduced. This information will be useful for designing an impulse sequence that takes into consideration actuator saturation.

3.5.2 Implementation Using High-Gain Feedback

Ideal impulsive inputs are Dirac-delta functions and cannot be generated by actuators. In real physical systems, continuous-time implementation of impulsive inputs has be achieved using high-gain feedback in both theory and experiments [19, 23, 25]. The high-gain feedback [93] for the IWP can be obtained as

$$\tau_{hg} = [K^T M^{-1} K]^{-1}[K^T M^{-1} H + \frac{1}{\varepsilon}(\dot{\phi}_i^+ - \dot{\phi}_i^-)] \tag{3.5.2}$$

$$M = 2\begin{bmatrix} (m_{11} + m_{22}) & m_{22} \\ m_{22} & m_{22} \end{bmatrix}, \quad H = \begin{bmatrix} \beta\cos\theta \\ 0 \end{bmatrix}$$

where the matrices M and H above were reconstructed from (3.2.2), $K \triangleq \begin{bmatrix} 0 & 1 \end{bmatrix}^T$, and $\varepsilon > 0$ is a small number. Implementation of impulsive inputs using high-gain feedback also enables us to compare our results with those published in the literature. A discussion of select results in the literature is presented next.

3.5.3 Discussion of Results in the Literature

3.5.3.1 Globally Stabilizing Controller

We implemented the globally stabilizing controller in [1] using their kinematic and dynamic parameter values, which are given below

$$m_{11} = 4.83 \times 10^{-3}, \quad m_{22} = 32 \times 10^{-6}, \quad \beta = 37.9 \times 10^{-2} \tag{3.5.3}$$

Due to brevity of space, we omit complete expression of the controller used in [1]; rather, we recall the controller's structure which is in the form

$$c_0\, c_1\, \mu_0 + c_1\, \mu_1 + c_2\, \mu_2 + c_3\, \mu_3$$

where μ_0, μ_1, μ_2 and μ_3 are nonlinear functions of state variables. The controller parameters were chosen as: $c_0 = -\pi/10$, $c_1 = 13$, $c_2 = 16$ and $c_3 = 8.0$; the results are shown in Fig.3.3. The plots are slightly different from those presented in [1] but the overall trends are similar. It is clear from the plot of θ that the control input drives the pendulum directly towards the desired value of $\theta_f = \pi/2$. There is a small overshoot beyond $\pi/2$ but the wheel velocity is extremely high, of the

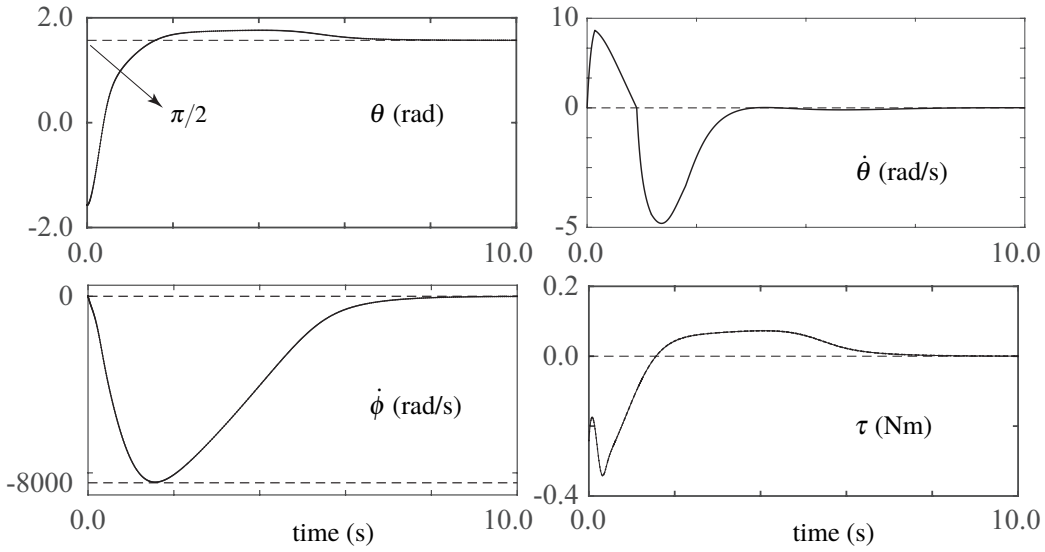

Figure 3.3: Simulation results for the globally stabilizing controller [1] with controller parameter values: $c_0 = -\pi/10$, $c_1 = 13$, $c_2 = 16$ and $c_3 = 8.0$.

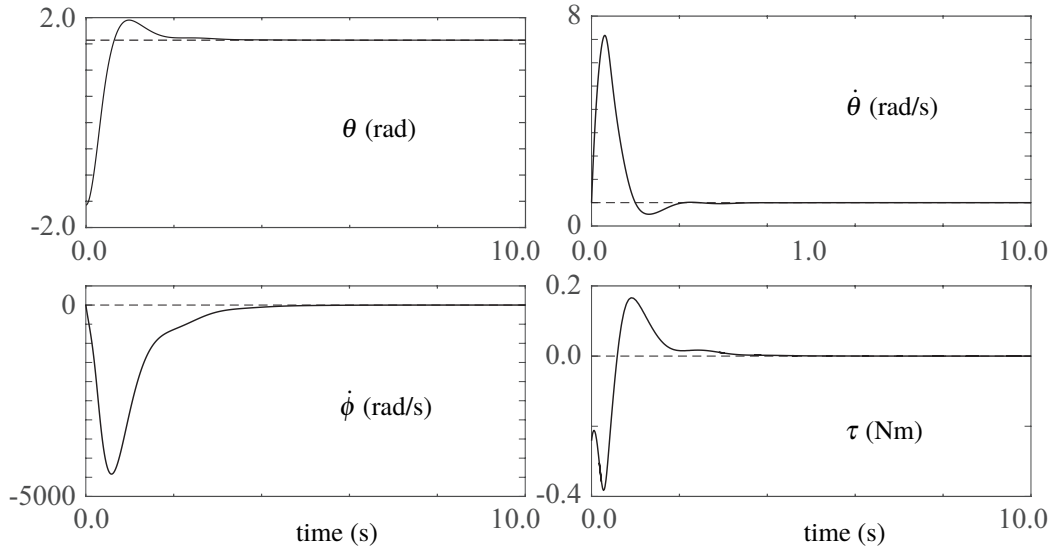

Figure 3.4: Simulation results for the globally stabilizing controller [1] with controller parameter values: $c_0 = -\pi/10$, $c_1 = 13$, $c_2 = 16$ and $c_3 = 4.5$.

order of 8000 rad/s. A change in the controller parameter c_3 from 8.0 to 4.5 increases the overshoot slightly but reduces the maximum wheel velocity by almost 50% - see Figs.3.3 and 3.4.

The above observation can be explained by the analysis presented in section 3.3 even though the nature of the inputs are completely different (continuous inputs in [1] vs a pair of impulsive inputs, $N = 2$). By changing the domain of θ from $(-3\pi/2, \pi/2]$ to $(-\pi/2, 3\pi/2]$[4] and using (3.3.1) and (3.3.8), we get for $\theta_f = \pi/2$ and $\theta_0 = -\pi/2$:

$$|\,\dot{\phi}_1^+\,| = \frac{1}{C}\sqrt{\frac{\beta}{m_{11}(1-\sin\theta_2)}} \tag{3.5.4}$$

It is clear from (3.5.4) that the wheel velocity immediately after application of the first impulse depends only on the angle where the second impulse is applied, namely θ_2, and tends to infinity when $\theta_2 = \pi/2^+$, *i.e.*, when the overshoot approaches zero. While it is clear from (3.5.4) that $\theta_2 = \pi/2^+$ is not a good choice for application of the second impulse, the value of θ_2 that minimizes the magnitude of the wheel velocity $|\,\dot{\phi}_1^+\,|$ can be obtained using the energy conservation law in

[4]This change in the domain is necessary to ensure that the trajectory of θ is similar to that in [1] but it does not change the analysis whatsoever.

(3.2.6a). For the IWP to cross the upright configuration, the following inequality must be satisfied:

$$m_{11}\dot{\theta}_1^{+\,2} + \beta \sin\theta_0 > \beta \quad \Rightarrow \quad |\,\dot{\phi}_1^{+}\,| > \frac{1}{C}\sqrt{2\beta/m_{11}} \tag{3.5.5}$$

where $\theta_0 = -\pi/2$ and (3.3.1) were used. Comparing (3.5.4) and (3.5.5), we can show that $\theta_2 = (5\pi/6)^-$ minimizes $|\,\dot{\phi}_1^{+}\,|$.

A simulation was performed using the high-gain feedback law in (3.5.2) with $\varepsilon = 0.01$, the parameter values in (3.5.3), and $\theta_2 \approx 3\pi/4$ (slightly less that $5\pi/6$); the results are shown in Fig.3.5. After the IWP reached a neighborhood of $\theta_f = \pi/2$, a linear controller was invoked for stabilization. The linear controller was designed to place the poles of the closed loop system at $-4 \pm 2i$ and -8. The simulation results indicate that swing-up is achieved in less than 1.0 s, which is much faster than that achieved in [1]. The maximum velocity of the wheel is still quite high (3000 rad/s) but it is significantly lower than that in Fig.3.3. The torque required is quite high ($\approx$ 13 Nm) but this can be reduced significantly by simply changing the domain of θ_2, as we will show in the next simulation.

The simulation results presented in Fig.3.5 were obtained by assuming $\theta \in (-\pi/2, 3\pi/2]$; this was motivated by the need to generate trajectories of the IWP similar to those generated in [1], for

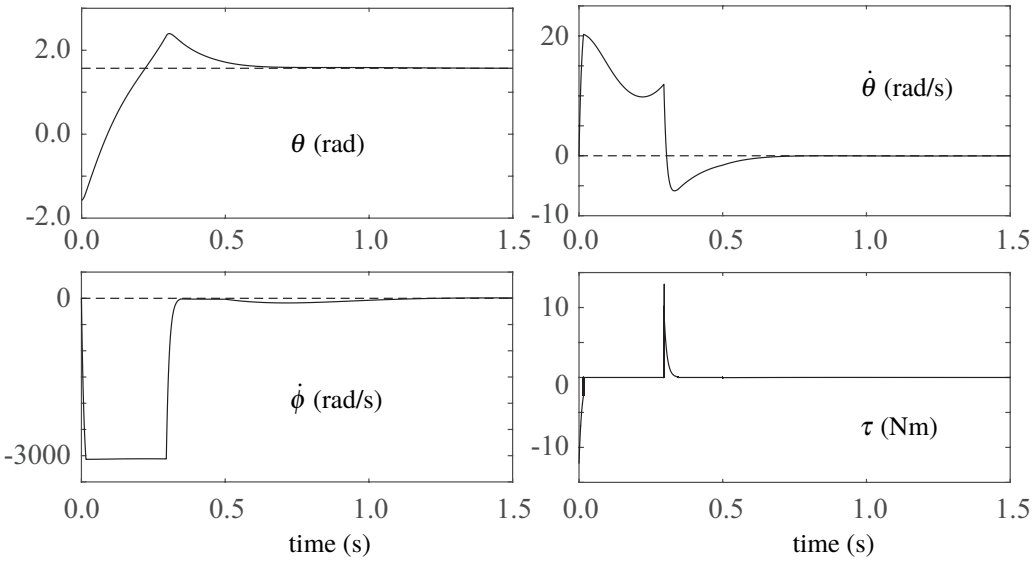

Figure 3.5: High-gain feedback implementation of two impulsive inputs ($N = 2$) for swing-up of the IWP. For the purpose of comparison with the results in Figs.3.3 and 3.4, the controller is designed to keep θ in the domain $(-\pi/2, 3\pi/2]$.

comparison. If we switch the domain of θ back to $(-3\pi/2, \pi/2]$, as defined in section 3.2.3, the maximum wheel speed and the magnitude of the maximum torque can both be reduced from their values in Fig.3.5. Simulation results of high-gain feedback implementation of the optimal impulse sequence based on two inputs, described by (3.4.3) and (3.4.4) with $n = 1$, is shown in Fig.3.6. The high-gain controller was implemented using $\varepsilon = 0.02$ and stabilization of the equilibrium was achieved by the same linear controller that was used in the last simulation. It can be seen from Fig.3.6 that the second impulse is applied when $\theta_2 \approx -\pi$ rad. Similar to the results in Fig.3.5, swing-up is achieved in less than 1.0 s, but the maximum wheel velocity is now reduced from 3000 rad/s to 2000 rad/s and magnitude of the maximum torque is reduced from ≈ 13 Nm to ≈ 3 Nm.

The maximum torque of ≈ 3 Nm in Fig.3.6, although larger than those reported in the literature, is not a significant concern because it is applied for a very short duration of time. Motors can apply substantially larger torques[5] than their maximum continuous torque over short time intervals. The maximum torque of ≈ 3 Nm also corresponds to the continuous-time implementation of the optimal $\mathscr{I}^2$. The magnitude of this torque, as well as the maximum velocity of the wheel, can

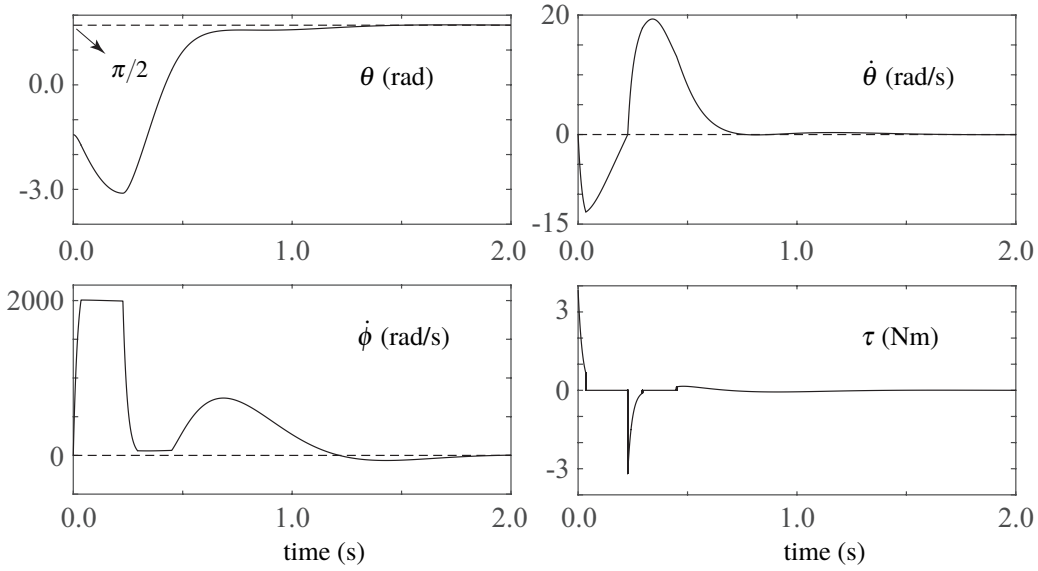

Figure 3.6: High-gain feedback implementation of the sequence of two optimal impulsive inputs ($N = 2$) for swing-up of the IWP. The controller is designed to keep θ in the domain $(-3\pi/2, \pi/2]$.

[5]This is referred to a peak torque [94]; for different motors, the peak torque can be twice to ten times larger than the maximum continuous torque.

be easily reduced if we consider continuous-time implementation of $\mathscr{I}^{2n}$, $n = 2, 3, \cdots$. This is discussed in the next section.

Our results are not compared with those obtained using the IDA-PBC method, [15, 43], for example, due to space constraints. Similar to the globally stabilizing controller [1], the IDA-PBC method also takes the pendulum directly to the desired upright configuration and results in a large continuous torque [15] or large wheel velocity [43] during swing-up.

3.5.3.2 Energy Based Controller

When the number of impulses are increased from $N = 2$ to $N = 8$, for example, the magnitude of the impulsive torques are reduced by a factor of $\sqrt{4} = 2$; consequently, the magnitude of the maximum high-gain torque and the wheel velocity are reduced proportionately - see Fig.3.7. The trajectories of the state variables in Fig.3.7 resemble those of the energy based controllers [2, 68] during swing-up phase of the IWP; the PFBLC + AL energy-based controller presented in [2] is simulated here to show the similarities in the trajectories - see Fig.3.8. It can be seen from Figs.3.7 and 3.8, that, unlike the globally stabilizing controller [1] (see Fig.3.3) where the pendulum is aggressively driven towards its desired configuration, both controllers (presented here and in [2])

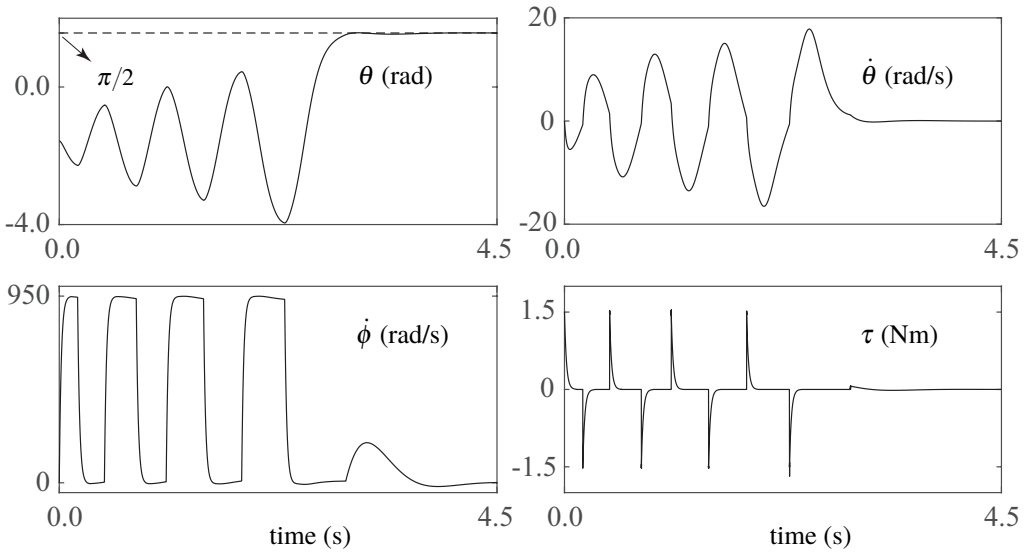

Figure 3.7: High-gain feedback implementation of the sequence of eight optimal impulsive inputs ($N = 8$) for swing-up of the IWP. The high-gain controller was implemented with $\varepsilon = 0.02$.

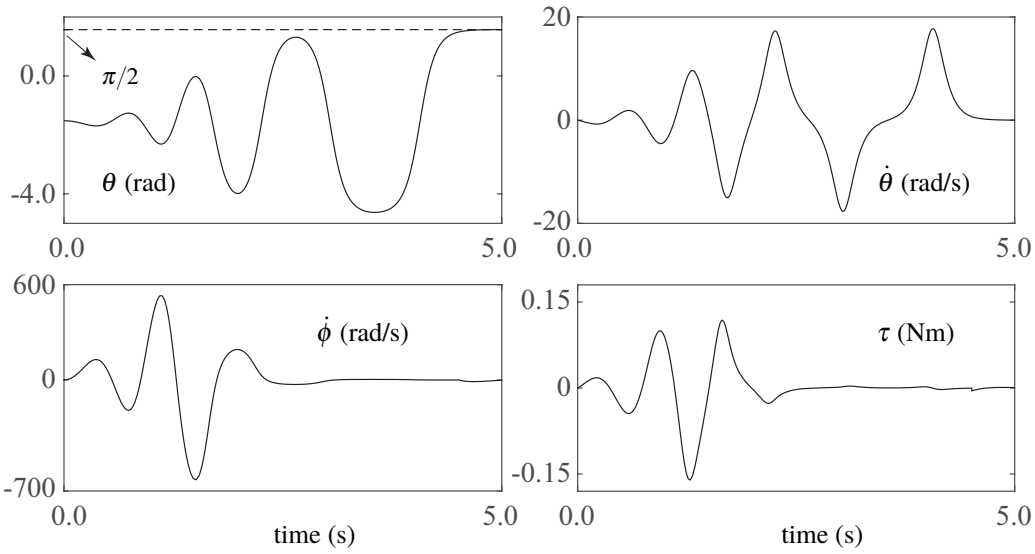

Figure 3.8: Simulation using the PFBLC + AL controller in [2]; the controller parameters were chosen as $k_e = 3.1 \times 10^7$ and $k_v = 0.1$. This choice of parameters ensured that the time required for swing-up and the magnitude of the maximum control torque in simulations matched those of the experiments. The initial configuration was chosen to be slightly different from $\theta_0 = -\pi/2$ since the controller is unable to swing-up from this configuration.

gradually add energy to the pendulum over several cycles of oscillation.

Table 3.1: Swing-up time and maximum magnitude of high-gain torque required for different values of N

N	2	4	6	8	10	12
t_s (s)	0.6	1.36	1.96	2.90	3.67	4.53
$\max_{t_0 \leqslant t \leqslant t_f} \lvert\tau_{hg}\rvert$ (Nm)	3.0	2.12	1.73	1.50	1.35	1.20

A comparison of Figs.3.7 and 3.8 indicates that the magnitude of the maximum torque required by our method is larger than that required by the approach proposed in [2]. However, since the torques are applied intermittently over very short intervals of time, feasibility of our approach is determined by the peak torque rating of the actuator as opposed to the maximum continuous torque rating, which is always lower [94]. A salient feature of our approach is that, given any actuator, an optimal impulse sequence can be designed such that the peak torque rating of the motor is not exceeded. A higher value of N reduces the peak torque requirement of the motor but increases the

time time required for swing-up. The swing-up time and the magnitude of the maximum torque for several different values of N are presented in Table 6.1.

CHAPTER 4

IMPULSIVE CONTROL OF A DEVIL-STICK: PLANAR SYMMETRIC JUGGLING

4.1 Introduction

The problem of juggling a devil-stick is investigated. Assuming that the stick remains confined to the vertical plane, the task is to juggle between two symmetric configurations. Impulsive forces are applied to the stick intermittently and the impulse of the force and its point of application are modeled as inputs to the system. The juggling problem is formally described in section 4.2. The dynamics of the devil-stick is presented in section 4.3; it is comprised of impulsive dynamics due to the control inputs and continuous dynamics due to torque-free motion under gravity. A coordinate transformation is used to simplify the control problem and the dynamics is described by a nonlinear discrete-time system. The control design is provided in section 4.4. By choosing one of the control inputs to be dead-beat, the nonlinear system is simplified to a linear discrete-time system. For stable juggling, the linear system is controlled using linear quadratic regulator (LQR) and model predictive control (MPC) techniques. Simulation results are presented in section 4.5.

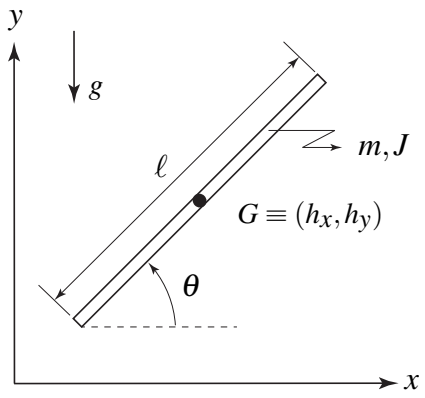

Figure 4.1: A three degree-of-freedom of a devil-stick.

4.2 Problem Description

Consider the three degree-of-freedom devil-stick shown in Fig. 4.1, which can move freely in the xy vertical plane. The stick has length ℓ, mass m, and mass moment of inertia J about its center-of-mass G. The configuration of the stick is described by the three generalized coordinates: (θ, h_x, h_y), where θ is the orientation of the stick with respect to the positive x axis, measured counter-clockwise, and (h_x, h_y) are the Cartesian coordinates of G. The objective is to juggle the stick between two configurations that are symmetric with respect to the vertical axis. The coordinates of the stick in these two configurations are (θ^*, h_x^*, h_y^*) and $(\pi - \theta^*, -h_x^*, h_y^*)$, where $\theta^* \in (0, \pi/2)$ - see Fig. 4.2. It is assumed that juggling is achieved by applying impulsive forces perpendicular to the stick; they are applied only when the orientation of the stick is $\theta = \theta^*$ or $\theta = \pi - \theta^*$. Therefore, the time of application of the impulsive force is not a part of the control design. The control inputs are the pair (I, r), where I, $I \geqslant 0$, is the impulse of the impulsive force and r is the distance of the point of application of the force from G. The value of r is considered to be positive if the angular impulse of the impulsive force about G is in the positive z direction when $\theta = \theta^*$, and is in the negative z direction when $\theta = \pi - \theta^*$. The control inputs that juggle the stick between the symmetric configurations are denoted by the pair (I^*, r^*).

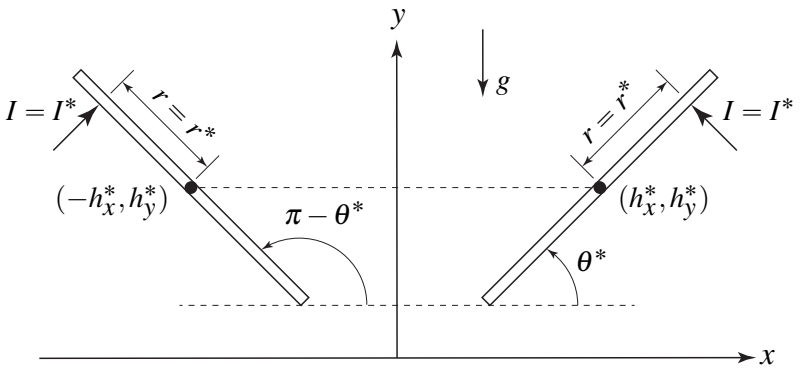

Figure 4.2: Symmetric configurations of the devil-stick in Fig. 4.1.

4.3 Dynamics of the Devil-Stick

4.3.1 Impulsive Dynamics

The dynamics of the three-DOF devil-stick is described by the six-dimensional state vector X, where

$$X = \begin{bmatrix} \theta & \omega & h_x & v_x & h_y & v_y \end{bmatrix}^T, \ \omega \triangleq \dot{\theta}, \ v_x \triangleq \dot{h}_x, \ v_y \triangleq \dot{h}_y$$

Let t_k, $k = 1,2,3,\cdots$, denote the instants of time when the impulsive inputs are applied. Furthermore, without loss of generality, let $k = (2n-1)$, $n = 1,2,\cdots$ denote the instants of time when the impulsive inputs are applied at $\theta = \theta^*$, and $k = 2n$, $n = 1,2,\cdots$ denote the instants of time when the impulsive inputs are applied at $\theta = \pi - \theta^*$. If t_k^- and t_k^+ denote the instants of time immediately before and after application of the impulsive inputs, the linear and angular impulse-momentum relationships can be used to describe the impulsive dynamics[1] as follows, for $k = 1,3,5,\cdots$

$$X(t_k^+) = X(t_k^-) + \begin{bmatrix} 0 \\ (I_k r_k / J) \\ 0 \\ -(I_k/m)\sin\theta^* \\ 0 \\ (I_k/m)\cos\theta^* \end{bmatrix} \tag{4.3.1}$$

and for $k = 2,4,6,\cdots$

$$X(t_k^+) = X(t_k^-) + \begin{bmatrix} 0 \\ -(I_k r_k / J) \\ 0 \\ (I_k/m)\sin\theta^* \\ 0 \\ (I_k/m)\cos\theta^* \end{bmatrix} \tag{4.3.2}$$

[1] Impulsive inputs cause discontinuous jumps in the velocity coordinates but no change in the position coordinates. The dynamics of underactuated systems subjected to impulsive inputs is discussed in [6, 25, 74, 95].

where (I_k, r_k) denote the control inputs at time t_k. Between two consecutive impulsive inputs, the devil-stick undergoes torque-free motion under gravity; this is discussed next.

4.3.2 Continuous-time Dynamics

Over the interval $t \in [t_k^+, t_{k+1}^-]$, the devil-stick will be in flight; its center-of-mass G will undergo projectile motion and its angular momentum will remain conserved. This dynamics is described by the differential equation:

$$\dot{X} = \begin{bmatrix} \omega & 0 & v_x & 0 & v_y & -g \end{bmatrix}^T \tag{4.3.3}$$

where the initial condition $X(t_k^+)$ can be obtained from (4.3.1) or (4.3.2), depending on whether k is odd or even.

4.3.3 Poincaré Sections and Half-Return Maps

For the hybrid system, described by impulsive dynamics of section 4.3.1 and continuous dynamics of section 4.3.2, we define two Poincaré sections[2,3] [96] S_r and S_l as follows:

$$\begin{aligned} S_r &: \{X \in \mathbb{R}^6 \mid \theta = \theta^*\} \\ S_l &: \{X \in \mathbb{R}^6 \mid \theta = \pi - \theta^*\} \end{aligned} \tag{4.3.4}$$

These Poincaré sections are chosen since the impulsive inputs are applied only when θ is equal to θ^* or $(\pi - \theta^*)$. Any point on S_r and S_l can be described by the vector Y, $Y \subset X$, where

$$Y = \begin{bmatrix} \omega & h_x & v_x & h_y & v_y \end{bmatrix}^T \tag{4.3.5}$$

The map $\mathbb{P}_r : S_r \rightarrow S_l$ can be determined from (4.3.1) and (4.3.3) as follows:

$$Y(t_{k+1}^-) = A\,Y(t_k^-) + B_r \tag{4.3.6}$$

[2]Poincaré sections have been previously used for design of gaits for bipedal robots [76, 80].

[3]It is assumed that the initial conditions of the devil-stick are such that its trajectory intersects one of the two Poincaré sections before the first impulsive control input is applied.

$$A \triangleq \begin{bmatrix} 1 & 0 & 0 & 0 & 0 \\ 0 & 1 & \delta_k & 0 & 0 \\ 0 & 0 & 1 & 0 & 0 \\ 0 & 0 & 0 & 1 & \delta_k \\ 0 & 0 & 0 & 0 & 1 \end{bmatrix}, B_r \triangleq \begin{bmatrix} (I_k r_k/J) \\ -(I_k/m)\sin\theta^* \delta_k \\ -(I_k/m)\sin\theta^* \\ (I_k/m)\cos\theta^* \delta_k - (1/2) g\, \delta_k^2 \\ (I_k/m)\cos\theta^* - g\delta_k \end{bmatrix}$$

where $\delta_k \triangleq (t_{k+1}^- - t_k^-)$ and $k = (2n-1)$, $n = 1, 2, \cdots$. Similarly, the map $\mathbb{P}_l : S_l \to S_r$ can be determined from (4.3.2) and (4.3.3) as follows

$$Y(t_{k+1}^-) = A\, Y(t_k^-) + B_l \tag{4.3.7}$$

$$B_l \triangleq \begin{bmatrix} -(I_k r_k/J) \\ (I_k/m)\sin\theta^* \delta_k \\ (I_k/m)\sin\theta^* \\ (I_k/m)\cos\theta^* \delta_k - (1/2) g\, \delta_k^2 \\ (I_k/m)\cos\theta^* - g\delta_k \end{bmatrix}$$

where $k = 2n$, $n = 1, 2, \cdots$. Both $\mathbb{P}_r$ and $\mathbb{P}_l$ in (4.3.6) and (4.3.7), respectively, can be viewed as half-return maps[4] since the composition of these maps are the return maps $\mathbb{P}_r \circ \mathbb{P}_l : S_l \to S_l$ and $\mathbb{P}_l \circ \mathbb{P}_r : S_r \to S_r$. In the next section we introduce a coordinate transformation to show that the map $\mathbb{P}_l$, in the transformed coordinates, is identical to $\mathbb{P}_r$. This simplifies the analysis of the problem.

4.3.4 Coordinate Transformation

Consider Fig. 4.3, where $z = 0$ denotes the xy plane in which the devil-stick is juggled. Typically, the juggler will stand at a point on the positive z axis, denoted by P in Fig. 4.3 (a), and face the $z = 0$ plane. The juggler will apply a control action with the right hand when $\theta = \theta^*$, and with the left hand when $\theta = \pi - \theta^*$, *i.e.*, the juggler is ambidextrous. Instead of alternating between the right and left hands, the juggler can choose to apply all control actions using the right hand only.

[4]Half-return maps have been used to analyze the behavior of dynamical systems such as the van der Pol oscillator [97, 98].

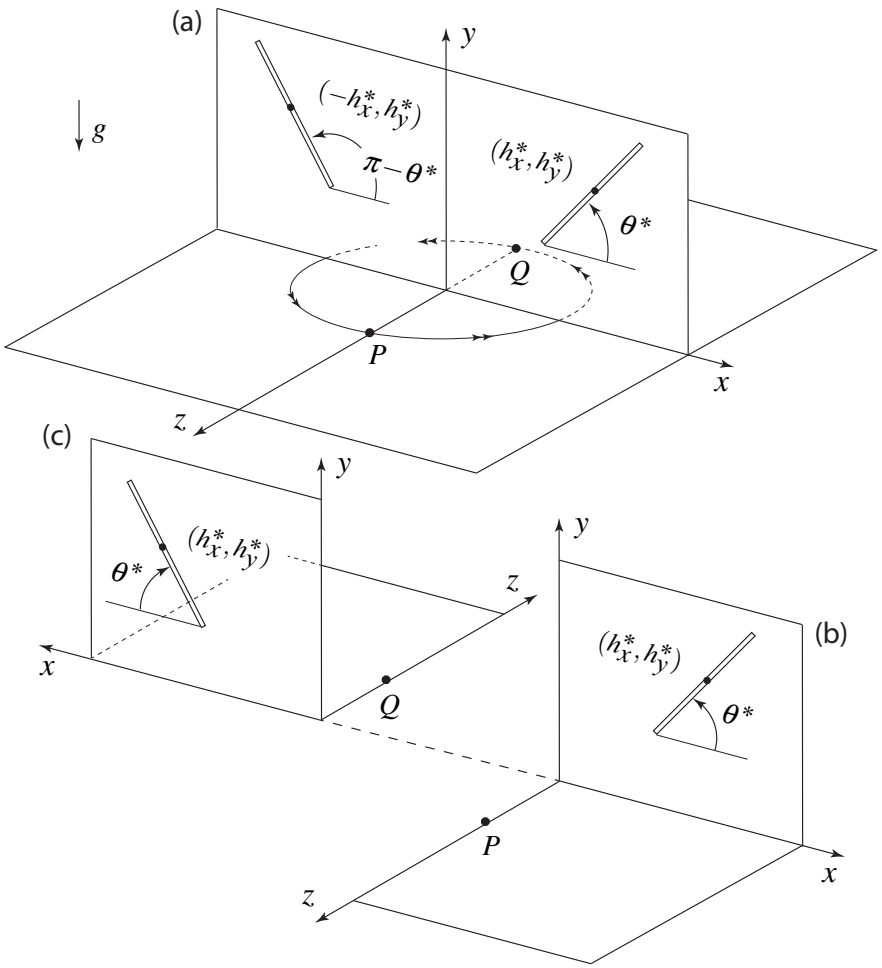

Figure 4.3: (a) Ambidexterous juggler standing at P and applying control actions with both hands, (b) right-handed juggler standing at P and applying control action with right hand, (c) right-handed juggler standing at Q and applying control action with right hand.

This juggler, whom we will now refer to as the right-handed juggler, To this end, the juggler will apply the control action standing at P when $\theta = \theta^*$ - see Fig. 4.3 (b), and apply the next control action after changing location to Q (mirror image of P) and facing the $z = 0$ plane when $\theta = \pi - \theta^*$ - see Fig. 4.3 (c). When the devil stick has the orientation $\theta = \pi - \theta^*$, as seen by an observer at P, it will have the orientation $\theta = \theta^*$ for the right-handed juggler. After applying control action at Q, the right-handed juggler will return back to P. If xyz denotes the rotating coordinate frame of the right-handed juggler, the change in position of this juggler can be described by the coordinate

transformation:

$$\begin{bmatrix} x \\ y \\ z \end{bmatrix}_Q = R_{y,\pi} \begin{bmatrix} x \\ y \\ z \end{bmatrix}_P, \quad \begin{bmatrix} x \\ y \\ z \end{bmatrix}_P = R_{y,\pi} \begin{bmatrix} x \\ y \\ z \end{bmatrix}_Q$$

where

$$R_{y,\pi} \triangleq diag[-1, \quad 1, \quad -1]$$

Since $R_{y,\pi}$ changes the sign of the x and z coordinates and leaves the y coordinate unchanged, we can show

$$Y_Q = RY_P, \quad Y_P = RY_Q$$

where

$$R = R^{-1} \triangleq diag[-1, \quad -1, \quad -1, \quad 1, \quad 1]$$

and Y_P and Y_Q denote the vector Y as seen by the right-handed juggler standing at points P and Q, respectively.

4.3.5 Single Return Map and Discrete-Time Model

In the reference frame of the right-handed juggler, who alternates between positions P and Q, the two Poincaré sections S_l and S_r are identical, and equal to

$$S : \{X \in \mathbb{R}^6 \mid \theta = \theta^*\} \tag{4.3.8}$$

This follows from our discussion in section 4.3.4 as well as Figs. 4.3 (b) and (c). The half-return maps $\mathbb{P}_r$ and $\mathbb{P}_l$ in (4.3.6) and (4.3.7) can be rewritten as follows:

$$Y_P(t_{k+1}^-) = AY_P(t_k^-) + B_r, \quad k = 1,3,5,\cdots \tag{4.3.9a}$$

$$Y_P(t_{k+1}^-) = AY_P(t_k^-) + B_l, \quad k = 2,4,6,\cdots \tag{4.3.9b}$$

to explicitly indicate the reference frame of Y. Since the right-handed juggler alternates between positions P and Q, the half-return map $\mathbb{P}_l$ in (4.3.9b) can be transformed as follows:

$$\begin{aligned} & RY_P(t_{k+1}^-) = RA\,Y_P(t_k^-) + RB_l \\ \Rightarrow \quad & Y_Q(t_{k+1}^-) = AR\,Y_P(t_k^-) + RB_l \\ \Rightarrow \quad & Y_Q(t_{k+1}^-) = A\,Y_Q(t_k^-) + B_r, \quad k = 2,4,6,\cdots \end{aligned} \tag{4.3.10}$$

where we used the relations $RA = AR$ and $RB_l = B_r$. It is clear from (4.3.9a) and (4.3.10) that the half-return maps $\mathbb{P}_r$ and $\mathbb{P}_l$ in (4.3.6) and (4.3.7) are identical in the reference frame of the right-handed juggler. This implies that the hybrid dynamics of the devil-stick between any two control actions can be described by a single return map if the change in reference frame of the right-handed juggler is incorporated in the dynamic model. This map, $\mathbb{P} : S \to S$, can be obtained by first rewriting the left-hand-sides of (4.3.6), (4.3.9a) and (4.3.10) as follows:

$$\begin{aligned} & RY_Q(t_{k+1}^-) = A\,Y_P(t_k^-) + B_r, \qquad k = 1,3,5,\cdots \\ \Rightarrow \quad & Y_Q(t_{k+1}^-) = R\left[A\,Y_P(t_k^-) + B_r\right], \quad k = 1,3,5,\cdots \end{aligned} \tag{4.3.11a}$$

$$\begin{aligned} & RY_P(t_{k+1}^-) = A\,Y_Q(t_k^-) + B_r, \qquad k = 2,4,6,\cdots \\ \Rightarrow \quad & Y_P(t_{k+1}^-) = R\left[A\,Y_Q(t_k^-) + B_r\right], \quad k = 2,4,6,\cdots \end{aligned} \tag{4.3.11b}$$

Then, by accounting for the change in reference frame of the right-handed juggler after each control action, (4.3.11a) and (4.3.11b) can be combined into the following single equation which represents the return map $\mathbb{P}$:

$$\bar{Y}(t_{k+1}^-) = R\left[A\bar{Y}(t_k^-) + B_r\right], \qquad k = 1,2,3,\cdots$$

where $\bar{Y}$ denotes the state vector Y in the reference frame of the right-handed juggler. The above equation results in the following discrete-time equations:

$$\omega(t_{k+1}^-) = -\omega(t_k^-) - (I_k\, r_k/J) \tag{4.3.12a}$$

$$h_x(t_{k+1}^-) = -h_x(t_k^-) - \left[v_x(t_k^-) - (I_k/m)\sin\theta^*\right]\delta_k \tag{4.3.12b}$$

$$v_x(t_{k+1}^-) = -v_x(t_k^-) + (I_k/m)\sin\theta^* \tag{4.3.12c}$$

$$h_y(t_{k+1}^-) = h_y(t_k^-) - (1/2)g\,\delta_k^2 + \left[v_y(t_k^-) + (I_k/m)\cos\theta^*\right]\delta_k \tag{4.3.12d}$$

$$v_y(t_{k+1}^-) = v_y(t_k^-) + (I_k/m)\cos\theta^* - g\,\delta_k \tag{4.3.12e}$$

where $\delta_k \triangleq (t_{k+1}^- - t_k^-)$, $k = 1, 2, \cdots$, is the time of flight between two consecutive control actions. During this time duration, the devil-stick rotates by a net angle $\pi - 2\theta^*$. Since the angular velocity of the stick remains constant in the interval $[t_k^+, t_{k+1}^-]$, δ_k is given as follows

$$\delta_k = \frac{\Delta\theta}{\omega(t_k^-) + (I_k\, r_k/J)}, \quad \Delta\theta \triangleq (\pi - 2\theta^*) \tag{4.3.13}$$

The control design for juggling is presented next.

4.4 State Feedback Control Design

4.4.1 Steady-State Dynamics

From the discussion in section 4.3.5 it becomes clear that when the change of reference frame of the juggler is taken into account, the problem of juggling between the two distinct configurations (θ^*, h_x^*, h_y^*) and $(\pi - \theta^*, -h_x^*, h_y^*)$ is converted to the problem of juggling between identical configurations (θ^*, h_x^*, h_y^*) and (θ^*, h_x^*, h_y^*). If the state variables at this configuration are denoted by

$$\bar{Y}^* \triangleq \begin{bmatrix} \omega^* & h_x^* & v_x^* & h_y^* & v_y^* \end{bmatrix}^T \tag{4.4.1}$$

then $\bar{Y}^* = \mathbb{P}(\bar{Y}^*)$ is a fixed point and (4.3.12) and (4.3.13) give

$$\omega^* = -\omega^* - (I_k^* r_k^*/J) \tag{4.4.2a}$$

$$h_x^* = -h_x^* - \left[v_x^* - (I_k^*/m)\sin\theta^*\right]\delta^* \tag{4.4.2b}$$

$$v_x^* = -v_x^* + (I_k^*/m)\sin\theta^* \tag{4.4.2c}$$

$$h_y^* = h_y^* - (1/2)g\,\delta^{*2} + \left[v_y^* + (I_k^*/m)\cos\theta^*\right]\delta^* \tag{4.4.2d}$$

$$v_y^* = v_y^* + (I_k^*/m)\cos\theta^* - g\,\delta^* \tag{4.4.2e}$$

$$\delta^* = \frac{\Delta\theta}{\omega^* + (I_k^* r_k^*/J)} \tag{4.4.2f}$$

where I_k^*, r_k^* denote the steady-state values of the control inputs and δ^* denote the steady-state value of the time of flight. Since h_y^* is eliminated from (4.4.2d), (4.4.2) represents six equations in seven unknowns, namely, ω^*, h_x^*, v_x^*, v_y^*, I^*, r^*, and δ^*. By choosing δ^*, the remaining six unknowns are obtained as follows:

$$\begin{aligned}
&\omega^* = -\Delta\theta/\delta^*, \qquad h_x^* = g\,\delta^{*2}\tan\theta^*/4 \\
&v_x^* = g\tan\theta^*\delta^*/2,\; v_y^* = -g\,\delta^*/2 \\
&I^* = mg\delta^*/\cos\theta^*, r^* = 2J\cos\theta^*\Delta\theta/(mg\delta^{*2})
\end{aligned} \tag{4.4.3}$$

Since the point of application of the impulsive force must lie on the stick, r^* in (4.4.3) must satisfy $0 < r^* < \ell/2$. This imposes the following constraint of the value of δ^*:

$$\delta^* > \bar{\delta}, \quad \bar{\delta} \triangleq 2\sqrt{\frac{J\cos\theta^*\Delta\theta}{mg\ell}} \tag{4.4.4}$$

It should be noted that for a given value of δ^*, the value of h_y^* is not unique.

4.4.2 Error Dynamics

To converge the states to their desired values, we first define the discrete error variables:

$$\begin{aligned}
&\widetilde{\omega}(k) \triangleq \omega(t_k^-) - \omega^* \\
&\widetilde{h}_x(k) \triangleq h_x(t_k^-) - h_x^*, \qquad \widetilde{v}_x(k) \triangleq v_x(t_k^-) - v_x^* \\
&\widetilde{h}_y(k) \triangleq h_y(t_k^-) - h_y^*, \qquad \widetilde{v}_y(k) \triangleq v_y(t_k^-) - v_y^* \\
&\widetilde{u}_1(k) \triangleq (I_k r_k - I^* r^*)/J, \quad \widetilde{u}_2(k) \triangleq (I_k - I^*)/m
\end{aligned} \tag{4.4.5}$$

Using (4.3.12) and (4.4.2a)-(4.4.2e), the error dynamics can now be written as

$$\widetilde{\omega}(k+1) = -\widetilde{\omega}(k) - \widetilde{u}_1(k) \tag{4.4.6a}$$

$$\widetilde{h}_x(k+1) = -\widetilde{h}_x(k) - \delta_k \widetilde{v}_x(k) + \delta_k \sin\theta^* \widetilde{u}_2(k) \tag{4.4.6b}$$

$$\widetilde{v}_x(k+1) = -\widetilde{v}_x(k) + \sin\theta^* \widetilde{u}_2(k) \tag{4.4.6c}$$

$$\widetilde{h}_y(k+1) = \widetilde{h}_y(k) + \delta_k \widetilde{v}_y(k) + \delta_k \cos\theta^* \widetilde{u}_2(k) + (g/2)\left[\delta_k \delta_k^* - \delta_k^2\right] \tag{4.4.6d}$$

$$\widetilde{v}_y(k+1) = \widetilde{v}_y(k) + \cos\theta^* \widetilde{u}_1(k) - g\left[\delta_k - \delta_k^*\right] \tag{4.4.6e}$$

where δ_k, defined in (4.3.13), can be written in terms of the error variables as follows:

$$\delta_k = \frac{\Delta\theta\, \delta^*}{\left[\widetilde{\omega}(k) + \widetilde{u}_1(k)\right]\delta^* + \Delta\theta} \tag{4.4.7}$$

It is clear from (4.4.6) and (4.4.7) that the error dynamics is nonlinear. In the next section we present a partial control design that converts the nonlinear system into a linear system and simplifies the remaining control design.

4.4.3 Partial Control Design: Dead-Beat Control

The error dynamics in (4.4.6) involves two control inputs, namely, $\widetilde{u}_1(k)$ and $\widetilde{u}_2(k)$. The input $\widetilde{u}_1(k)$ appears only in (4.4.6a). To this end, we first design $\widetilde{u}_1(k)$ as follows:

$$\widetilde{u}_1(k) = -\widetilde{\omega}(k) \tag{4.4.8}$$

to guarantee dead-beat convergence of the error state $\widetilde{\omega}(k)$. Substitution of (4.4.8) in (4.4.7) yields $\delta_k = \delta^*$. Since, δ^* is user-defined and is a constant, the choice of control in (4.4.8) is special as it

transforms the remaining dynamics in (4.4.6b)-(4.4.6e) into the linear system:

$$
\begin{aligned}
&z(k+1) = \mathscr{A}\, z(k) + \mathscr{B}\, \widetilde{u}_2(k) \\
&z(k) \triangleq \begin{bmatrix} \widetilde{h}_x(k) & \widetilde{v}_x(k) & \widetilde{h}_y(k) & \widetilde{v}_y(k) \end{bmatrix}^T \\
&\mathscr{A} \triangleq \begin{bmatrix} -1 & -\delta^* & 0 & 0 \\ 0 & -1 & 0 & 0 \\ 0 & 0 & 1 & \delta^* \\ 0 & 0 & 0 & 1 \end{bmatrix}, \quad \mathscr{B} \triangleq \begin{bmatrix} \delta^* \sin\theta^* \\ \sin\theta^* \\ \delta^* \cos\theta^* \\ \cos\theta^* \end{bmatrix}
\end{aligned}
\tag{4.4.9}
$$

It can be verified that the pair $(\mathscr{A}, \mathscr{B})$ is controllable since $\theta^* \in (0, \pi/2)$ and $\delta^* > 0$.

4.4.4 Residual Control Design

The error dynamics in (4.4.9) is linear and therefore the states can be converged to zero by simply designing a linear controller. However, it should be noted that the control input $\widetilde{u}_2(k)$ determines the value of I_k which also appears in the dead-beat control design $\widetilde{u}_1(k)$ - see (4.4.5). By using the values of $\widetilde{u}_2(k)$ from (4.4.5) in (4.4.8), we get:

$$
r_k = \left[I^* r^* - J\widetilde{\omega}(k) \right] / I_k \tag{4.4.10}
$$

Since the point of application of impulsive force must lie of the stick, r_k must satisfy $-\ell/2 < r_k < \ell/2$. By imposing this condition on the value of r_k in (4.4.10), we get the following constraints on the input $\widetilde{u}_2(k)$:

$$
\begin{aligned}
\widetilde{u}_2(k) &> \left[2I^* r^* - 2J\widetilde{\omega}(k) - I^* \ell \right] / (m\ell) \\
\widetilde{u}_2(k) &> \left[-2I^* r^* + 2J\widetilde{\omega}(k) - I^* \ell \right] / (m\ell)
\end{aligned}
\tag{4.4.11}
$$

Since I^* and r^* are both positive, as it can be seen from (4.4.3), the inequalities in (4.4.11) can be combined into the single inequality:

$$
\begin{aligned}
&\widetilde{u}_2(k) > \bar{a} + \bar{b}\, |\, \widetilde{\omega}(k)\, | \\
&\bar{a} \triangleq (2r^* - \ell) I^* / (m\ell), \quad \bar{b} \triangleq 2J/(m\ell)
\end{aligned}
\tag{4.4.12}
$$

Since $\widetilde{u}_1(k)$ is dead-beat, $\widetilde{\omega}(k) = 0, k = 2,3\cdots$. Thus, (4.4.12) can also be written as

$$\begin{aligned} \widetilde{u}_2(k) &> \bar{a} + \bar{b} \mid \widetilde{\omega}(k) \mid, \qquad k = 1 \\ \widetilde{u}_2(k) &> \bar{a}, \qquad\qquad\qquad\quad k = 2,3,\cdots \end{aligned} \tag{4.4.13}$$

The input $\widetilde{u}_2(k)$ is designed using Linear Quadratic Regulator (LQR) and Model Predictive Control (MPC) methods. For an LQR design, the control minimizes the cost function

$$J = \sum_{k=1}^{\infty} \left[z(k)^T Q z(k) + R \widetilde{u}_2^2(k) \right] \tag{4.4.14}$$

where, Q and R are constant weighting matrices that can be chosen by trial and error to satisfy the constraints in (4.4.13). The closed-form solution of the control input $\widetilde{u}_2(k)$ can be obtained by solving the Ricatti equation [99].

For a receding horizon MPC design, the constraint in (4.4.13) can be explicitly included in the optimization problem. In the MPC design[5], it is necessary to calculate the predicted output with future control input as the adjusted variable. Since the current control input cannot affect the output at the same time for receding horizon control, the system dynamics must be represented in terms of the difference between the current and the predicted control input. To this end, we define the following variables based on the augmented state-space model[6] in [100]:

$$\begin{aligned} &\Delta u(k_i) \triangleq \widetilde{u}_2(k_i) - \widetilde{u}_2(k_i - 1) \\ &\Delta U_i \triangleq \begin{bmatrix} \Delta u(k_i) \\ \Delta u(k_i + 1) \\ \vdots \\ \Delta u(k_i + N_c - 1) \end{bmatrix}, \; Z_i \triangleq \begin{bmatrix} z(k_i + 1 \mid k_i) \\ z(k_i + 2 \mid k_i) \\ \vdots \\ z(k_i + N_p \mid k_i) \end{bmatrix} \end{aligned} \tag{4.4.15}$$

where k_i is the current sampling instant, $z(k_i)$ is the state vector in (4.4.9) measured at k_i, N_c is the control horizon, N_p is the prediction horizon, and $z(k_i + m \mid k_i)$ is the predicted state variable at $k_i + m$ with state measurements $z(k_i)$.

[5] A detailed discussion of MPC design for discrete-time systems can be found in Chapters 1-3 in [100].

[6] The augmented state-space model is controllable; this was verified using Theorem 1.2 in [100].

We now construct the following N-step receding horizon optimal control problem:

$$\text{minimize } J = \sum_{i=1}^{N} \left[Z_i^T Z_i + \Delta U_i^T \Delta U_i \right] \tag{4.4.16}$$

subject to

$$\begin{aligned} & z(k_i+1) = \mathscr{A}\, z(k_i) + \mathscr{B}\, \widetilde{u}_2(k_i) \\ & \widetilde{u}_2(k_i) > \bar{a} + \bar{b} \mid \widetilde{\omega}(1) \mid, \qquad i = 1 \\ & \widetilde{u}_2(k_i) > \bar{a}, \qquad i = 2,3\cdots,N \end{aligned} \tag{4.4.17}$$

In every sampling period, the optimization problem determines the best control parameter ΔU_i that attempts to converge the sequence of states in Z_i to zero. Although ΔU_i contains N_c number of future control inputs, only the first entry is implemented as the actual control input. This optimization process is repeated using a more recent measurement of the states. It should be emphasized that the input constraint in (4.4.17), namely, $\widetilde{u}_2(k_i) > \bar{a} + \bar{b} \mid \widetilde{\omega}(1) \mid$ is imposed only in the first optimization window. In subsequent optimization windows, the constraint is relaxed to $\widetilde{u}_2(k_i) > \bar{a}$. This is necessary for $\widetilde{u}_2$ to converge to zero since $\bar{a}$ is negative - see (4.4.12), whereas $\bar{a} + \bar{b} \mid \widetilde{\omega}(1) \mid$ can assume positive values based on the initial value of $\widetilde{\omega}$.

Remark 1. *The control input $\widetilde{u}_2(k)$ is obtained as the numerical solution of the optimal control problem in (4.4.16) and (4.4.17). These inputs are applied at discrete time instants and the optimization solver is required to compute these inputs within the sampling time interval, which is equal to the time of flight δ^*. Since δ^* is relatively large, there is sufficient time for the optimization solver to generate the solution. This, along with the fact that the input constraint can be explicitly considered in the problem formulation, makes MPC well-suited for this problem.*

4.5 Simulation Results

4.5.1 System Parameters and Initial Conditions

We present simulation results of both LQR- and MPC-based control designs. The physical parameters of the devil-stick are provided below in SI units:

$$m = 0.1, \quad \ell = 0.5, \quad J = 0.0021 \tag{4.5.1}$$

Using these physical parameters and by choosing the values of $\theta^* = \pi/6$ rad and $\delta^* = 0.5$ sec, the steady-state values of state variables and control inputs are obtained from (4.4.3) as

$$\begin{aligned} \omega^* &= -4.18\,rad/s \quad h_x^* = 0.353\,m \quad v_x^* = 1.414\,m/s \\ v_y^* &= -2.45\,m/s \quad I^* = 0.565\,Ns \quad r^* = 0.030\,m \end{aligned} \tag{4.5.2}$$

Since h_y^* can be chosen arbitrarily, we chose

$$h_y^* = 3.0\,m \tag{4.5.3}$$

At the initial time, we assume $\theta = \theta^* = \pi/6$ rad and the states variables (in SI units) are

$$\omega(0) = 0, \quad h_x(0) = 0.53, \quad v_x(0) = 2.0, \quad h_y(0) = 1.0, \quad v_y(0) = -2.0 \tag{4.5.4}$$

For the physical parameters in (4.5.1), steady-state values of the states in (4.5.2) and (4.5.3), and initial conditions in (4.5.4), the control $\widetilde{u}_1(k)$ was chosen according to (4.4.8). The control input $\widetilde{u}_2(k)$ was designed using LQR and MPC methods and simulation results are presented next.

4.5.2 Results for the LQR-based Design

For the LQR design, the weight matrix Q for the states was chosen to be the identity matrix and the control weight R was chosen as 0.2. The control was obtained as

$$\widetilde{u}_2(k) = Fz(k), \quad F = \begin{bmatrix} -0.43 & -0.77 & 0.43 & 0.66 \end{bmatrix}$$

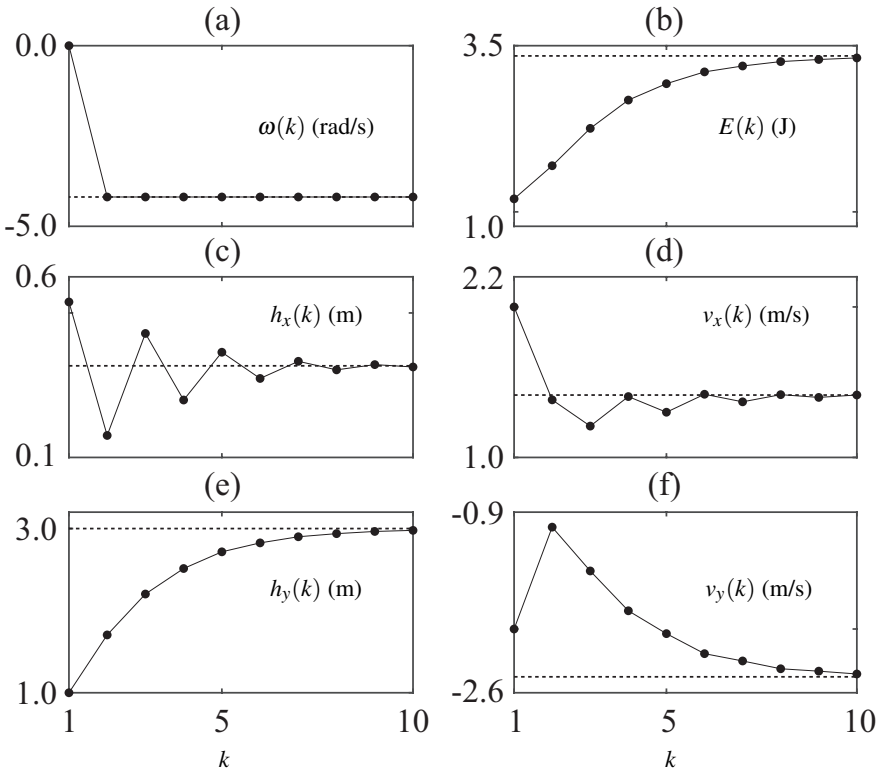

Figure 4.4: State variables and total energy E of the devil-stick at sampling instants k, $k = 1, 2, \cdots, 10$, for the LQR design.

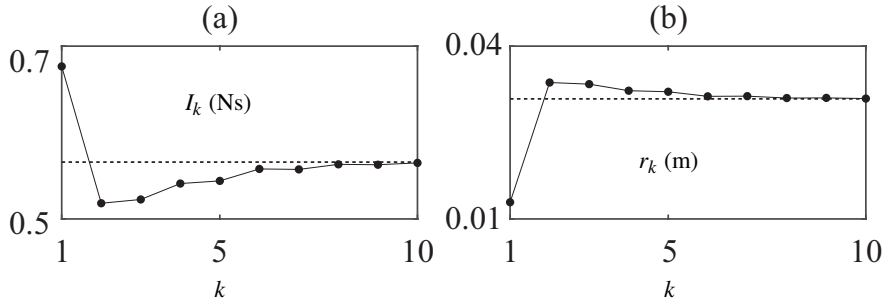

Figure 4.5: Control inputs for the devil-stick at sampling instants k, $k = 1, 2, \cdots, 10$, for the LQR design.

The simulation results are shown in Figs. 4.4[7] and 4.5. It can be seen from Fig. 4.4 (a) that the dead-beat control $\widetilde{u}_1(k)$ converges $\omega(k)$ to ω^* in one sampling interval. The control $\widetilde{u}_2(k)$ converges the remaining states to their steady-state values given in (4.5.2) in approximately $k = 10$ steps - see Figs. 4.4 (c)-(f). The control inputs I_k and r_k are shown in Figs. 4.5 (a) and (b). It can

[7]It should be noted that the state variables are shown in the reference frame of the right-handed juggler.

be seen that both control inputs converge to their steady-state values defined in (4.5.2); also the control input r_k remains well inside the constraint boundary $|r_k| < \ell/2$. The convergence of both the states and control inputs to their desired values imply that the devil-stick is juggled between two symmetric configurations. Since the magnitudes of v_x, v_y, ω_x, and h_y are the same in the two symmetric configurations, the total energy E (kinetic plus potential) reaches a constant value at steady state - see Fig. 4.4(b).

Remark 2. *The total energy of the devil-stick is the same at the symmetric configurations. Also, it is conserved during the flight phase. Therefore, in steady-state, the control inputs I^* and r^* do zero work on the system.*

4.5.3 Results for the MPC-based Design

The control horizon, prediction horizon, and the number of steps were taken as

$$N_c = 5, \quad N_p = 10, \quad N = 15$$

The MPC problem, defined by (4.4.16) and (4.4.17) were solved using quadratic programming in Matlab[8]. The state variables $h_x(k)$, $h_y(k)$, $v_x(k)$ and $v_y(k)$ and the control inputs I_k and r_k are shown in Fig. 4.6. The state variable $\omega(k)$ is not shown as it converged to its desired value in one sampling interval by the dead-beat controller. Similar to the LQR design, the control input r_k remains well inside the constraint boundary. The trajectory of the center-of-mass of the devil stick is shown in Fig. 4.7 (a); it starts from the initial configuration $(h_x, h_y) = (0.53, 1.00)$ and is eventually juggled between the symmetric coordinates $(h_x^*, h_y^*) = (0.353, 3.00)$ and $(-h_x^*, h_y^*) = (-0.353, 3.00)$ in steady state. Typically, N is chosen to be large to guarantee convergence. For our system, the states rapidly converged to zero with $N = 15$. In Fig. 4.7 (b), the devil-stick is shown at the two symmetric configurations where $\theta^* = \pi/6$ and several intermediate configurations that are equal time intervals apart.

[8]The quadprog Matlab function was used.

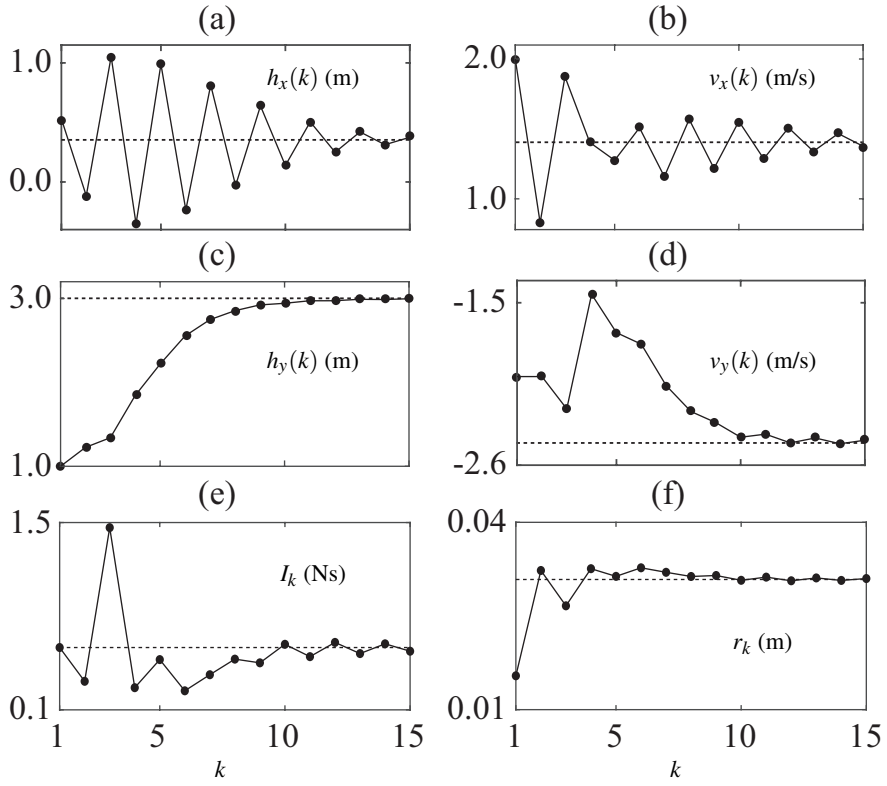

Figure 4.6: State variables and control inputs of the devil-stick at sampling instants k, $k = 1, 2, \cdots, 15$, for the MPC design.

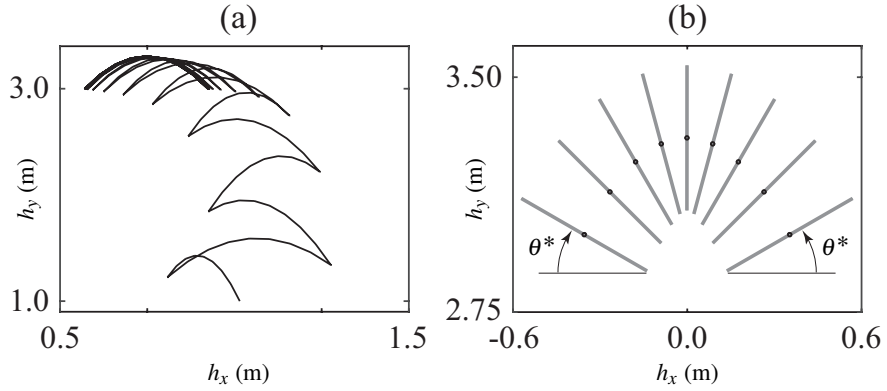

Figure 4.7: (a) Trajectory of the center-of-mass from the initial configuration to steady-state and (b) symmetric configurations and seven intermediate configurations of the devil-stick in steady state for the MPC design.

Remark 3. *In both simulations, the stick rotates by an angle* $(\pi - 2\theta^*)$ *between two consecutive control inputs. This corresponds to "top-only idle" juggling [47]. The controller is quite general and the stick can be controlled to rotate by* $(q\pi - 2\theta^*)$, $q = 2, 3, \cdots$, *by simply changing the*

definition of $\Delta\theta$ *in (4.3.13) from* $\Delta\theta = (\pi - 2\theta^*)$ *to* $\Delta\theta = (q\pi - 2\theta^*)$. *In other words, the stick can be made to flip multiple times in the flight phase, if desired. The "flip-idle" in [47] corresponds to the case where* $q = 2$.

CHAPTER 5

ENERGY-BASED ORBITAL STABILIZATION USING CONTINUOUS INPUTS AND IMPULSIVE BRAKING

5.1 Introduction

We present a controller for energy-based orbital stabilization of the class of Euler-Lagrange systems that have one passive revolute joint. Examples of systems in this class include the pendubot, acrobot, cart-pendulum system, rotary pendulum etc. The orbit is defined by fixed positions of the active coordinates and a desired energy of the overall system. The controller is comprised of continuous-time inputs and impulsive inputs for braking. At first, a general result for underactuated systems is presented which shows that an impulsive input causes an instantaneous jump in the mechanical energy of the system. This jump is shown to be explicitly dependent on the change in the active velocities due to an impulsive input. This result is then used to show that impulsive braking causes a negative jump in the mechanical energy of the system as well as the Lyapunov-like function. Finally, using a state-dependent impulsive dynamical system model [101], we present sufficient conditions for stabilization. To demonstrate the generality of our approach, we demonstrate orbital stabilization for the three-DOF Tiptoebot [6] through simulations. Experimental validation of the control design is carried out on a rotary pendulum to show the applicability of our approach in real hardware.

5.2 Problem Statement

Consider an n degree-of-freedom underactuated system with one passive degree-of-freedom. The generalized coordinates of the system are denoted by q, $q \triangleq \begin{bmatrix} q_1^T & q_2 \end{bmatrix}^T$, where $q_1 \in R^{n-1}$ and $q_2 \in R$ are the coordinates associated with the active and passive degrees-of-freedom. Our control objective is to stabilize the orbit defined by

$$(q_1, \dot{q}_1, E) = (0, 0, E_{des}) \tag{5.2.1}$$

where E is the total mechanical energy of the system and is given by the relation

$$E(q,\dot{q}) = \frac{1}{2}\dot{q}^T M(q)\,\dot{q} + \mathscr{F}(q) \tag{5.2.2}$$

and E_{des} is the desired value of E. In (5.2.2), $M(q) \in R^{n\times n}$ is the mass matrix, assumed to be positive definite, and $\mathscr{F}(q)$ is the potential energy, assumed to be a smooth function of q. The mass matrix is partitioned as

$$M(q) = \left[\begin{array}{c|c} M_{11}(q) & M_{12}(q) \\ \hline M_{12}^T(q) & M_{22}(q) \end{array}\right] \tag{5.2.3}$$

where $M_{11} \in R^{(n-1)\times(n-1)}$ and $M_{22} \in R$.

Assumption 1. *The mechanical energy of the system is assumed to be periodic in the passive coordinate q_2, such that $E(q_2 + 2\pi) = E(q_2)$.*

Remark 4. *Assumption 4 is easily satisfied if the passive degree-of-freedom is a revolute joint.*

Assumption 2. *The elements of the mass matrix $M(q)$ are bounded and the potential energy $\mathscr{F}(q)$ is lower bounded. Furthermore, if $q_1 = q_1^*$ is constant, then*

$$\frac{d}{dq_2}\left[kP_1(q_1^*, q_2) + P_2(q_1^*, q_2)\right] \neq 0$$

where k is any scalar constant, and

$$P_1(q_1^*, q_2) = \frac{2}{M_{22}}\left(\left[\frac{\partial M_{12}}{\partial q_2}\right] - \frac{1}{2}\left[\frac{\partial M_{22}}{\partial q_1}\right]^T - \frac{M_{12}}{2M_{22}}\left[\frac{\partial M_{22}}{\partial q_2}\right]\right)$$

$$P_2(q_1^*, q_2) = -P_1(q_1^*, q_2)\mathscr{F} - \frac{M_{12}}{M_{22}}\frac{\partial \mathscr{F}}{\partial q_2} + \left[\frac{\partial \mathscr{F}}{\partial q_1}\right]^T$$

Remark 5. *The boundedness property of $M(q)$ and $\mathscr{F}(q)$ is satisfied for systems that have no prismatic joints. For a given underactuated system with one passive DOF, assumption 5 can be easily verified.*

5.3 Modeling of System Dynamics

5.3.1 Lagrangian Dynamics

For our system described in section 5.2, the equations of motion can be written as:

$$\begin{aligned} \frac{d}{dt}\left(\frac{\partial \mathscr{L}}{\partial \dot{q}_1}\right) - \left(\frac{\partial \mathscr{L}}{\partial q_1}\right) &= u \\ \frac{d}{dt}\left(\frac{\partial \mathscr{L}}{\partial \dot{q}_2}\right) - \left(\frac{\partial \mathscr{L}}{\partial q_2}\right) &= 0 \end{aligned} \tag{5.3.1}$$

where $\mathscr{L}(q,\dot{q})$ is the Lagrangian and $u \in R^{n-1}$ is the vector of independent control inputs. Each element of the vector u is a continuous function of time for all $t \geqslant 0$ except at discrete instants $t = \tau_k$, $k = 1,2,\cdots$, where it is impulsive in nature. At $t = \tau_k$, the impulsive input vector has the form $u(\tau_k) = \mathscr{I}_k\,\delta(t-\tau_k)$, where $\delta(t-\tau_k)$ is the Dirac measure at time τ_k and $\mathscr{I}_k \in R^{n-1}$ is the impulse of the impulsive input. The Lagrangian has the form

$$\mathscr{L}(q,\dot{q}) = \frac{1}{2}\dot{q}^T M(q)\,\dot{q} - \mathscr{F}(q) \tag{5.3.2}$$

By substituting (5.2.3) in (5.3.2), the Lagrangian is written as

$$\mathscr{L}(q,\dot{q}) = \frac{1}{2}\dot{q}_1^T M_{11}\dot{q}_1 + \frac{1}{2}M_{22}\dot{q}_2^2 + \dot{q}_1^T M_{12}\dot{q}_2 - \mathscr{F} \tag{5.3.3}$$

and by substituting (5.3.3) in (5.3.1), the equations of motion are written in the form:

$$M_{11}\,\ddot{q}_1 + M_{12}\,\ddot{q}_2 + h_1(q,\dot{q}) = u \tag{5.3.4a}$$

$$M_{12}^T\,\ddot{q}_1 + M_{22}\,\ddot{q}_2 + h_2(q,\dot{q}) = 0 \tag{5.3.4b}$$

where

$$h_1 = \dot{M}_{11}\,\dot{q}_1 + \dot{M}_{12}\,\dot{q}_2 - \frac{1}{2}\left[\frac{\partial}{\partial q_1}(M_{11}\,\dot{q}_1)\right]\dot{q}_1 - \left[\frac{\partial (M_{12}\,\dot{q}_2)}{\partial q_1}\right]\dot{q}_1 - \frac{1}{2}\left[\frac{\partial M_{22}}{\partial q_1}\right]^T \dot{q}_2^2 + \left[\frac{\partial \mathscr{F}}{\partial q_1}\right]^T \tag{5.3.5a}$$

$$h_2 = \dot{M}_{22}\,\dot{q}_2 + \dot{q}_1^T\dot{M}_{12} - \frac{1}{2}\dot{q}_1^T\left[\frac{\partial (M_{11}\,\dot{q}_1)}{\partial q_2}\right] - \frac{1}{2}\left[\frac{\partial M_{22}}{\partial q_2}\right]\dot{q}_2^2 - \dot{q}_1^T\left[\frac{\partial (M_{12}\dot{q}_2)}{\partial q_1}\right] + \frac{\partial \mathscr{F}}{\partial q_2} \tag{5.3.5b}$$

Equations (5.3.4a) and (5.3.4b) can be rewritten in the form

$$\ddot{q}_1 = A(q,\dot{q}) + B(q)u \tag{5.3.6a}$$

$$\ddot{q}_2 = -(1/M_{22})\left[M_{12}^T\{A(q,\dot{q}) + B(q)u\} + h_2\right] \tag{5.3.6b}$$

where

$$B(q) = \left[M_{11} - (1/M_{22})M_{12}M_{12}^T\right]^{-1} \tag{5.3.7}$$

$$A(q,\dot{q}) = (1/M_{22})B(q)\left[M_{12}h_2 - h_1 M_{22}\right] \tag{5.3.8}$$

Using the properties of the mass matrix $M(q)$ and the Schur complement theorem [102], it can be shown that $B(q)$ is well-defined, symmetric and positive-definite, *i.e.*, $B(q) = B^T(q) > 0$.

5.3.2 Effect of Impulsive Inputs

When the control input u in (5.3.4a) is impulsive, it causes discontinuous jumps in the velocities $(\dot{q}_1, \dot{q}_2)$, while the coordinates (q_1, q_2) remain unchanged. For the impulsive input at $t = \tau_k$, the jump in the velocities is computed by integrating (5.3.4) as follows [86]:

$$\begin{bmatrix} M_{11} & M_{12} \\ M_{12}^T & M_{22} \end{bmatrix} \begin{bmatrix} \Delta\dot{q}_1 \\ \Delta\dot{q}_2 \end{bmatrix} = \begin{bmatrix} \mathscr{I}_k \\ 0 \end{bmatrix}, \quad \mathscr{I}_k \triangleq \int_{t_k^-}^{t_k^+} u(t_k)\,dt$$

In the above equation, $\Delta\dot{q}_1$ and $\Delta\dot{q}_2$ are defined as

$$\Delta\dot{q}_1 \triangleq (\dot{q}_1^+ - \dot{q}_1^-), \qquad \Delta\dot{q}_2 \triangleq (\dot{q}_2^+ - \dot{q}_2^-)$$

where $\dot{q}^- \triangleq \dot{q}(\tau_k^-)$ and $\dot{q}^+ \triangleq \dot{q}(\tau_k^+)$ denote the generalized velocities immediately before and after application of the impulsive inputs. Since the system is underactuated, the jump in $\dot{q}_2$ is dependent on the jumps in $\dot{q}_1$; this dependence is described by the one-dimensional impulse manifold [23] or impulse line, obtained from the equation above:

$$\dot{q}_2^+ = \dot{q}_2^- - (1/M_{22})M_{12}^T(\dot{q}_1^+ - \dot{q}_1^-) \tag{5.3.9}$$

The kinetic energy undergoes an instantaneous change due to jumps in the generalized velocities. This change is also equal to the change in the total mechanical energy of the system since the potential energy is only a function of the generalized coordinates. A formal statement of this result is provided next.

Lemma 1. *For the dynamical system in (5.3.4), the jump in the total mechanical energy due to application of an impulsive input is given by*

$$\Delta E \triangleq (E^+ - E^-) = \frac{1}{2}\dot{q}_1^{+T} B^{-1}(q)\,\dot{q}_1^+ - \frac{1}{2}\dot{q}_1^{-T} B^{-1}(q)\,\dot{q}_1^- \tag{5.3.10}$$

where E^- and E^+ are the energies immediately before and after application of the impulsive input.

Proof: See section 5.7.1.

Remark 6. *The proof of Lemma 1 is provided for the general case where the number of active and passive degrees-of-freedom are $(n-m)$ and m, respectively. This general result indicates that the change in mechanical energy due to an impulsive input depends only on the velocities of the active degrees-of-freedom immediately before and after application of the input. The result is analogous to the passivity property for the continuous-time case [103], where the power input to the system is the inner product of the velocities of the active degrees-of-freedom and control inputs. It is important to note that results similar to Lemma 1 appeared earlier in [104].*

We define impulsive braking as the process of applying impulsive inputs that result in $\dot{q}_1^+ = 0$. It follows from Lemma 1 that impulsive braking results in a loss of mechanical energy, given by the expression

$$\Delta E = -\frac{1}{2}\dot{q}_1^{-T} B^{-1}(q)\,\dot{q}_1^- \tag{5.3.11}$$

The discontinuous jumps in the generalized velocities and kinetic energy of the system also occurs when mechanical systems experience forces due to impact. In this regard, results similar to the ones presented above can be found in [104–106].

We now state an important result related to impulsive braking.

Lemma 2. *Consider the scalar function*

$$V = \frac{1}{2}\left[q_1^T K_p q_1 + \dot{q}_1^T K_d \dot{q}_1 + K_e(E - E_{des})^2\right] \tag{5.3.12}$$

where K_p and K_d are diagonal positive definite constant matrices and K_e is a positive constant. Impulsive braking results in a discontinuous jump in the function given by

$$\Delta V \triangleq (V^+ - V^-) = -\frac{1}{2}\dot{q}_1^{-T}\left[\frac{1}{4}\left\{K_e \dot{q}_1^{-T} B^{-1}(q)\dot{q}_1^-\right\}B^{-1}(q) + K_d + K_e(E^+ - E_{des})B^{-1}(q)\right]\dot{q}_1^- \tag{5.3.13}$$

where V^- and V^+ are values of the function immediately before and after impulsive braking. Furthermore, if $\left[K_d + K_e(E^+ - E_{des})B^{-1}(q)\right]$ is positive definite, then $\Delta V \leqslant 0$, and $\Delta V = 0$ if and only if $\dot{q}_1^- = 0$.

Proof: See section 5.7.2.

5.3.3 Hybrid Dynamical Model

For orbital stabilization of our system in (5.3.4), we propose a control strategy comprised of continuous and impulsive inputs. The impulsive inputs will be used for impulsive braking of the active coordinates, *i.e.*, $\dot{q}_1^+ = 0$. As a result, the change in the velocities can be obtained using (5.3.9) as follows:

$$\begin{aligned}\Delta\dot{q}_1 &= 0 - \dot{q}_1^- = -\dot{q}_1^- \\ \Delta\dot{q}_2 &= \dot{q}_2^+ - \dot{q}_2^- = (1/M_{22})M_{12}^T\dot{q}_1^-\end{aligned} \tag{5.3.14}$$

In addition to the impulsive braking inputs, we will reset the passive coordinate q_2 periodically to confine it to the compact set $[-3\pi/2, \pi/2]$. To describe the dynamics of our system, we adopt the state-dependent impulsive dynamical model in [101, pg.20]:

$$\dot{x}(t) = f_c[x(t)], \quad x(0) = x_0, \qquad x(t) \notin \mathscr{Z} \tag{5.3.15a}$$

$$\Delta x(t) = f_d[x(t)], \qquad x(t) \in \mathscr{Z} \tag{5.3.15b}$$

where $\mathscr{Z}$ defines the set where the impulsive inputs are applied and/or periodic resetting occurs. For our system,

$$x(t) \triangleq [q_1^T \quad q_2 \quad \dot{q}_1^T \quad \dot{q}_2]^T \in \mathscr{D} \subseteq R^{2n}$$
$$\Delta x(t) \triangleq x(t^+) - x(t^-)$$

In the above expression, $\mathscr{D}$ is the open set where $q_2 \in (a,b)$, $a < -3\pi/2$, $b > \pi/2$, and $x(t^-)$, $x(t^+)$ are the values of the state variables immediately before and after application of impulsive inputs or coordinate resetting. Using (5.3.6), (5.3.9) and (5.3.14), it can be shown

$$f_c = \begin{bmatrix} \dot{q}_1 \\ \dot{q}_2 \\ A(q,\dot{q}) + B(q)u \\ -(1/M_{22})\left[M_{12}^T\{A(q,\dot{q}) + B(q)u\} + h_2\right] \end{bmatrix} \tag{5.3.16}$$

$$f_d = \begin{cases} \begin{bmatrix} 0 & 0 & -\dot{q}_1^- & (1/M_{22})M_{12}^T\dot{q}_1^- \end{bmatrix}^T & : x(t) \in \mathscr{Z}_1 \\ \begin{bmatrix} 0 & 2\pi & 0 & 0 \end{bmatrix}^T & : x(t) \in \mathscr{Z}_2 \\ \begin{bmatrix} 0 & -2\pi & 0 & 0 \end{bmatrix}^T & : x(t) \in \mathscr{Z}_3 \end{cases} \tag{5.3.17}$$

$\mathscr{Z} = \mathscr{Z}_1 \cup \mathscr{Z}_2 \cup \mathscr{Z}_3$, $\mathscr{Z}_1$ is the set where impulsive braking inputs are applied (to be defined in Theorem 2 where the control design will be presented), and $\mathscr{Z}_2 \triangleq \{q_2 = -3\pi/2, \dot{q}_2 < 0\}$ and $\mathscr{Z}_3 \triangleq \{q_2 = \pi/2, \dot{q}_2 > 0\}$ are the sets where coordinate resetting occurs.

Note that the solution $x(t)$ of (5.3.15) is left-continuous, *i.e.*, it is continuous everywhere except at time instants t_k, $k = 1,2,\cdots$, where t_k's denote the time instants when impulsive inputs are applied or coordinate resetting occurs. Since impulsive inputs are applied at τ_k, $k = 1,2,\cdots$, $\{\tau_1,\tau_2,\cdots\} \subset \{t_1,t_2,\cdots\}$. Thus, $x(t^+)$ and $x(t^-)$, in the equation after (5.3.15), were defined

without the time stamp, *i.e.*

$$x(t^-) \triangleq x(t_k^-) = \lim_{\varepsilon \to 0^+} x(t_k - \varepsilon)$$
$$x(t^+) \triangleq x(t_k^-) + f_d[x(t_k^-)] = \lim_{\varepsilon \to 0^+} x(t_k + \varepsilon)$$

The well-posedness of the t_k's and the quasi-continuous dependence of the solution to (5.3.15) with respect to initial conditions [101, 104, 107] will be established later in the proof of Theorem 4 where $\mathscr{Z}_1$ will be defined.

5.4 Hybrid Control Design

5.4.1 Main Result

For the control objective in (5.2.1), we propose a hybrid control strategy comprised of a continuous controller and impulsive braking[1]. Theorem 4 provides the design of the continuous controller and defines the set $\mathscr{Z}_1$, where impulsive braking is applied. The proof of Theorem 2 is based on a Lyapunov-like function. The continuous controller is invoked as long as the derivative of the Lyapunov-like function is negative semi-definite; when this condition is not satisfied, impulsive braking is applied to produce negative jumps in the Lyapunov-like function. Before stating Theorem 4, we present Lemma 3 and an invariant set theorem [101, pg.38] that will be used in the proof of Theorem 4.

Lemma 3. *For the system in (5.3.4) subjected to continuous control, q_2 is constant if $\dot{q}_1$ and $\dot{u}$ are identically zero.*

Proof: See section 5.7.3.

Remark 7. *Lemma 3 implies that the active and passive generalized coordinates are dynamically coupled. Due to this coupling, the active generalized coordinates cannot be held stationary by*

[1] It is assumed that the active degrees-of-freedom will have a friction brake such that they can be stopped instantaneously.

constant generalized forces when the passive generalized coordinate is non-stationary. The proof of Lemma 3 is based on assumption 5, which is satisfied when dynamical coupling exists. The existence of such coupling has been verified for an inverted pendulum on a cart [74], pendubot, acrobot, and reaction-wheel pendulum; in this work it is shown for the tiptoebot and the rotary pendulum.

Theorem 3. *[101, pg.38] Consider the impulsive dynamical system given by (5.3.15), assume that $\mathscr{D}_c \subset \mathscr{D}$ is a compact positively invariant set with respect (5.3.15), and assume that there exists a continuously differentiable function $W : \mathscr{D} \to R$ such that*

$$[\partial W(x)/\partial x]\, f_c(x) \leqslant 0, \qquad x \in \mathscr{D}_c, \quad x \notin \mathscr{Z} \tag{5.4.1a}$$

$$W(x + f_d(x)) \qquad \leqslant W(x), \quad x \in \mathscr{D}_c, \quad x \in \mathscr{Z} \tag{5.4.1b}$$

Let $\mathscr{R} \triangleq \{x \in \mathscr{D}_c : x \notin \mathscr{Z}, [\partial W(x)/\partial x]\, f_c(x) = 0\} \cup \{x \in \mathscr{D}_c : x \in \mathscr{Z}, W(x + f_d(x)) = W(x)\}$ and let $\mathscr{M}$ denote the largest invariant set contained in $\mathscr{R}$. If $x_0 \in \mathscr{D}_c$, then $x(t) \to \mathscr{M}$ as $t \to \infty$.

Remark 8. *Although the invariance principle in [101] will be used (Theorem 3), the reader should be aware of the invariance principles in [55, 106, 108] that can be used for analysis of non-smooth and hybrid systems.*

Theorem 4. *For the impulsive dynamical system defined by (5.3.15), (5.3.16) and (5.3.17), and $x_0 \in \mathscr{D}$ such that*

$$-3\pi/2 < q_2(0) < \pi/2 \tag{5.4.2}$$

the following choice of control design:

$$u = -\left[(K_d + K_c)\, B(q) + K_e\,(E - E_{des})\, I\right]^{-1} \left[K_p\, q_1 + (K_d + K_c) A(q, \dot{q})\right] \tag{5.4.3a}$$

$$\mathscr{Z}_1 = \{x(t) \mid [A(q, \dot{q}) + B(q)u]^T\, K_c\, \dot{q}_1 \leqslant 0, \dot{q}_1 \neq 0\} \tag{5.4.3b}$$

where I is the identity matrix and K_c is a diagonal positive-definite matrix, guarantees asymptotic stability of the orbit in (5.2.1) if the gain matrices K_p, K_d and K_e satisfy the following conditions:

(i) $\left[K_d + K_e(E - E_{des})B^{-1}(q)\right]$ *is positive definite for all* q *and* $\dot{q}$,

(ii) If q_1^* *and* q_2^* *are constant values of* q_1 *and* q_2, *then the following system of equations:*

$$\left[\frac{\partial \mathscr{F}}{\partial q_1}\right]^T_{q=q^*} = -\frac{K_p\, q_1^*}{K_e\left[\mathscr{F}(q^*) - E_{des}\right]}$$
$$\left[\frac{\partial \mathscr{F}}{\partial q_2}\right]_{q=q^*} = 0$$

yields a finite number of solutions with $q_1^* = 0$, *and*

(iii) For all possible solutions of q_2^* *obtained from (ii) and for the function* V *in (5.3.12), the following inequality is satisfied*

$$V(t=0) < \min\{V \mid q_1 = 0, \dot{q}_1 = 0, E \in S_E \backslash \{E_{des}\}\}$$

where S_E *is the set of values of* E *evaluated at* $q_1 = 0$, $q_2 = q_2^*$, $\dot{q} = 0$.

Proof:

Consider the Lyapunov-like function V defined in (5.3.12); V is zero on the orbit defined in (5.2.1) and positive everywhere else. The time derivative of V is

$$\begin{aligned} \dot{V} &= q_1^T K_p\, \dot{q}_1 + \ddot{q}_1^T K_d\, \dot{q}_1 + K_e(E - E_{des})\dot{E} \\ &= \left[q_1^T K_p + \ddot{q}_1^T K_d + K_e(E - E_{des})\, u^T\right] \dot{q}_1 \end{aligned} \tag{5.4.4}$$

where $\dot{E} = u^T\, \dot{q}_1$ follows from the passivity property of underactuated Euler-Lagrange systems - see [103][2] and proposition 2.5 of [109]. By substituting $\ddot{q}_1$ from (5.3.6a) in (5.4.4) and using the symmetry of $B(q)$, we get

$$\dot{V} = \left[q_1^T K_p + A^T K_d + u^T B\left\{K_d + K_e(E - E_{des})B^{-1}\right\}\right] \dot{q}_1 \tag{5.4.5}$$

The following choice of u

$$u^T = -\left[q_1^T K_p + A^T K_d + \ddot{q}_1^T K_c\right]\left[B\left\{K_d + K_e(E - E_{des})B^{-1}\right\}\right]^{-1}, \tag{5.4.6}$$

[2]The proof of the passivity property follows from the fact that the matrix $[\dot{M} - 2C]$ is skew-symmetric for our choice of generalized coordinates.

which is well defined based on condition (i), results in

$$\dot{V} = -\ddot{q}_1^T K_c \dot{q}_1 \tag{5.4.7}$$

Substitution of (5.3.6a) in (5.4.6) followed by algebraic manipulation gives the expression for u in (5.4.3a). Substitution of (5.3.6a) in (5.4.7) gives

$$\dot{V} = -\left[A(q,\dot{q}) + B(q)u\right]^T K_c \dot{q}_1 \tag{5.4.8}$$

Based on the expression of $\dot{V}$, three cases may arise:

case (a): if $\left[A + Bu\right]^T K_c \dot{q}_1 > 0$, then $\dot{V} < 0$,

case (b): if $\left[A + Bu\right]^T K_c \dot{q}_1 \leqslant 0$, $\dot{q}_1 \neq 0$, then $x \in \mathscr{Z}_1$ and impulsive braking is applied - see (5.4.3b). Since condition (i) is satisfied, Lemma 2 indicates that V undergoes a discontinuous change ΔV, where $\Delta V < 0$, and

case (c): if $\dot{q}_1 = 0$, then $\dot{V} = 0$.

For case (b), impulsive braking results in $\dot{q}_1 = 0$ at t^+ and the trajectories of the system leave $\mathscr{Z}_1$. If $\dot{q}_1 \equiv 0$ for all $t > t^+$, the trajectories of the system remain outside $\mathscr{Z}_1$ and $\dot{V} \equiv 0$. If $\dot{q}_1 \not\equiv 0$ for $t > t^+$, V decreases and the trajectories of the system move away from $\mathscr{Z}_1$ since (5.4.7) implies

$$\dot{V}(t^+) = 0, \quad \ddot{V}(t^+) = -\ddot{q}_1^T(t^+) K_c \ddot{q}_1(t^+) < 0$$
$$\Rightarrow \dot{V}(\tau) < 0, \ \tau \in (t^+, t^+ + \varepsilon)$$

for some $\varepsilon > 0$ since K_c is positive-definite and $\ddot{q}_1 \neq 0$. The trajectories may re-enter $\mathscr{Z}_1$, but not arbitrarily quickly. Hence Zeno phenomenon will not be observed; this is discussed in section 5.7.4. Case (c) implies that either $\dot{q}_1 \equiv 0 \Rightarrow \dot{V} \equiv 0$, or $\dot{q}_1 \not\equiv 0$ and V continues to decrease again; this follows from our discussion of the nature of trajectories after impulsive braking. Cases (a), (b) and (c) imply that for $t > 0$, $V(t) \leqslant V(0) \triangleq c$ and therefore the set

$$\mathscr{D}_c \triangleq \{V \leqslant c\} \cap \{-3\pi/2 \leqslant q_2 \leqslant \pi/2\}$$

is positively invariant.

Cases (a), (b) and (c) together satisfy the conditions in Theorem 3[3] with $\mathscr{D}_c$ defined above and $W(x) = V(x)$. Since (b) implies $\Delta V < 0$, $\{x \in \mathscr{D}_c : x \in \mathscr{Z}, \Delta V = 0\}$ is an empty set. Therefore, $x(t) \to \mathscr{M} \subset \mathscr{R} = \{x \in \mathscr{D}_c : x \notin \mathscr{Z}, \dot{V} = 0\}$ as $t \to \infty$. From case (c), $\dot{V} = 0$ implies $\dot{q}_1 = 0$ and thus $\mathscr{R} = \{x \in \mathscr{D}_c : \dot{q}_1 \equiv 0\}$. In $\mathscr{R}$, $\ddot{q}_1 = 0$. Substitution of $\ddot{q}_1 = 0$ in (5.3.6a) and (5.4.6) yields

$$u^T = -A^T B^{-1} \tag{5.4.9a}$$

$$u^T B K_d = -K_e(E - E_{des})u^T - q_1^T K_p - A^T K_d \tag{5.4.9b}$$

Substitution of (5.4.9a) into (5.4.9b) gives

$$u^T K_e (E - E_{des}) + q_1^T K_p = 0 \tag{5.4.10}$$

The definition of $\mathscr{R}$ in Theorem 3 implies V is constant in $\mathscr{R}$. Also, q_1 is constant and $\dot{q}_1 = 0$ in $\mathscr{R}$. Therefore, from the definition of V in (5.3.12), we can claim that E is constant in $\mathscr{R}$. Let q_1^* and E^* be the constant values of q_1 and E. We now discuss two cases that can arise:

case 1: If $E^* = E_{des}$, we have $q_1^* = 0$ from (5.4.10). This implies that $\mathscr{M}$ is the orbit in (5.2.1).

case 2: if $E^* \neq E_{des}$, we get from (5.4.10)

$$u \triangleq u^* = -\frac{K_p q_1^*}{K_e(E^* - E_{des})} \tag{5.4.11}$$

where u^* is the constant value of the continuous control in $\mathscr{R}$.

For case 2, both q_1 and u are constants. Therefore, based on Lemma 3, we claim $q_2 = q_2^*$ is a constant. It follows from (5.2.2) that $E^* = \mathscr{F}(q^*)$. Using (5.3.4) and (5.3.5), we can show that the trajectories in $\mathscr{R}$ satisfy

$$\left[\frac{\partial \mathscr{F}}{\partial q_1}\right]^T_{q=q^*} = u^*, \qquad \left[\frac{\partial \mathscr{F}}{\partial q_2}\right]_{q=q^*} = 0$$

[3]Before we can apply Theorem 3, we must ensure that the time instants t_k, $k = 1, 2, \cdots$, are well-posed and the hybrid dynamical system in (5.3.15) satisfies the quasi-continuous dependence property. The conditions for well-posedness and its proof appear in section 5.7.5. A sufficient condition for satisfying the quasi-continuous dependence property and its proof appear in section 5.7.6.

Substituting the expression for u^* from (5.4.11) in the above equation along with $E^* = \mathscr{F}(q^*)$, we can use condition (*ii*) to claim $q_1^* = 0$. Using (5.3.12) and cases (a) and (b), we can claim that as $t \to \infty$, $V \to V^*$, where

$$V^* = \frac{1}{2} K_e (E^* - E_{des})^2 \leqslant V(t=0)$$

where $E^* \in S_E$. Since $V^* \leqslant V(t=0)$, we can claim using condition (iii) that $E^* = E_{des}$, *i.e.*, $V^* = 0$. Thus the largest invariant set $\mathscr{M}$ is the orbit defined in (5.2.1). This concludes the proof. □

5.4.2 Choice of Controller Gains

It can be easily shown that condition (i) in Theorem 4 is satisfied if

$$(1/K_e)\lambda_{min}(K_d) > [E_{des} - min(\mathscr{F})]\,\lambda_{max}[B^{-1}(q)]$$

where $\lambda_{min}(K_d)$ and $\lambda_{max}[B^{-1}(q)]$ are the minimum and maximum eigenvalues of K_d and $[B^{-1}(q)]$. Assumption 5 implies $\lambda_{max}[B^{-1}(q)]$ and $min(\mathscr{F})$ exist and therefore K_d and K_e can always be chosen to satisfy condition (i).

For the choice of K_e satisfying condition (i), K_p has to be chosen to satisfy condition (ii). Although we do not prove that condition (ii) can be simultaneously satisfied for the general case, several combinations of gains (K_p, K_d, K_e) were found to exist for the inverted pendulum on a cart [74]. The authors have independently verified that condition (ii) can be easily satisfied for several other underactuated mechanical systems, namely, the pendubot, the acrobot, and the reaction-wheel pendulum. It is shown that conditions (i) and (ii) can be simultaneously satisfied for the three-DOF Tiptoebot and the rotary pendulum. These examples indicate that condition (ii) is not restrictive.

Once the controller gains K_p, K_d and K_e have been chosen to satisfy conditions (i) and (ii) in Theorem 4, condition (iii) imposes no additional restrictions on the gains but simply provides an estimate of the region of attraction of the orbit. Since K_c does not appear in conditions (i)-(iii), it can be chosen without restriction.

5.5 Illustrative Example - The Tiptoebot

We consider the tiptoebot example as presented in 2.3.1. Using the following definition for the joint angles

$$q_1^T = [\ \theta_2 \quad \theta_3\ ]^T, \quad q_2 = \theta_1 \tag{5.5.1}$$

the dynamics of the tiptoebot can be expressed in the form of (5.3.4); the components of mass matrix in (5.2.3) are

$$\begin{aligned} M_{11} &= \begin{bmatrix} \alpha_2+\alpha_3+2\alpha_5\cos\theta_3 & \alpha_3+\alpha_5\cos\theta_3 \\ \alpha_3+\alpha_5\cos\theta_3 & \alpha_3 \end{bmatrix} \\ M_{12} &= \begin{bmatrix} \alpha_2+\alpha_3+\alpha_4\cos\theta_2+2\alpha_5\cos\theta_3+\alpha_6\cos(\theta_2+\theta_3) \\ \alpha_3+\alpha_5\cos\theta_3+\alpha_6\cos(\theta_2+\theta_3) \end{bmatrix} \\ M_{22} &= \alpha_1+\alpha_2+\alpha_3+2\left[\alpha_4\cos\theta_2+\alpha_5\cos\theta_3+\alpha_6\cos(\theta_2+\theta_3)\right] \end{aligned} \tag{5.5.2}$$

where α_i, $i = 1,2,\cdots,6$, are lumped parameters, defined as follows:

$$\begin{aligned} &\alpha_1 \triangleq m_1(\ell_1^2+\ell_2^2+\ell_3^2), \quad \alpha_2 \triangleq (m_2+m_3)\ell_2^2, \quad \alpha_3 \triangleq m_3\ell_3^2, \\ &\alpha_4 \triangleq m_2\ell_1\ell_2+m_3\ell_1\ell_2 \qquad \alpha_5 \triangleq m_3\ell_2\ell_3, \qquad \alpha_6 \triangleq m_3\ell_1\ell_3 \end{aligned} \tag{5.5.3}$$

The sum of Coriolis, centrifugal and gravitational force terms, h_1 and h_2, can be obtained using (5.3.5), where $\mathscr{F}(q)$ has the expression

$$\begin{aligned} \mathscr{F} &= \beta_1\sin\theta_1+\beta_2\sin(\theta_1+\theta_2)+\beta_3\sin(\theta_1+\theta_2+\theta_3) \\ \beta_1 &\triangleq (m_1+m_2+m_3)\ell_1 g, \quad \beta_2 \triangleq (m_2+m_3)\ell_2 g, \quad \beta_3 \triangleq m_3\ell_3 g \end{aligned} \tag{5.5.4}$$

The control input is defined as $u = [\tau_2\ \tau_3]^T$. In the compact set $\theta_1 \in [-3\pi/2, \pi/2]$, as defined in section 5.3.3, the upright equilibrium configuration of the tiptoebot is defined by

$$\theta_1 = -3\pi/2 \ or\ \pi/2, \left[\begin{array}{ccccc} \theta_2 & \theta_3 & \dot\theta_1 & \dot\theta_2 & \dot\theta_3 \end{array}\right] = \left[\begin{array}{ccccc} 0 & 0 & 0 & 0 & 0 \end{array}\right]$$

is unstable, but can be stabilized, by a linear controller, for example. The stabilized equilibrium will typically have a finite region of attraction; therefore, to stabilize from an arbitrary initial

configurations, we first use the controller in section 5.3 to stabilize an orbit that intersects the region of attraction. The obvious choice for such an orbit is the one where E_{des} equals the potential energy of the system at the equilibrium. Substitution of $\theta_1 = -3\pi/2$ or $\pi/2$ and $\theta_2 = \theta_3 = 0$ in (5.5.4) yields $E_{des} = \beta_1 + \beta_2 + \beta_3$. The control objective in (5.2.1) can therefore be written as

$$\theta_2 = \theta_3 = 0,\ \dot{\theta}_2 = \dot{\theta}_3 = 0,\ E_{des} = (\beta_1 + \beta_2 + \beta_3) \tag{5.5.5}$$

The feasibility of our control design is discussed next.

5.5.1 Selection of Controller Gains

The initial configuration of the tiptoebot is taken as

$$[\ \theta_1 \quad \theta_2 \quad \theta_3 \quad \dot{\theta}_1 \quad \dot{\theta}_2 \quad \dot{\theta}_3\ ] = [\ 0 \quad \pi \quad \pi \quad 0 \quad 0 \quad 0\ ] \tag{5.5.6}$$

In this configuration, the tiptoebot is coiled up: the first link is horizontal, the second link folds back on the first link, and the third link folds back on the second link. The links were chosen to have the same mass $m_1 = m_2 = m_3 = 0.1$ kg and the same length $\ell_1 = \ell_2 = \ell_3 = 0.6$ m. For this choice of mass and length parameters, the lumped parameters of the tiptoebot, defined in (5.5.3) and (5.5.4), are provided in Table 6.1 below:

Table 5.1: Tiptoebot lumped parameters in SI units

α_1	0.108	α_4	0.072	β_1	1.764
α_2	0.072	α_5	0.036	β_2	1.176
α_3	0.036	α_6	0.036	β_3	0.588

The passive joint of the tiptoebot is revolute and therefore assumption 1 holds good. Assumption 2 also holds good - this is discussed in 5.7.7.

The following choice of gains satisfy condition (i) and (ii):

$$K_p = \begin{bmatrix} 70 & 0 \\ 0 & 70 \end{bmatrix}, \quad K_d = \begin{bmatrix} 2.8 & 0 \\ 0 & 2.8 \end{bmatrix}, \quad K_e = 2.2 \tag{5.5.7}$$

Condition (ii) results in $\theta_2^* = \theta_3^* = 0$, which upon substitution in (5.3.4b) and (5.3.5b) yields

$$\frac{\partial \mathscr{F}}{\partial q_2} = 0 \quad \Rightarrow \quad \cos\theta_1^* = 0 \tag{5.5.8}$$

From section 5.3.3 we know that q_2 lies in the compact set $[-3\pi/2, \pi/2]$. Thus θ_1 lies in the same compact set - see (5.5.1). In this set, the possible solutions of (5.5.8) are $\theta_1^* = \{-3\pi/2, -\pi/2, \pi/2\}$. For $\theta_1^* = -3\pi/2$ or $\pi/2$, and $\theta_2^* = \theta_3^* = 0$, we know that $E = E_{des}$. Therefore, to satisfy condition (iii), we use $\theta_1^* = -\pi/2$; this results in the following inequality

$$V(t=0) < 2K_e\left[E(q_1^* = 0, q_2^* = -\pi/2) - E_{des}\right]^2 = 2K_e(\beta_1 + \beta_2 + \beta_3)^2$$

For the initial configuration in (5.5.6), K_e in (5.5.7) satisfies the inequality above. The matrix K_c was chosen as

$$K_c = \begin{bmatrix} 1.2 & 0 \\ 0 & 1.2 \end{bmatrix} \tag{5.5.9}$$

5.5.2 Simulation Results

For the initial configuration in (5.5.6) and controller gains in (5.5.7) and (5.5.9), the simulation results are shown in Figs.5.1 and 5.2. The effect of impulsive braking can be seen in Figs.5.1 (d) and (f), where $\dot{\theta}_2$ and $\dot{\theta}_3$ (the velocities of the active joints) jump to zero on multiple occasions. Each impulsive braking also results in a negative jump in the mechanical energy (follows from Lemma 1) which can be seen in Fig.5.1 (b). Since impulsive inputs cause no jumps in the joint angles, there is no change in θ_1, θ_2 and θ_3 at the time of impulsive braking - see Figs.5.1 (a), (c) and (e). In Fig.5.1 (a), θ_1 never leaves the set $[-3\pi/2, \pi/2]$ and therefore virtual impulsive inputs are not applied.

While impulsive brakings cause negative jumps in the total energy E, the continuous-time controller in (5.4.3a) adds energy to the system; together, they converge the energy to the desired values E_{des} - see Fig.5.1 (b). The phase portrait of the passive joint is shown in Fig.5.2 (a). The jumps in the phase portrait (vertical drops in $\dot{\theta}_1$, twice) is due to impulsive braking. The variation

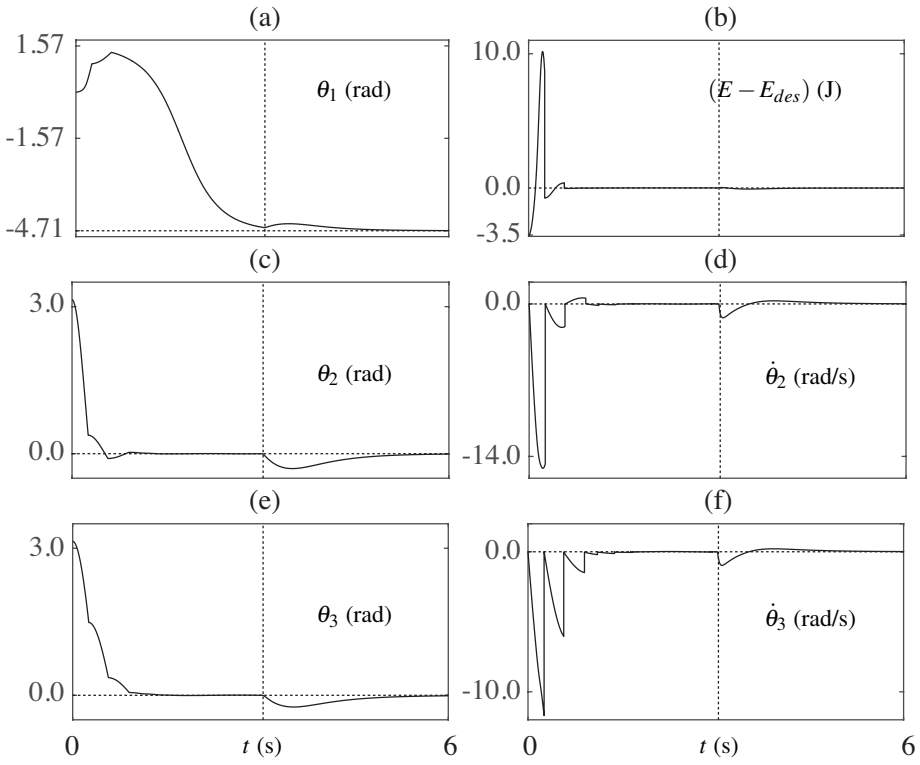

Figure 5.1: Plots of the joint angles θ_1, θ_2, θ_3, error in the desired energy $(E - E_{des})$, and the active joint velocities $\dot{\theta}_2$, $\dot{\theta}_3$ of the Tiptoebot.

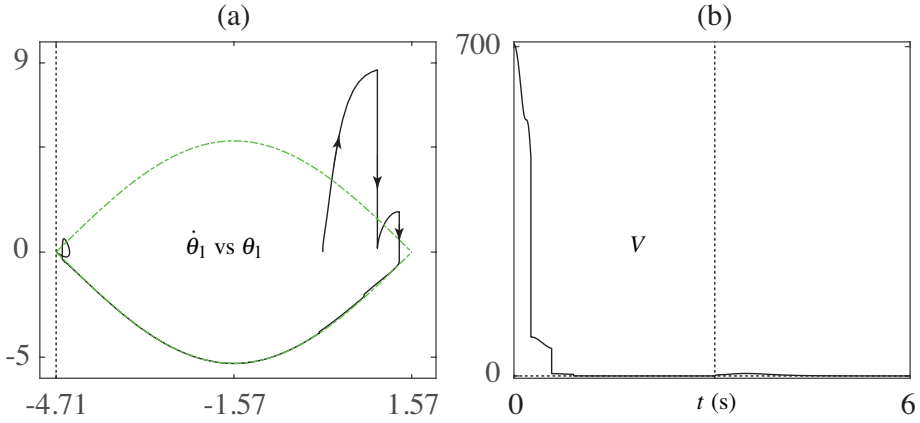

Figure 5.2: Plots showing (a) phase portrait of passive joint angle θ_1, and (b) variation of the Lyapunov-like function V. The desired orbit is shown using dashed green line in (a).

of the Lyapunov-like function V with time is shown in Fig.5.2 (b) - it can be seen that V decreases monotonically due to the action of the continuous-time controller and undergoes negative jumps intermittently due to impulsive brakings. The continuous controller and impulsive brakings work together to converge V to zero.

The gain matrices in (5.5.7) and (5.5.9) were chosen such that convergence to the desired orbit is fast. The simulation results indicate that the system trajectories reach a close neighborhood of the desired orbit very quickly, at approximately 3 s. For stabilization of the equilibrium in (5.5.6), a linear controller was designed using LQR. The matrices Q and R of the algebraic Ricatti equation were chosen to be $I_{6\times 6}$ and $2I_{2\times 2}$, where $I_{k\times k}$ is the identity matrix of size k. The linear controller was invoked when $V \leqslant 0.05$ and $\mid \theta_1 - \pi/2 \mid \leqslant 0.05$.

5.6 Experimental Validation

5.6.1 System Description

Experiments were done with a rotary pendulum. As shown in Fig.5.3, the system is comprised of a horizontal arm OA of mass m_a and length ℓ_a, which rotates about point O, and a pendulum of mass m_p and length ℓ_p, that rotates about point A. The center-of-mass of the horizontal arm is located at a distance d_a from O and the center-of-mass of the pendulum is located at a distance d_p from A. The horizontal arm is actively controlled by an external torque τ and its angular displacement about the z axis is denoted by ϕ. The pendulum is passive and its angular displacement about the ε_r axis is denoted by θ. The accleration due to gravity is denoted by g. With the following definition:

$$[q_1 \quad q_2]^T = [\phi \quad \theta]^T \tag{5.6.1}$$

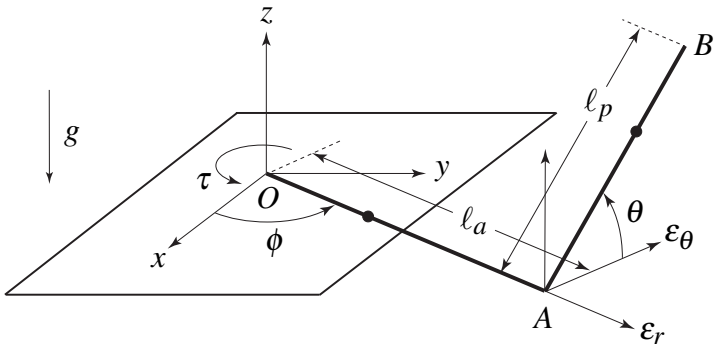

Figure 5.3: Schematic of a rotary pendulum.

the dynamics of the system can be expressed in the from given by (5.3.4), where $u = \tau$, and

$$\begin{aligned} M_{11} &= \gamma_1 + \gamma_2 \cos^2\theta, \quad M_{12} = \gamma_3 \sin\theta, \quad M_{22} = \gamma_2 \\ h_1 &= \gamma_3 \cos\theta\, \dot{\theta}^2 - \dot{\phi}\,\dot{\theta}\gamma_2 \sin 2\theta, \quad h_2 = \gamma_2 \dot{\phi}^2 \sin\theta \cos\theta + \gamma_4 \cos\theta \\ \gamma_1 &\triangleq m_a d_a^2 + m_p \ell_a^2, \quad \gamma_2 \triangleq m_p d_p^2, \quad \gamma_3 \triangleq -m_p \ell_a d_p, \quad \gamma_4 \triangleq m_p g d_p \end{aligned} \tag{5.6.2}$$

The physical parameters of the experimental setup are

$$\gamma_1 = 0.0120,\ \gamma_2 = 0.0042,\ \gamma_3 = -0.0038,\ \gamma_4 = 0.1190 \tag{5.6.3}$$

The control torque was applied by a 24-Volt permanent magnet brushed DC motor[4].The motor is driven by a power amplifier[5] operating in current mode. The motor torque constant is 37.7 mNm/A and the amplifier gain is 4.4 A/volt. An electromagnetic friction brake[6] was integrated to the shaft of the DC motor. In the OFF state, the brake engages a friction pad to the shaft of the motor which prevents the shaft from turning; in the ON state, the brake is disengaged and the motor shaft rotates freely. For impulsive braking, the brake was kept engaged till the active velocity $\dot{\phi}$ reached a close neighborhood of zero. The brake was powered ON/OFF by sending command voltage signals through an n-channel mosfet. The rotary pendulum was interfaced with a dSpace DS1104 board and the Matlab/Simulink environment was used for real-time data acquisition and control with a sampling rate of 1 Khz. The angular positions of the links were measured using incremental optical encoders; the angular velocities were obtained by differentiating and low-pass filtering the position signals.

5.6.2 Selection of Controller Gains

The total energy of the system is obtained from (5.2.2) as follows

[4]The motor manufacturer is Faulhaber Drive Systems. The motor has a gearbox with a reduction ratio of 3.71 : 1.

[5]The amplifier is a product of Advanced Motion Control.

[6]The electromagnetic brake is manufactured by Anaheim Automation, model BRK-20H-480-024. The brake can withhold torques up to 3.4 Nm.

$$E = \frac{1}{2}(\gamma_1 + \gamma_2 \cos^2\theta)\,\dot{\phi}^2 + \frac{1}{2}\gamma_2\,\dot{\theta}^2 + \gamma_3 \sin\theta\,\dot{\phi}\,\dot{\theta} + \mathscr{F}$$
$$\mathscr{F} = \gamma_4 \sin\theta \tag{5.6.4}$$

For the control objective in (5.2.1), we choose E_{des} to be equal to the energy associated with the homoclinic orbit that contains the upright equilibrium

$$\begin{bmatrix} \phi & \theta & \dot{\phi} & \dot{\theta} \end{bmatrix} = \begin{bmatrix} 0 & \pi/2 & 0 & 0 \end{bmatrix} \; or \; \begin{bmatrix} 0 & -3\pi/2 & 0 & 0 \end{bmatrix}$$

Using (5.6.4), the energy associated with the homoclinic orbit can be written as

$$E_{des} = \gamma_4 \tag{5.6.5}$$

The passive joint of the rotary pendulum is revolute and thus assumption 1 holds good. Assumption 5 also holds good - this is shown in 5.7.7. From (5.6.4) we know that $\mathscr{F}$ is only a function of θ and therefore condition (ii) is trivially satisfied resulting in the solution $\phi^* = 0$. In the compact set $[-3\pi/2, \pi/2]$, the possible solutions of θ^* obtained from condition (ii) are $\theta^* = \{-3\pi/2, -\pi/2, \pi/2\}$. At $\theta^* = \pi/2$ or $\theta^* = -3\pi/2$ and $\phi^* = 0$, $E = E_{des}$. Using condition (iii), we therefore get $\theta^* = -\pi/2$; this implies that K_e should be chosen to satisfy

$$V(t=0) < 2K_e\gamma_4^2 \tag{5.6.6}$$

At the lower equilibrium configuration where $[\phi\ \theta\ \dot{\phi}\ \dot{\theta}] = [0\ -\pi/2\ 0\ 0]$, we have $V = 2K_e\gamma_4^2$. This violates the inequality in (5.6.6). This implies that our controller cannot swing-up the pendulum when the system is exactly at the lower equilibrium.Therefore, in experiments, a small external perturbation was provided such that the system is not at the lower equilibrium at the initial time. For the experimental results presented herein, the initial configuration of the system after the perturbation was measured as

$$\begin{bmatrix} \phi(0) & \theta(0) & \dot{\phi}(0) & \dot{\theta}(0) \end{bmatrix}^T = \begin{bmatrix} 0.01 & -1.42 & 0.05 & 0 \end{bmatrix}^T \tag{5.6.7}$$

For the initial conditions in (5.6.7) and physical parameter values in (5.6.3), the following gains satisfied conditions (i)-(iii):

$$K_p = 0.5, \quad K_c = 0.08, \quad K_d = 0.3, \quad K_e = 100 \tag{5.6.8}$$

For the above set of gains, the experimental results are presented next.

5.6.3 Experimental Results

The experimental results are shown in Fig.5.4. The hybrid controller for orbital stabilization was active for the first 20 s. At the end of this period, the system trajectories reached a close neighborhood of the upright equilibrium $[\phi\ \theta\ \dot{\phi}\ \dot{\theta}] = [0\ -3\pi/2\ 0\ 0]$ and the following linear controller was invoked for stabilization:

$$\tau_s = 1.4\phi - 20.23(\theta + 3\pi/2) + 1.14\dot{\phi} - 1.98\dot{\theta}$$

The poles of the closed-loop system were located at $-37.0 \pm 20.0\,i$ and $-1.0 \pm 1.2\,i$.

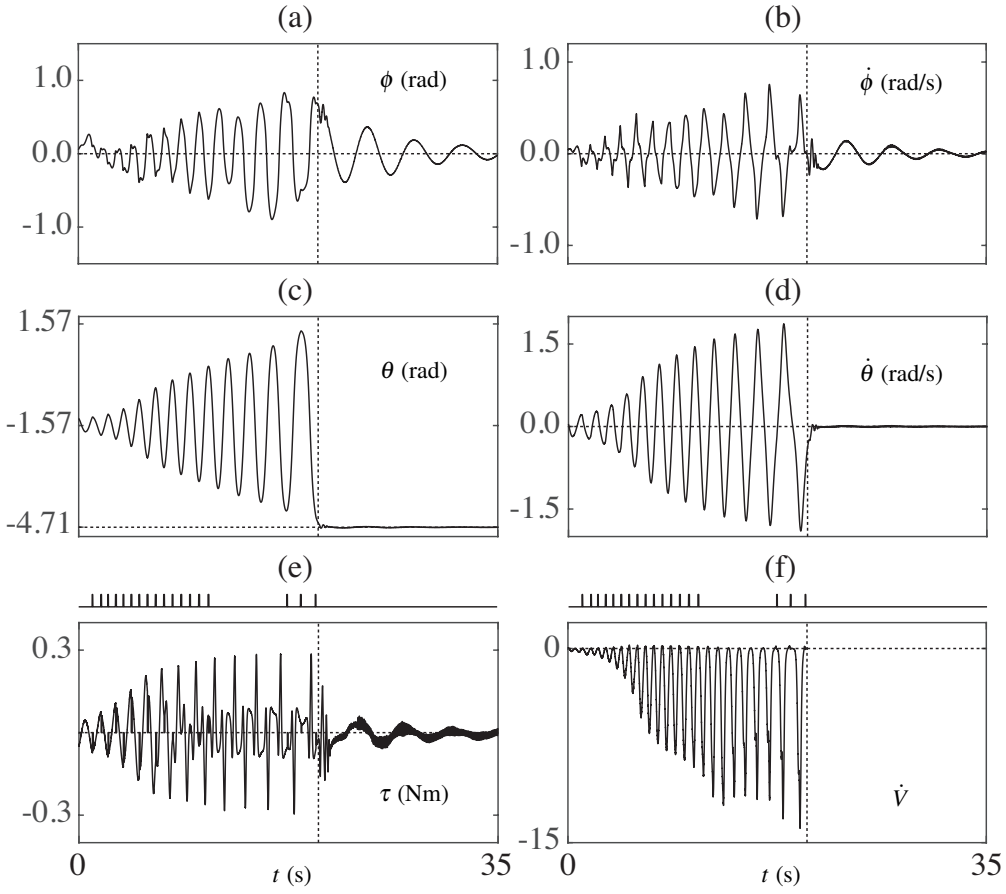

Figure 5.4: Rotary pendulum experimental results: (a)-(d) are plots of joint angles and joint velocities, (e) control torque, and (f) derivative of Lyapunov-like function. The brake pulses are shown within plots (e) and (f), the peaks represent time intervals when the brakes were engaged.

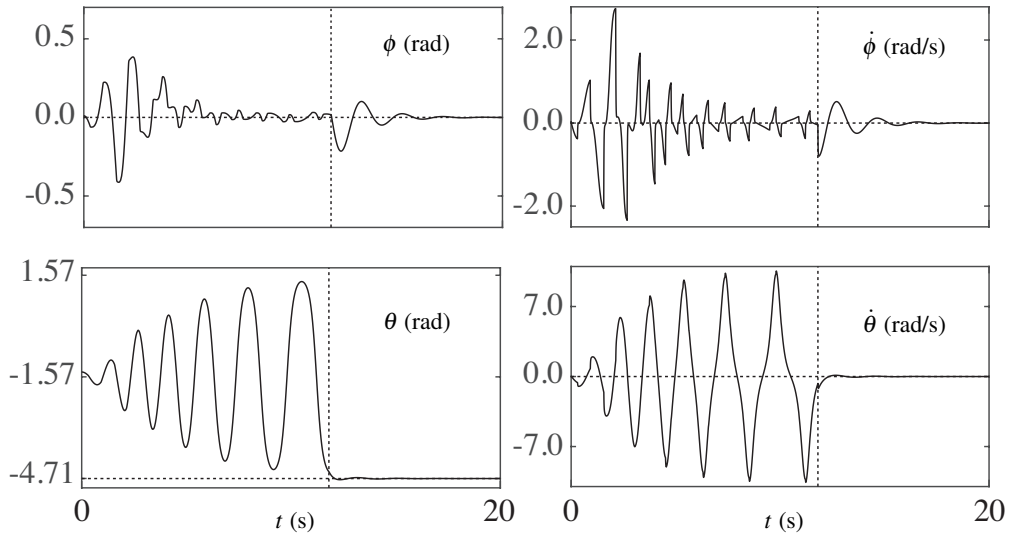

Figure 5.5: Rotary pendulum simulation results.

The pulses shown on the top of Figs.5.4 (e) and (f) correspond to the time intervals when the brake was engaged (OFF) during orbital stabilization. The brake was disengaged (ON) when the condition $|\dot{\phi}| \leqslant \mu$ was satisfied; the value of μ was chosen to be small, equal to 0.1 rad/s. The time intervals required for braking were very short (≈ 0.04 s, on average); this implies that the brakings were impulsive in nature. The effect of impulsive braking can be seen in Fig.5.4 (b) where $\dot{\phi}$ jumps to almost zero value upon engagement of the brake on multiple occasions.

It can be seen from Fig.5.4 (c) that the amplitude of the pendulum gradually increases and finally reaches a close neighborhood of the upright equilibrium configuration. The derivative of the Lyapunov-like function is shown in Fig.5.4 (f). It can be seen that $\dot{V}$ never becomes positive; this is because the brake is engaged every time when $\dot{V}$ is about to become positive[7]. Since $\dot{V}$ is always negative, V decreases monotonically and orbital stabilization is achieved. A plot of the motor torque is shown in Fig.5.4 (e). To minimize wear and tear of the brake, the commanded motor torque was set to zero when the brake was engaged. A video of this experiment can be found on the weblink: `www.egr.msu.edu/~mukherji/RotaryPendulum.mp4`

Simulation results for the same set of initial conditions and controller gains in (5.6.7) and (5.6.8) are presented in Fig.5.5. A comparison of Figs.5.4 and 5.5 indicate that the joint velocities

[7]When $|\dot{\phi}| \leqslant \mu \approx 0$, the brake is not engaged since $\dot{V} \approx 0$ - see (5.4.7).

in experiments are lower than those in simulations - this can be attributed to the presence of friction and other dissipative forces. The amplitude of the active joint ϕ is larger in experiments than simulations - this is due to the fact that the controller has to overcome the dissipative losses and additional energy is added through larger amplitude of motion. As expected, the time needed for stabilization is less in simulations than experiments.

Remark 9. *For comparison, we considered the rotary pendulum example in [71]. Taking identical initial conditions and physical parameters of the system therein, we simulated our controller with the gains*

$$K_p = 0.20, \quad K_d = 0.12, \quad K_e = 50, \quad K_c = 0.70$$

The gains were tuned such that the magnitude of the motor torque did not exceed 0.3 *Nm. The system trajectories converged to the desired orbit in approx.* 30 *s. The controller in [71] took approx.* 100 *sec and the magnitude of the maximum torque was* 8 *Nm. Our controller performed well, both in terms of motor torque requirement and speed of convergence. This better performance, however, comes at the cost of additional brake hardware.*

5.7 Proofs and Additional Discussions

5.7.1 Proof of Lemma 1

The proof of Lemma 1 is provided here for the general case where the underactuated system has m passive and $n-m$ active generalized coordinates, *i.e.* $q_1 \in R^{n-m}$, $q_2 \in R^m$ and $u \in R^{n-m}$. The Euler-Lagrange equation has the same form as in (5.3.4) with $M_{11} \in R^{(n-m)\times(n-m)}$, $M_{22} \in R^{m\times m}$, $h_1 \in R^{(n-m)}$, and $h_2 \in R^m$. The change in the total energy due to application of an impulsive input is equal to the change in the kinetic energy:

$$\begin{aligned}
\Delta E &= \frac{1}{2}\dot{q}^{+^T} M(q)\dot{q}^+ - \frac{1}{2}\dot{q}^{-^T} M(q)\dot{q}^- \\
&= \frac{1}{2}\left[\dot{q}_1^{+^T} M_{11}\,\dot{q}_1^+ - \dot{q}_1^{-^T} M_{11}\,\dot{q}_1^-\right] + \frac{1}{2}\left[\dot{q}_2^{+^T} M_{22}\,\dot{q}_2^+ - \dot{q}_2^{-^T} M_{22}\,\dot{q}_2^-\right] \\
&\quad + \dot{q}_1^{+^T} M_{12}\,\dot{q}_2^+ - \dot{q}_1^{-^T} M_{12}\,\dot{q}_2^- \qquad \text{(A.1)}
\end{aligned}$$

The impulse manifold, given in (5.3.9) for $m = 1$, is

$$\dot{q}_2^+ = \dot{q}_2^- - M_{22}^{-1} M_{12}^T (\dot{q}_1^+ - \dot{q}_1^-) \tag{A.2}$$

Substitution of $\dot{q}_2^+$ from (A.2) into (A.1) yields

$$\begin{aligned}\Delta E = &\frac{1}{2}\left[\dot{q}_1^{+T} M_{11}\, \dot{q}_1^+ - \dot{q}_1^{-T} M_{11}\, \dot{q}_1^-\right] + \frac{1}{2}\left[\dot{q}_2^- - M_{22}^{-1} M_{12}^T (\dot{q}_1^+ - \dot{q}_1^-)\right]^T M_{22} \left[\dot{q}_2^- - M_{22}^{-1} M_{12}^T (\dot{q}_1^+ - \dot{q}_1^-)\right] \\ &- \frac{1}{2}\dot{q}_2^{-T} M_{22}\, \dot{q}_2^- - \dot{q}_1^{-T} M_{12}\, \dot{q}_2^- + \dot{q}_1^{+T} M_{12} \left[\dot{q}_2^- - M_{22}^{-1} M_{12}^T (\dot{q}_1^+ - \dot{q}_1^-)\right]\end{aligned}$$

Expanding, canceling, and regrouping the terms on the right-hand side of the above equation yields

$$\Delta E = \frac{1}{2}\dot{q}_1^{+T}\left[M_{11} - M_{12} M_{22}^{-1} M_{12}^T\right]\dot{q}_1^+ - \frac{1}{2}\dot{q}_1^{-T}\left[M_{11} - M_{12} M_{22}^{-1} M_{12}^T\right]\dot{q}_1^- \tag{A.3}$$

Similar to (5.3.7), $B(q)$ is defined for the general case as follows

$$B(q) = \left[M_{11} - M_{12} M_{22}^{-1} M_{12}^T\right]^{-1} \tag{A.4}$$

From the properties of the mass matrix $M(q)$, it can be shown that $B(q)$ is well-defined; also, it is symmetric and positive-definite, *i.e.*, $B(q) = B^T(q) > 0$. Substitution of (A.4) into (A.3) gives (5.3.10). □

5.7.2 Proof of Lemma 2

Impulsive inputs result in no change in the generalized coordinates. Additionally, impulsive braking results in $\dot{q}_1^+ = 0$. Therefore, from the definition of V in (5.3.12), ΔV for impulsive braking can be expressed as

$$\begin{aligned}\Delta V &= \frac{1}{2}\left[K_e (E^+ - E_{des})^2 - K_e (E^- - E_{des})^2 - \dot{q}_1^{-T} K_d\, \dot{q}_1^-\right] \\ &= \frac{1}{2}\left[K_e (E^+ + E^- - 2E_{des})\Delta E - \dot{q}_1^{-T} K_d\, \dot{q}_1^-\right] \\ &= \frac{1}{2}\left[K_e (2E^+ - \Delta E - 2E_{des})\Delta E - \dot{q}_1^{-T} K_d\, \dot{q}_1^-\right]\end{aligned}$$

where ΔE is defined in (5.3.10). Substitution of ΔE from (5.3.11) in the equation above yields

$$\begin{aligned}
\Delta V &= -\frac{1}{2}\left[(\dot{q}_1^-{}^T B^{-1}\dot{q}_1^-)K_e\{E^+ - E_{des} + \frac{1}{4}\dot{q}_1^-{}^T B^{-1}\dot{q}_1^-\} + \dot{q}_1^-{}^T K_d\,\dot{q}_1^-\right] \\
&= -\frac{1}{2}\dot{q}_1^-{}^T\left[K_e\{E^+ - E_{des} + \frac{1}{4}\dot{q}_1^-{}^T B^{-1}\dot{q}_1^-\}B^{-1} + K_d\right]\dot{q}_1^- \\
&= -\frac{1}{2}\dot{q}_1^-{}^T\left[\frac{1}{4}\left\{K_e\,\dot{q}_1^-{}^T B^{-1}\,\dot{q}_1^-\right\}B^{-1} + K_d + K_e(E^+ - E_{des})B^{-1}\right]\dot{q}_1^-
\end{aligned}$$

which is the same as in (5.3.13). Since B, defined in (A.4), is positive-definite, $\{K_e\,\dot{q}_1^-{}^T B^{-1}\,\dot{q}_1^-\}B^{-1}$ is positive-definite. Therefore, if $\left[K_d + K_e(E^+ - E_{des})B^{-1}(q)\right]$ is positive-definite, $\Delta V \leqslant 0$ and $\Delta V = 0$ iff $\dot{q}_1^- = 0$. □

5.7.3 Proof of Lemma 3

Let q_1^* and u^* denote the constant values of q_1 and u, respectively. From the passivity property of underactuated Euler-Lagrange systems [103, 109], it follows that $\dot{E} = u^T\,\dot{q}_1 = 0$. Let E^* denote the constant value of E. Since $\dot{q}_1 \equiv 0$, using (5.3.4) and (5.3.5), we get the following

$$M_{12}\,\ddot{q}_2 + \left[\frac{\partial M_{12}}{\partial q_2}\right]\dot{q}_2^2 - \frac{1}{2}\left[\frac{\partial M_{22}}{\partial q_1}\right]^T\dot{q}_2^2 + \left[\frac{\partial \mathscr{F}}{\partial q_1}\right]^T = u^* \tag{A.5a}$$

$$M_{22}\,\ddot{q}_2 + \frac{1}{2}\left[\frac{\partial M_{22}}{\partial q_2}\right]\dot{q}_2^2 + \frac{\partial \mathscr{F}}{\partial q_2} = 0 \tag{A.5b}$$

Eliminating $\ddot{q}_2$ using (A.5a) and (A.5b), we get

$$\left(\left[\frac{\partial M_{12}}{\partial q_2}\right] - \frac{1}{2}\left[\frac{\partial M_{22}}{\partial q_1}\right]^T - \frac{M_{12}}{2M_{22}}\left[\frac{\partial M_{22}}{\partial q_2}\right]\right)\dot{q}_2^2 - \frac{M_{12}}{M_{22}}\frac{\partial \mathscr{F}}{\partial q_2} + \left[\frac{\partial \mathscr{F}}{\partial q_1}\right]^T = u^* \tag{A.6}$$

Since $E = E^*$ is constant and $\dot{q}_1 = 0$, (5.2.2) gives

$$\dot{q}_2^2 = \frac{2(E^* - \mathscr{F})}{M_{22}} \tag{A.7}$$

Substitution of $\dot{q}_2^2$ from (A.7) in (A.6) yields

$$E^*\,P_1(q_1^*, q_2) + P_2(q_1^*, q_2) = u^* \tag{A.8}$$

where $P_1(q_1^*, q_2)$, $P_2(q_1^*, q_2)$ are defined in assumption 5. Differentiation of the above equation with respect to time results in

$$\frac{d}{dq_2}\left[kP_1(q_1^*, q_2) + P_2(q_1^*, q_2)\right]\dot{q}_2 = 0$$

Using assumption 5, we claim q_2 is constant. □

5.7.4 Nonoccurrence of Zeno Phenomenon

Impulsive braking results in $\dot{q}_1(t^+) = 0$ and the time derivative of (5.4.7) yields:

$$\ddot{V}(t^+) = -\ddot{q}_1^T(t^+)K_c\,\ddot{q}_1(t^+) < 0 \tag{A.9}$$

since K_c is positive-definite and $\ddot{q}_1(t^+) \neq 0$. If ε denotes the time for the trajectories to re-enter $\mathscr{Z}_1$, we can write

$$\dot{V}(t^+ + \varepsilon) = \dot{V}(t^+) + \int_{t^+}^{t^+ + \varepsilon} \ddot{V}(\tau)d\tau \tag{A.10}$$

Since, $\dot{V}(t^+ + \varepsilon) = \dot{V}(t^+) = 0$, and $\ddot{V}(t^+) \neq 0$, $\ddot{V}$ must change sign in $t \in (t^+, t^+ + \varepsilon)$. If ε is a small number, then the continuity of $\ddot{V}$ in the interval $[t^+, t^+ + \varepsilon]$ implies:

$$|\ddot{V}(t^+)| = \mathscr{O}(\varepsilon) \tag{A.11}$$

Using (A.9) and (A.11), we get

$$\|\ddot{q}_1(t^+)\| \leqslant \sqrt{\frac{|\ddot{V}(t^+)|}{\lambda_{min}(K_c)}} = \mathscr{O}(\varepsilon^{1/2}) \tag{A.12}$$

where $\lambda_{min}(K_c)$ is the smallest eigenvalue of K_c. Integrating $\ddot{q}_1$ with respect to time and using (A.12), we get

$$\|\dot{q}_1(t^+ + \varepsilon)\| \leqslant \int_{t^+}^{t^+ + \varepsilon} \|\ddot{q}_1(\tau)\|d\tau = \mathscr{O}(\varepsilon^{3/2}) \tag{A.13}$$

Let us now assume that Zeno phenomenon occurs. Then, the time interval between consecutive impulsive inputs, which is equal to ε, converges to zero and the trajectory of the system at time $t = (t^+ + \varepsilon)$ lies in the set $\mathscr{Z}_1$, where $\dot{q}_1(t^+ + \varepsilon) \neq 0$. Since $\varepsilon^{3/2}$ converges to zero faster than ε converges to zero, (A.13) implies that $\dot{q}_1(t^+ + \varepsilon)$ also converges to zero faster than ε converges to zero. This implies that the trajectory of the system does not lie in $\mathscr{Z}_1$ at $t = (t^+ + \varepsilon)$, and, by contradiction, proves the nonoccurence of the Zeno phenomenon.

5.7.5 Well-posedness of Switching Times

5.7.5.1 Background

Let $\psi(t,0,x_0)$ denote the solution of the continuous-time dynamics in (5.3.15a) for $0 \leqslant t \leqslant t_1^-$ starting from the initial condition $x(0) = x_0$ at time $t = 0$. If and when the trajectory reaches $\mathscr{Z}$ at t_1, the states are instantaneously transferred to $x(t_1^+) = x(t_1^-) + f_d[x(t_1^-)]$, according to the resetting in (5.3.17). The trajectory $x(t)$, $t_1^+ \leqslant t \leqslant t_2^-$, is then given by $\psi(t,t_1^+,x(t_1^+))$, and so on. The resetting times are well-posed if the following conditions are satisfied [101, pg.13]:

1. If $x(t) \in \bar{\mathscr{Z}} \backslash \mathscr{Z}$, then there exists $\varepsilon > 0$ such that, for all $0 < \delta < \varepsilon$,

$$\psi(t+\delta,t,x(t)) \notin \mathscr{Z}$$

2. If $x(t_k^-) \in \partial\mathscr{Z} \cap \mathscr{Z}$, then there exists $\varepsilon > 0$ such that, for all $0 \leqslant \delta < \varepsilon$,

$$\psi(t_k^+ + \delta, t_k^+, x(t_k^-) + f_d[x(t_k^-)]) \notin \mathscr{Z}$$

Condition (1) ensures that when the system trajectory reaches the closure of the set $\mathscr{Z}$, the trajectory must be directed away from $\mathscr{Z}$. Condition (2) ensures that when the trajectory intersects $\mathscr{Z}$, it instantaneously exists $\mathscr{Z}$.

5.7.5.2 Proof

Consider the set $\mathscr{Z}_1$ defined in (5.4.3b). If $x(t) \in \bar{\mathscr{Z}}_1 \backslash \mathscr{Z}_1$, then $\dot{q}_1(t) = 0$, which implies $\dot{V}(t) = 0$. Differentiating (5.4.7) with respect to time and substituting $\dot{q}_1(t) = 0$, we get $\ddot{V}(t) = -\ddot{q}_1^T(t) K_c \ddot{q}_1(t) < 0$. Since $\dot{V}(t) = 0$ and $\ddot{V}(t) < 0$, it follows $\lim_{\varepsilon \to 0^+} \dot{V}(t+\varepsilon) < 0$. Using (5.4.8), $[A + Bu]^T K_c \dot{q}_1(t+\varepsilon) > 0$, the trajectory of the system is directed away from $\mathscr{Z}_1$ after it reaches the closure of $\mathscr{Z}_1$. This implies condition (1) is satisfied for $\mathscr{Z}_1$. It can be shown that

$$\partial\mathscr{Z}_1 \cap \mathscr{Z}_1 = \{[A(q,\dot{q}) + B(q)u]^T K_c \dot{q}_1 = 0, \dot{q}_1 \neq 0\}$$

If $x(t_k^-) \in \partial\mathscr{Z}_1 \cap \mathscr{Z}_1$, impulsive braking is applied. This results in $\dot{q}_1(t_k^+) = 0$, which implies $x(t_k^+) \notin \mathscr{Z}_1$. Thus the trajectory instantaneously exists $\mathscr{Z}_1$ after intersecting $\mathscr{Z}_1$ and condition (2) is satisfied for $\mathscr{Z}_1$.

Now consider the set $\mathscr{Z}_2 \triangleq \{q_2 = -3\pi/2, \dot{q}_2 < 0\}$, which was defined after (5.3.17). If $x(t) \in \bar{\mathscr{Z}}_2 \backslash \mathscr{Z}_2$ *i.e.*, $x(t) \in \{q_2 = -3\pi/2, \dot{q}_2 = 0\}$. Then, if $\lim_{\varepsilon \to 0^+} \dot{q}_2(t+\varepsilon) \geqslant 0$, then it follows from the definition of $\mathscr{Z}_2$ that $x(t+\varepsilon) \notin \mathscr{Z}_2$. Alternatively, if $\lim_{\varepsilon \to 0^+} \dot{q}_2(t+\varepsilon) < 0$, then coordinate resetting occurs and $q_2(t+\varepsilon) = \pi/2 \to x(t+\varepsilon) \notin \mathscr{Z}_2$. Thus condition (1) is satisfied for $\mathscr{Z}_2$. Condition (2) is trivially satisfied for $\mathscr{Z}_2$ since $\partial\mathscr{Z}_2 \cap \mathscr{Z}_2$ is an empty set.

Similar to the set $\mathscr{Z}_2$, it can be shown that conditions (1) and (2) are satisfied for the set $\mathscr{Z}_3 \triangleq \{q_2 = \pi/2, \dot{q}_2 > 0\}$. Since conditions (1) and (2) are satisfied individually for $\mathscr{Z}_1$, $\mathscr{Z}_2$, $\mathscr{Z}_3$, they are satisfied for $\mathscr{Z} = \mathscr{Z}_1 \cup \mathscr{Z}_2 \cup \mathscr{Z}_3$. □

5.7.6 Quasi-Continuous Dependence Property

5.7.6.1 Background

Let $s(t,0,x_0)$ denote the solution of the hybrid dynamical system in (5.3.15a) and (5.3.15b) for $t \geqslant 0$ starting from the initial condition $x(0) = x_0$ at time $t = 0$. Let $\mathscr{T}_{x_0} \triangleq [0,\infty)\backslash\{t_1(x_0), t_2(x_0), \cdots\}$ denote all times except the discrete instants at which impulsive inputs are applied or coordinate resetting occurs. We now state the following assumption [101, Assumption 2.1, pg.27]:

Assumption 3. *Consider the hybrid dynamical system in (5.3.15). For every $x_0 \in \mathscr{D}$ and for every $\varepsilon > 0$ and $t \in \mathscr{T}_{x_0}$, there exists $\delta(\varepsilon, x_0, t) > 0$ such that if $\|x_0 - y\| < \delta(\varepsilon, x_0, t)$, $y \in \mathscr{D}$, then $\|s(t,0,x_0) - s(t,0,y)\| < \varepsilon$.*

The above assumption is a generalization of the standard continuous dependence property for dynamical systems with continuous flows to dynamical systems with left-continuous flows. We now state a proposition that provides sufficient conditions for satisfying Assumption 3 [101, Proposition 2.1, pg.32]:

Proposition 1. *Consider the hybrid dynamical system in (5.3.15) and suppose that conditions (1) and (2) in section 5.7.5.1 are satisfied; then the system in (5.3.15) satisfies Assumption 3 if for all* $x_0 \in \mathscr{D}$, $0 \leqslant t_1(x_0) < \infty$, $t_1(x_0)$ *is continuous, and* $\lim_{k\to\infty} t_k(x_0) \to \infty$.

5.7.6.2 Proof

Our domain $\mathscr{D}$ was defined in section 5.3.3 as the open set where $q_2 \in (a,b)$, $a < -3\pi/2$, $b > \pi/2$. If $q_2(0) \in (a,-3\pi/2] \cup [\pi/2,b)$, we can reset q_2 to satisfy (5.4.2) since q_2 corresponds to a revolute joint. From (5.3.15) we know that $x_0 \notin \mathscr{Z}$. This implies that $t_1(x_0) > 0$. Furthermore, $t_1(x_0)$ is a continuous function of x_0 since the system is described by continuous-time dynamics (ordinary differential equations) over the interval $t \in [0,t_1)$. Also, as shown in section 5.7.4, Zeno phenomenon does not occur. Thus $\lim_{k\to\infty} t_k(x_0) \to \infty$. □

5.7.7 Verification of Assumption 2 for Tiptoebot and Rotary Pendulum

Tiptoebot: It can be seen from (5.5.2) and (5.5.4) that all elements of the mass matrix are bounded and the potential energy is lower bounded. It can also be seen from (5.5.2) that M_{12} and M_{22} are only functions of q_1. Therefore P_1 in (A.8), defined earlier in assumption 5, is not a function of q_2. Since $\mathscr{F}$ in (5.5.4) is a function of both q_1 and q_2, it can be easily shown that $(dP_2/dq_2) \neq 0$. Thus assumption 5 holds.

Rotary Pendulum: It can be seen from (5.6.2) and (5.6.4) that all elements of the mass matrix are bounded and the potential energy is lower bounded. It can also be seen from (5.6.2) and (5.6.4) that the mass matrix and potential energy are independent of $q_1 = \phi$. Therefore

$$\begin{aligned}&\frac{d}{d\theta}\left[kP_1(\theta) + P_2(\theta)\right]\\ =&\frac{d}{d\theta}\left[\frac{\gamma_3}{\gamma_2}\cos\theta\left(2E^* - 3\gamma_4\sin\theta\right)\right] \neq 0\end{aligned}$$

Thus assumption 5 holds.

CHAPTER 6

ORBITAL STABILIZATION USING VIRTUAL HOLONOMIC CONSTRAINTS AND IMPULSE CONTROLLED POINCARÉ MAPS

6.1 Introduction

The problem of orbital stabilization of underactuated mechanical systems with one passive degree-of-freedom (DOF) is revisited in this chapter. The system dynamics is presented in section 6.2 and the results in [62] are utilized to design a continuous controller that can enforce the VHC such that the resulting zero dynamics is Euler-Lagrange. A periodic orbit is selected on the constraint manifold and a method for orbital stabilization is presented in section 6.3. To stabilize the orbit, a Poincaré section is defined at a point on the orbit and the return map is linearized about the fixed point; this results in a $2n-1$ dimensional discrete linear time-invariant (LTI) system. To control this system and stabilize the orbit, impulsive inputs are applied when the system trajectory crosses the Poincaré section. The controllability of the orbit can be verified by simply checking the controllability of the linear system. This is simpler than the approach in [3, 65, 66] where controllability is verified numerically along the orbit for most systems. Since the system is LTI, the control design involves constant gains that can be computed off-line. Compared to the methods proposed earlier [3, 63, 65, 66], where periodic Ricatti equations have to be solved, our method has lower computational cost and complexity. Since impulsive inputs are used to control the Poincaré map, the dynamics of the closed-loop system can be described by the Impulse Controlled Poincaré Map (ICPM). The simplicity and generality of the ICPM approach to orbital stabilization is demonstrated using the examples of the 2-DOF cart-pendulum in section 6.4 and the 3-DOF tiptoebot in section 6.5.

6.2 Problem Formulation

6.2.1 System Dynamics

Consider an n DOF underactuated system with one passive DOF, where the passive DOF is a revolute joint. Let q, $q \triangleq \left[q_1^T \; q_2\right]^T$, denote the generalized coordinates, where $q_1 \in R^{n-1}$ and $q_2 \in S^1$, $S^1 = R$ modulo 2π, are the coordinates of the active and passive DOFs. The configuration space of the system is denoted by $\mathbb{Q}^n$, $\mathbb{Q}^n \in R^{n-1} \times S^1$. The Lagrangian of the system can be written as

$$L(q,\dot{q}) = \frac{1}{2}\dot{q}^T M(q)\,\dot{q} + \mathscr{F}(q)$$

In the equation above, $M(q) \in R^{n\times n}$ denotes the symmetric, positive-definite mass matrix, partitioned as

$$M(q) = \left[\begin{array}{c|c} M_{11}(q) & M_{12}(q) \\ \hline M_{12}^T(q) & M_{22}(q) \end{array}\right]$$

where $M_{11} \in R^{(n-1)\times(n-1)}$, $M_{22} \in R$ and $\mathscr{F}(q)$ is the potential energy of the system. The Euler-Lagrange equation of motion can be written as follows

$$M_{11}(q)\,\ddot{q}_1 + M_{12}(q)\,\ddot{q}_2 + h_1(q,\dot{q}) = u \tag{6.2.1a}$$

$$M_{12}^T(q)\,\ddot{q}_1 + M_{22}(q)\,\ddot{q}_2 + h_2(q,\dot{q}) = 0 \tag{6.2.1b}$$

where $u \in R^{n-1}$ is the control input, and $[h_1^T, h_2]^T$ is the vector of Coriolis, centrifugal and gravity forces. In compact form, (6.2.1a) and (6.2.1b) can be rewritten as

$$\ddot{q}_1 = A(q,\dot{q}) + B(q)u \tag{6.2.2a}$$

$$\ddot{q}_2 = C(q,\dot{q}) + D(q)u \tag{6.2.2b}$$

where,

$$\begin{aligned} B(q) &= \left[M_{11} - (1/M_{22})M_{12}M_{12}^T\right]^{-1}, \quad A(q,\dot{q}) = (1/M_{22})B(q)\left[M_{12}h_2 - h_1 M_{22}\right] \\ D(q) &= -(1/M_{22})M_{12}^T B(q), \quad C(q,\dot{q}) = -(1/M_{22})\left[M_{12}^T A(q,\dot{q}) + h_2\right] \end{aligned} \tag{6.2.3}$$

Similar to [62], we make the following assumption:

Assumption 4. *For some $\bar{q} \triangleq [\bar{q}_1^T, \bar{q}_2]^T \in \mathbb{Q}^n$, the mass matrix $M(q)$ and the potential energy $\mathscr{F}(q)$ are even with respect to $\bar{q}$,* i.e.*,*

$$M(\bar{q}+q) = M(\bar{q}-q), \quad \mathscr{F}(\bar{q}+q) = \mathscr{F}(\bar{q}-q)$$

6.2.2 Imposing Virtual Holonomic Constraints (VHC)

A holonomic constraint enforced by feedback is referred to as VHC. The current and the next subsection summarizes relevant results from [62]. For a wide class of mechanical systems, a comprehensive discussion on VHC can be found in [62], [85].

A VHC for (6.2.1) is described by the relation $\rho(q) = 0$ where, $\rho : \mathbb{Q}^n \to R^{n-1}$ is smooth and $\text{rank}[J_q(\rho)] = n-1$ for all $q \in \rho^{-1}(0)$. Here, $J_q(\rho)$ is the Jacobian of ρ with respect to q. The VHC is stabilizable if there exists a smooth feedback $u_c(q,\dot{q})$ that asymptotically stabilizes the set

$$\mathscr{C} = \{(q,\dot{q}) : \rho(q) = 0,\ J_q(\rho)\dot{q} = 0\} \tag{6.2.4}$$

The set $\mathscr{C}$, which is referred to as the constraint manifold, is controlled invariant [62]. For the system described by (6.2.1), the set $\mathscr{C}$ is the tangent bundle of $\rho^{-1}(0)$, which is a closed embedded submanifold of $\mathbb{Q}^n$ of codimension $(n-1)$ [110, Def. 4.2].

An important goal of this work is to generate repetitive motion, which can be described by closed orbits. Consequently, $\rho^{-1}(0)$ must be a smooth and closed curve without any self-intersection. The VHC can be described as

$$\rho(q) = q_1 - \Phi(q_2) = 0 \tag{6.2.5}$$

where $\Phi : S^1 \to R^{n-1}$ is a smooth vector-valued function. The constraint manifold $\mathscr{C}$ in (6.2.4) can be expressed as:

$$\mathscr{C} = \left\{(q,\dot{q}) : q_1 = \Phi(q_2),\ \dot{q}_1 = \left[\frac{\partial \Phi}{\partial q_2}\right]\dot{q}_2\right\} \tag{6.2.6}$$

It should be noted that since $q_2 \in S^1$, $\Phi(q_2 + 2\pi) = \Phi(q_2)$ and $\rho^{-1}(0)$ is closed. Following the notion of odd VHC [62], we make another assumption.

Assumption 5. *For $\bar{q}$ which satisfies Assumption 4, $\Phi(q_2)$ is odd with respect to $\bar{q}_2$,* i.e.*,*

$$\Phi(\bar{q}_2 + q_2) = -\Phi(\bar{q}_2 - q_2)$$

To stabilize $\mathscr{C}$, we investigate the dynamics of $\rho(q)$; differentiating $\rho(q)$ twice with respect to time, we get

$$\ddot{\rho} = \ddot{q}_1 - \left[\frac{\partial \Phi}{\partial q_2}\right] \ddot{q}_2 - \left[\frac{\partial^2 \Phi}{\partial q_2^2}\right] \dot{q}_2^2 \tag{6.2.7}$$

Substitution of $\ddot{q}_1$ and $\ddot{q}_2$ from (6.2.2a) and (6.2.2b) in (6.2.7) yields

$$\ddot{\rho} = A - \left[\frac{\partial^2 \Phi}{\partial q_2^2}\right] \dot{q}_2^2 - \left[\frac{\partial \Phi}{\partial q_2}\right] C + \left[B - \left[\frac{\partial \Phi}{\partial q_2}\right] D\right] u \tag{6.2.8}$$

The following choice of linearizing control

$$u_c = \left[B - \left[\frac{\partial \Phi}{\partial q_2}\right] D\right]^{-1} \left[-A + \left[\frac{\partial^2 \Phi}{\partial q_2^2}\right] \dot{q}_2^2 + \left[\frac{\partial \Phi}{\partial q_2}\right] C - k_p \rho - k_d \dot{\rho}\right] \tag{6.2.9}$$

where k_p and k_d are positive definite matrices, results in

$$\ddot{\rho} + k_d \dot{\rho} + k_p \rho = 0 \tag{6.2.10}$$

This implies that $\lim_{t \to \infty} \rho(t) \to 0$ exponentially and u_c in (6.2.9) stabilizes the VHC in (6.2.5). If the initial conditions are chosen such that $\rho(0) = \dot{\rho}(0) = 0$, u_c in (6.2.9) enforces the VHC and the constraint manifold $\mathscr{C}$ is controlled invariant.

Remark 10. *For u_c in (6.2.9) to be well-defined, the matrix $[B - (\partial \Phi / \partial q_2) D]$ must be invertible. It can be shown that $[B - (\partial \Phi / \partial q_2) D]$ is invertible iff $M_{12}^T (\partial \Phi / \partial q_2) + M_{22} \neq 0$. This is also a necessary and sufficient condition for the VHC in (6.2.5) to be regular; since the VHC in (6.2.5) is in parametric form, this is also a necessary and sufficient condition for $\mathscr{C}$ to be stabilizable - see proposition 3.2 of [62].*

6.2.3 Zero Dynamics and Periodic Orbits

On the constraint manifold $\mathscr{C}$, the dynamics of the system satisfies $\rho(q) \equiv 0$; this implies

$$q_1 = \Phi(q_2),\ \dot{q}_1 = \left[\frac{\partial \Phi}{\partial q_2}\right] \dot{q}_2,\ \ddot{q}_1 = \left[\frac{\partial^2 \Phi}{\partial q_2^2}\right] \dot{q}_2^2 + \left[\frac{\partial \Phi}{\partial q_2}\right] \ddot{q}_2 \tag{6.2.11}$$

Substitution of q_1, $\dot{q}_1$ and $\ddot{q}_1$ from (6.2.11) in (6.2.1b) provides the zero dynamics, which can be expressed in the following form

$$\ddot{q}_2 = \alpha_1(q_2) + \alpha_2(q_2)\dot{q}_2^2 \tag{6.2.12}$$

It was shown in [3, 62, 83, 84] that the equation above has an integral of motion of the form

$$\begin{aligned} E(q_2,\dot{q}_2) &= (1/2)\mathscr{M}(q_2)\dot{q}_2^2 + \mathscr{P}(q_2) \\ \mathscr{M}(q_2) &= exp\left(-2\int_0^{q_2}\alpha_2(\tau)d\tau\right), \quad \mathscr{P}(q_2) = -\int_0^{q_2}\alpha_1(\tau)\mathscr{M}(\tau)\,d\tau \end{aligned} \tag{6.2.13}$$

where $\mathscr{M}(q_2)$ represents the mass and $\mathscr{P}(q_2)$ represents the potential energy of the reduced system in (6.2.12). Since both Assumption 4 and 5 are satisfied, the zero dynamics represents an Euler-Lagrange system with the Lagrangian[1] equal to $(1/2)\mathscr{M}(q_2)\dot{q}_2^2 - \mathscr{P}(q_2)$.

Since Assumptions 1 and 2 hold, the zero dynamics in (6.2.12) is similar to the dynamics of a simple pendulum [62] and its qualitative properties can be described by the potential energy $\mathscr{P}(q_2)$. Let $\mathscr{P}_{min}$ and $\mathscr{P}_{max}$ denote the minimum and maximum values of $\mathscr{P}$. If an energy level set is denoted by $E(q_2,\dot{q}_2) = c$, then $c \in (\mathscr{P}_{min}, \mathscr{P}_{max})$ corresponds to a periodic orbit where the sign of $\dot{q}_2$ changes periodically and $c > \mathscr{P}_{max}$ corresponds to an orbit where the sign of $\dot{q}_2$ does not change [62].

6.2.4 Problem Statement

Since the zero dynamics in (6.2.12) has an Euler-Lagrange structure, there cannot exist any non-trivial isolated periodic orbit - this follows from the Poincaré-Lyapunov-Liouville-Arnol'd theorem [62, 85, 111]. A direct implication of this theorem is that the reduced dynamics possesses a dense set of closed orbits that are stable, but not asymptotically stable. For a desired repetitive motion, the corresponding orbit must be stabilized. Consider the desired closed orbit $\mathscr{O}_d$, defined as follows:

$$\mathscr{O}_d = \{q, \dot{q} \in \mathscr{C} : E(q_2,\dot{q}_2) = c_d\}, \quad c_d > \mathscr{P}_{min} \tag{6.2.14}$$

[1] Assumptions 4 and 5 provide necessary and sufficient conditions for the reduced system to be Euler-Lagrange - the proof of this result can be found in [62, 85].

Let x, $x \triangleq [q^T, \dot{q}^T]^T$, denote the states of the system in (6.2.1). We define an ε-neighborhood of $\mathscr{O}_d$ by

$$U_\varepsilon = \{x \in \mathbb{Q}^n \times R^n : dist(x, \mathscr{O}_d) < \varepsilon\}$$

$$dist(x, \mathscr{O}_d) \triangleq \inf_{y \in \mathscr{O}_d} \|x - y\|$$

We now define stability of the orbit $\mathscr{O}_d$ from [112].

Definition 1. *The orbit $\mathscr{O}_d$ in (6.2.14) is*

- *stable, if for every $\varepsilon > 0$, there is a $\delta > 0$ such that $x(0) \in U_\delta \implies x(t) \in U_\varepsilon$, $\forall t \geqslant 0$.*
- *asymptotically stable if it is stable and δ can be chosen such that $\lim_{t\to\infty} dist(x(t), \mathscr{O}_d) = 0$.*

The control u_c in (6.2.9) asymptotically stabilizes $\mathscr{C}$ but does not asymptotically stabilize $\mathscr{O}_d$. If $q, \dot{q} \in \mathscr{O}_d$, u_c enforces the VHC and trajectories stay on $\mathscr{O}_d$; however, a perturbation of the states will cause the trajectories to converge to a different orbit on $\mathscr{C}$. The objective of this work is to utilize the control u_c in (6.2.9), which was designed to stabilize $\mathscr{C}$, together with impulsive inputs to stabilize $\mathscr{O}_d$ directly, that lies on $\mathscr{C}$.

6.3 Main Result: Stabilization of $\mathscr{O}_d$

6.3.1 Poincaré Map

The system in (6.2.1) with $u = u_c$ defined in (6.2.9), has the state-space representation

$$\dot{x} = f(x) \tag{6.3.1}$$

The stability characteristics of periodic orbits can be studied using Poincaré maps [113]. To this end, we define the Poincaré section Σ of $\mathscr{O}_d$ as follows[2]:

$$\Sigma = \{x \in \mathbb{Q}^n \times R^n : q_2 = q_2^*, \dot{q}_2 \geqslant 0\} \tag{6.3.2}$$

[2]Since the periodic orbit $\mathscr{O}_d$ can pass through $q_2 = q_2^*$ with both positive and negative velocity $\dot{q}_2$, the condition $\dot{q}_2 \geqslant 0$ implicitly assumes that Σ intersects the periodic orbit $\mathscr{O}_d$ at a single point. In the definition of Σ in (6.3.2), $\dot{q}_2 \geqslant 0$ can be replaced with $\dot{q}_2 \leqslant 0$ without any loss of generality.

where q_2^* is a constant. Let z, $z \triangleq [q_1^T, \dot{q}^T]^T \in R^{(2n-1)}$, denote the states of the system on Σ. The Poincaré map $\mathbb{P} : \Sigma \to \Sigma$ is obtained by following trajectories of z from one intersection with Σ to the next. Let t_k, $k = 1, 2, \cdots$ denote the time of the k-th intersection and $z(k) = z(t_k)$. Then, $z(k+1)$ can be described with the help of the map $\mathbb{P}$

$$z(k+1) = \mathbb{P}[z(k)] \tag{6.3.3}$$

The point of intersection of Σ and $\mathscr{O}_d$ is the fixed point of $\mathbb{P}$ denoted by z^*; it satisfies the following relation

$$z^* = \mathbb{P}(z^*) \tag{6.3.4}$$

The stability characteristics of the orbit $\mathscr{O}_d$ can be studied by investigating the stability properties of z^*, which is an equilibrium point of the discrete-time system in (6.3.3); this can be done by linearizing the map $\mathbb{P}$ about z^*. For $z(k) = z^* + \nu$, where $\|\nu\|$ is a small number, we can write

$$z(k+1) = \mathbb{P}(z^* + \nu) = \mathbb{P}(z^*) + [\nabla_z \mathbb{P}(z)]_{z=z^*} [z(k) - z^*] + O(\|\nu\|^2) \tag{6.3.5}$$

Using $\mathbb{P}(z^*) = z^*$ from (6.3.4) and neglecting higher-order terms in $\|\nu\|$, the above equation can be written as

$$\begin{aligned} e(k+1) &= \mathscr{A}\, e(k) \\ e(k) \triangleq z(k) - z^*, &\quad \mathscr{A} \triangleq [\nabla_z \mathbb{P}(z)]_{z=z^*} \end{aligned} \tag{6.3.6}$$

The stability properties of z^* is governed by the eigenvalues of $\mathscr{A}$, which are referred to as the Floquet multipliers of $\mathscr{O}_d$ [113]. If the Floquet multipliers lie inside the unit circle, $\mathscr{O}_d$ is exponentially stable - see Theorem 7.3 of [112]. From our discussion in section 6.2.4 we know that the desired orbit $\mathscr{O}_d$ is not asymptotically stable, *i.e.*, not all eigenvalues of $\mathscr{A}$ lie inside the unit circle. To asymptotically stabilize the orbit, *i.e.*, to asymptotically stabilize z^*, we design an impulsive controller in the next subsection.

6.3.2 Impulse Controlled Poincaré Map (ICPM)

To asymptotically stabilize the desired orbit $\mathscr{O}_d$, our controller in (6.2.9) is modified as follows

$$u = u_c + u_{\mathscr{I}} \tag{6.3.7}$$

where $u_{\mathscr{I}}$ is an impulsive input which is applied only when $x(t) \in \Sigma$. The dynamics of the system, with $u_{\mathscr{I}}$ as the new input, can be written as

$$M_{11}(q)\,\ddot{q}_1 + M_{12}(q)\,\ddot{q}_2 + \bar{h}_1(q,\dot{q}) = u_{\mathscr{I}} \tag{6.3.8a}$$

$$M_{12}^T(q)\,\ddot{q}_1 + M_{22}(q)\,\ddot{q}_2 + h_2(q,\dot{q}) = 0 \tag{6.3.8b}$$

where $\bar{h}_1 \triangleq (h_1 - u_c)$. Impulsive inputs cause discontinuous changes in the generalized velocities while there is no change in the generalized coordinates. On the Poincaré section Σ, the jump in velocities can be computed by integrating (6.3.8) as follows [86]:

$$\begin{bmatrix} M_{11} & M_{12} \\ M_{12}^T & M_{22} \end{bmatrix} \begin{bmatrix} \Delta\dot{q}_1 \\ \Delta\dot{q}_2 \end{bmatrix} = \begin{bmatrix} \mathscr{I} \\ 0 \end{bmatrix}, \quad \mathscr{I} \triangleq \int_0^{\Delta t} u_{\mathscr{I}}\, dt \tag{6.3.9}$$

In the above equation, Δt is the infinitesimal interval of time for which $u_{\mathscr{I}}$ is active, $\mathscr{I} \in R^{n-1}$ is the impulse of the impulsive input, and $\Delta\dot{q}_1$ and $\Delta\dot{q}_2$ are defined as

$$\Delta\dot{q}_1 \triangleq (\dot{q}_1^+ - \dot{q}_1^-), \qquad \Delta\dot{q}_2 \triangleq (\dot{q}_2^+ - \dot{q}_2^-) \tag{6.3.10}$$

where $\dot{q}^-$ and $\dot{q}^+$ are the velocities immediately before and after application of $u_{\mathscr{I}}$. Since the system is underactuated, the jump in the passive velocity $\dot{q}_2$ is dependent on the jumps in the active velocity $\dot{q}_1$; this relationship is described by the $(n-1)$ dimensional impulse manifold [6,23], which can be obtained from (6.3.9):

$$\mathscr{I}_{\mathrm{M}} = \{\dot{q}_1^+, \dot{q}_2^+ \mid \Delta\dot{q}_2 = -(1/M_{22})M_{12}^T\,\Delta\dot{q}_1\} \tag{6.3.11}$$

Since impulsive inputs can cause the system states to move on Σ, we exploit this property to design a feedback law that asymptotically stabilizes z^*, *i.e.*, asymptotically stabilizes $\mathscr{O}_d$. The control

input applied at t_k is denoted by $\mathscr{I}(k)$[3]. The dynamics of the impulse controlled system in (6.3.3) can be described by the map

$$z(k+1) = \mathbb{P}[z(k), \mathscr{I}(k)] \tag{6.3.12}$$

where $\mathscr{I}(k) = 0$ if $z(k) = z^*$[4]. By linearizing the above map about the fixed point $z = z^*$ and $\mathscr{I} = 0$, we get

$$\begin{aligned} e(k+1) &= \mathscr{A}\, e(k) + \mathscr{B}\, \mathscr{I}(k) \\ \mathscr{A} &\triangleq \left[\nabla_z \mathbb{P}(z, \mathscr{I})\right]_{z=z^*, \mathscr{I}=0}, \quad \mathscr{B} \triangleq \left[\nabla_{\mathscr{I}} \mathbb{P}(z, \mathscr{I})\right]_{z=z^*, \mathscr{I}=0} \end{aligned} \tag{6.3.13}$$

where $\mathscr{A} \in R^{(2n-1)\times(2n-1)}$ and $\mathscr{B} \in R^{(2n-1)\times(n-1)}$ can be obtained numerically. Since $\mathscr{A}$ is not Hurwitz (see discussion in the last sub-section), we make the following proposition to exponentially stabilize $\mathscr{O}_d$:

Proposition 2. *If the pair $\{\mathscr{A}, \mathscr{B}\}$ is stabilizable, the orbit $\mathscr{O}_d$ can be exponentially stabilized locally using the discrete impulsive feedback*

$$\mathscr{I}(k) = \mathscr{K}\, e(k) \tag{6.3.14}$$

where the matrix $\mathscr{K}$ is chosen such that $(\mathscr{A} + \mathscr{B}\mathscr{K})$ is Hurwitz.

Remark 11. *The matrices $\mathscr{A}$ and $\mathscr{B}$ depend on the continuous controller in (6.2.9), and hence on the choice of controller gains k_p and k_d. Thus, the stabilizability of the pair $\{\mathscr{A}, \mathscr{B}\}$ depends on the choice of k_p and k_d.*

The above approach to stabilization, which we refer to as the impulse controlled Poincaré map (ICPM) approach, is explained with the help of the schematic in Fig.6.1. The desired orbit $\mathscr{O}_d$ is shown in red and it intersects the Poincaré section Σ at the fixed point z^*. A trajectory starting from an arbitrary initial condition, shown by the point ①, intersects Σ at ②. The impulsive input in

[3] As long as Δt is sufficiently small, the effect of the impulsive input $u_{\mathscr{I}}$ depends solely on the value of $\mathscr{I}$ - see (6.3.9). Thus $\mathscr{I}$ can be viewed as the control input.

[4] If the system trajectory is passing through z^*, the trajectory is evolving on $\mathscr{O}_d$, which lies on $\mathscr{C}$. Since $\mathscr{I} = 0$, the invariance of $\mathscr{O}_d$ is guaranteed solely by the continuous controller u_c in (6.2.9).

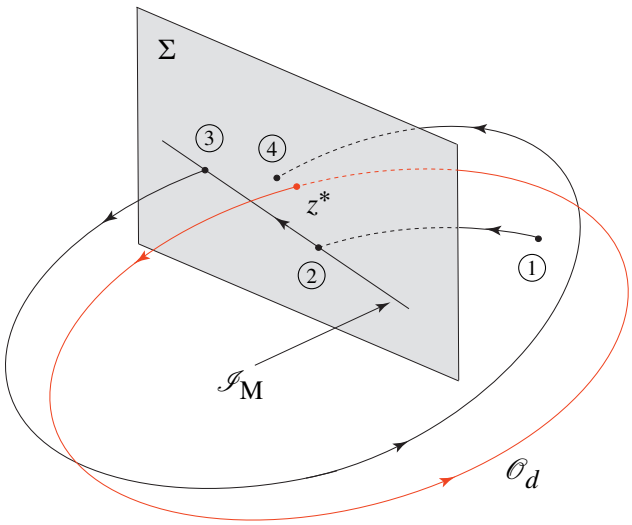

Figure 6.1: Schematic of ICPM approach to orbital stabilization.

(6.3.14) moves the configuration of the system from ② to ③ along the impulse manifold $\mathscr{I}_{\mathrm{M}}$. The point ③ lies on Σ since impulsive inputs cause no change in the position coordinates and $q_2 = q_2^*$ is maintained during the transition from ② to ③ along $\mathscr{I}_{\mathrm{M}}$. Furthermore, the condition $\dot{q}_2^+ \geqslant 0$ is satisfied since the impulsive controller in (6.3.14) is designed using linearization and ③ lies in some small neighborhood of z^* on Σ. Hereafter, the altered system trajectory evolves under the continuous control u_c and ④ denotes its next intersection with Σ. A series of ICPMs, similar to the map ② $\rightarrow$ ④ exponentially converge the intersection point of the trajectory on Σ to z^*.

Remark 12. *By stabilizing the constraint manifold $\mathscr{C}$, the continuous controller keeps the system trajectory close to $\mathscr{C}$. By stabilizing the fixed point, the impulsive controller works in tandem with the continuous controller to converge the system trajectory to $\mathscr{O}_d$, which lies on $\mathscr{C}$. Although the impulsive control inputs perturb the system trajectory intermittently, the trajectory converges to $\mathscr{O}_d$ on $\mathscr{C}$ due to the vanishing nature of the perturbations. While global exponential stability of $\mathscr{C}$ guarantees that $\mathscr{C}$ remains exponentially stable despite the perturbations, the magnitudes of the perturbations exponentially converge to zero as the intersection point of the trajectory with the Poincaré section converges to the fixed point.*

Remark 13. *In the ICPM approach, impulsive inputs create discontinuous jumps in the states of the system. Although the subsequent continuous-time dynamics remains unchanged, the discontinuous jumps in the states result in a change in the Poincaré map. This is different from the well-known OGY method of chaos control [114] where the continuous-time dynamics is altered by discretely changing system parameters on a Poincaré section. The OGY method has been utilized in control of dynamical systems described by Poincaré maps; examples include bipeds [115] and hopping robots [8].*

6.3.3 Implementation of Control Design

6.3.3.1 Numerical Computation of $\mathscr{A}$ and $\mathscr{B}$ matrices

Let δ_i, $i = 1,2,\cdots,2n-1$, denote the i-th column of $\varepsilon_1 I_{(2n-1)}$, where ε_1 is a small number and $I_{(2n-1)}$ is the identity matrix of size $(2n-1)$. If $\mathscr{A}_i$ denotes the i-th column of $\mathscr{A}$, then $\mathscr{A}_i$ can be numerically computed as follows:

$$\mathscr{A}_i = \frac{1}{\varepsilon_1}\left[\mathbb{P}(z^* + \delta_i) - z^*\right] \tag{6.3.15}$$

Let $Q \in R^{n\times(n-1)}$ and $S \in R^{(n-1)}$ be defined as follows:

$$Q \triangleq \left[\begin{array}{c} I_{(n-1)} \\ \hline 0_{1\times(n-1)} \end{array}\right], \quad S \triangleq \left[\begin{array}{c} 0_{(n-1)\times 1} \\ \hline M(q)^{-1}\eta_i \end{array}\right]$$

where $0_{i\times j}$ is a matrix of zeros of dimension $i \times j$, and η_i, $i = 1,2,\cdots,n-1$, denote the i-th column of $\varepsilon_2 Q$, where ε_2 is a small number. If $\mathscr{B}_i$ denotes the i-th column of $\mathscr{B}$, then $\mathscr{B}_i$ can be numerically computed as follows:

$$\mathscr{B}_i = \frac{1}{\varepsilon_2}\left\{\left[\mathbb{P}(z+S)\right]_{z=z^*} - z^*\right\} \tag{6.3.16}$$

The above expression has been obtained using (6.3.9).

Remark 14. *Numerical computation of $\mathscr{A}$ and $\mathscr{B}$ matrices is sensitive to the choice of ε_1 and ε_2. While ε_1 and ε_2 should be small, excessively small values can lead to numerical errors. For*

example, the eigenvalues of $\mathscr{A}$ may be found to lie inside the unit circle, which cannot be the case since orbits on $\mathscr{C}$ are not asymptotically stable.

6.3.3.2 Impulsive Input using High-Gain Feedback

Impulsive inputs are Dirac-delta functions and cannot be realized in real physical systems. Using singular perturbation theory [116], it was shown that continuous-time approximation of impulsive inputs can be carried out using high-gain feedback [23]; this has allowed implementation of impulsive control in physical systems using standard hardware [6, 25]. To obtain the expression for the high-gain feedback, we substitute (6.3.14) in (6.3.9) to get

$$\Delta \dot{q}_1(k) = B\,\mathscr{I}(k) = B\mathscr{K}\,e(k) \tag{6.3.17}$$

where B is defined in (6.2.3) and is evaluated at t_k; $\Delta\dot{q}_1(k)$ is the jump in the active velocities generated by the input $\mathscr{I}(k)$. From (6.3.10) and (6.3.17), the desired active joint velocities at t_k is

$$\dot{q}_1^{des}(k) = \dot{q}_1(k) + B\mathscr{K}\,e(k) \tag{6.3.18}$$

where $\dot{q}_1(k) = \dot{q}_1(t_k)$. To reach the desired velocities in a very short period of time, we use the high-gain feedback [6]

$$u_{hg} = B^{-1}\left[\frac{1}{\mu}\Lambda\left(\dot{q}_1^{des}(k) - \dot{q}_1\right) - \bar{A}\right] \tag{6.3.19}$$

which remains active for as along as $\|\dot{q}_1^{des}(k) - \dot{q}_1\| \geqslant \varepsilon_3$, where ε_3 is a small number. In (6.3.19), $\dot{q}_1^{des}$ is obtained from (6.3.18) and $\bar{A}$ is obtained from the expression for A in (6.2.3) by replacing h_1 with $\bar{h}_1$. Furthermore, $\Lambda \triangleq diag[\lambda_1 \quad \lambda_2 \quad \cdots \quad \lambda_{n-1}]$, where λ_i, $i = 1, 2, \cdots, n-1$ are positive numbers, and $\mu > 0$ is a small number.

6.4 Illustrative Example: Cart-Pendulum

6.4.1 System Dynamics and VHC

Consider the frictionless cart-pendulum system in Fig.6.2. The masses of the cart and pendulum are denoted by m_c and m_p, ℓ denotes the length of the pendulum, and g is the acceleration due to

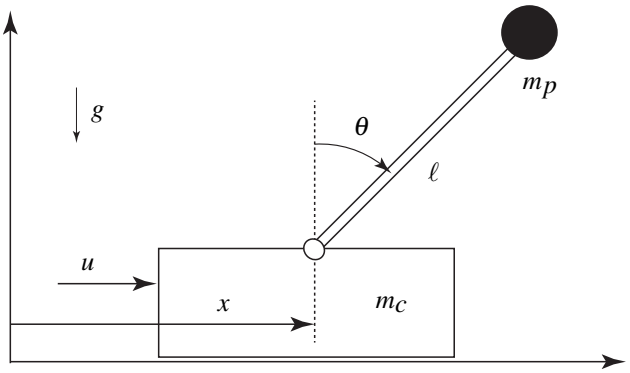

Figure 6.2: Inverted pendulum on a cart.

gravity. The control input u is the horizontal force applied on the cart. The cart position is denoted by x, $x \in R$, and the angular displacement of the pendulum, measured clock-clockwise with respect to the vertical, is denoted by θ, $\theta \in S^1$. We consider physical parameters of the system to be the same as those in [3]: $m_p = m_c = \ell = 1$. With the following definition

$$q = [q_1 \quad q_2]^T = [x \quad \theta]^T \tag{6.4.1}$$

and the potential energy of the system, given by

$$\mathscr{F} = \cos\theta \tag{6.4.2}$$

the equations of motion can be obtained as

$$\begin{bmatrix} 2 & \cos\theta \\ \cos\theta & 1 \end{bmatrix} \begin{bmatrix} \ddot{x} \\ \ddot{\theta} \end{bmatrix} - \begin{bmatrix} \sin\theta\,\dot{\theta}^2 \\ g\sin\theta \end{bmatrix} = \begin{bmatrix} u \\ 0 \end{bmatrix} \tag{6.4.3}$$

which is of the form in (6.2.1). The VHC in (6.2.5) is chosen as

$$\rho = x + 1.5\sin\theta = 0 \tag{6.4.4}$$

which is identical to that considered in [3]. It can be verified that the mass matrix in (6.4.3) and the choice of VHC in (6.4.4) satisfy Assumptions 4 and 5 for $\bar{q} = (0,\ 0)$. For the VHC in (6.4.4) to be stabilizable, Remark 10 provides the following condition that needs to be satisfied:

$$1 - 1.5\cos^2\theta \neq 0 \quad \Rightarrow \quad \theta \neq \pm 0.61\ rad \tag{6.4.5}$$

Clearly, the VHC in (6.4.4) is not regular and the corresponding constraint manifold is therefore not stabilizable. Since our control design requires the VHC to be regular, we cannot use the VHC in (6.4.4) with $\theta \in S^1$. However, by restricting the domain of θ to be $(-0.61, 0.61)$, it is possible to compare the performance of our control design with that presented in [3]. Through trial and error, the controller gains are chosen such that θ lies in the interval $(-0.61, 0.61)$.

6.4.2 Stabilization of VHC and $\mathscr{O}_d$

The ICPM approach relies on stabilization of both the constraint manifold $\mathscr{C}$, and the orbit $\mathscr{O}_d$ on $\mathscr{C}$. This is a distinctive difference between our approach and the approach in [3] where $\mathscr{O}_d$ is stabilized without stabilizing $\mathscr{C}$, *i.e.*, without enforcing the VHC. With the objective of enforcing the VHC, the gains k_p and k_d in (6.2.9) are chosen as follows:

$$k_p = 2, \quad k_d = 1 \tag{6.4.6}$$

We choose the desired orbit $\mathscr{O}_d$ to pass through the point:

$$(x,\ \theta,\ \dot{x},\ \dot{\theta}) = (0.0,\ 0.0,\ -0.675,\ 0.450) \tag{6.4.7}$$

which is approximately the desired orbit in [3] - see Fig.2 therein. For exponential stabilization of $\mathscr{O}_d$, we define the Poinacaré section

$$\Sigma = \{x \in \mathbb{Q}^2 \times R^2 \,:\, \theta = 0,\ \dot{\theta} \geqslant 0\} \tag{6.4.8}$$

The states of the system on Σ are

$$z = [\,x \quad \dot{x} \quad \dot{\theta}\,]^T$$

Since z^* lies on $\mathscr{O}_d$, using (6.4.7) and (6.4.8) we get

$$z^* = [0.0 \quad -0.675 \quad 0.450]^T$$

Using the values of $\varepsilon_1 = 0.02$ and $\varepsilon_2 = 0.01$, the matrices $\mathscr{A}$ and $\mathscr{B}$ in (6.3.15) and (6.3.16) are obtained as

$$\mathscr{A} = \begin{bmatrix} 0.115 & 0.435 & 0.600 \\ -0.510 & -0.640 & -2.465 \\ -0.145 & 0.215 & 1.325 \end{bmatrix}, \quad \mathscr{B} = \begin{bmatrix} -0.06 \\ 1.80 \\ -1.09 \end{bmatrix}$$

It can be verified that all eigenvalues of $\mathscr{A}$ do not lie inside the unit circle but the pair $\{\mathscr{A}, \mathscr{B}\}$ is controllable and satisfy Proposition 2. Using LQR design, the gain matrix $\mathscr{K}$ in (6.3.14) was obtained as

$$\mathscr{K} = \begin{bmatrix} 0.163 & 0.288 & 1.198 \end{bmatrix} \tag{6.4.9}$$

The eigenvalues of $(\mathscr{A} + \mathscr{B}\mathscr{K})$ are located at 0.13 and $-0.06 \pm 0.48i$; thus, the impulsive feedback in (6.3.14) exponentially stabilizes the desired orbit $\mathscr{O}_d$.

6.4.3 Simulation Results

The initial configuration of the system is taken from [3]:

$$[x \quad \theta \quad \dot{x} \quad \dot{\theta}] = [0.1 \quad 0.4 \quad -0.1 \quad -0.2]$$

For the controller gains in (6.4.6) and (6.4.9), simulation results for the ICPM are shown in Fig.6.3; ρ is plotted with time in Fig.6.3 (a) and the phase portrait of the pendulum is shown in Fig.6.3 (b). To show the convergence of system trajectories to $\mathscr{O}_d$, $\|e(k)\|_2$ is plotted with respect to k in Fig.6.3 (c). It can be seen from Fig.6.3 (a) that the system trajectories converge to the constraint manifold. To stabilize $\mathscr{O}_d$ on $\mathscr{C}$, the impulsive controller in (6.3.14) is implemented using the high-gain feedback in (6.3.19) with $\Lambda = 1$ and $\mu = 0.005$. It can be seen from the phase portrait in Fig.6.3 (b) that the pendulum trajectory converges exponentially to $\mathscr{O}_d$, shown in red. The effect of discrete impulsive feedback can be seen in Fig.6.3 (b) where $\dot{\theta}$ jumps when trajectories cross the Poincaré section Σ defined in (6.4.8). The system trajectories reach a close neighborhood of $\mathscr{O}_d$ in approximately 10 sec; this is comparable to the results in [3]. We now consider the following initial

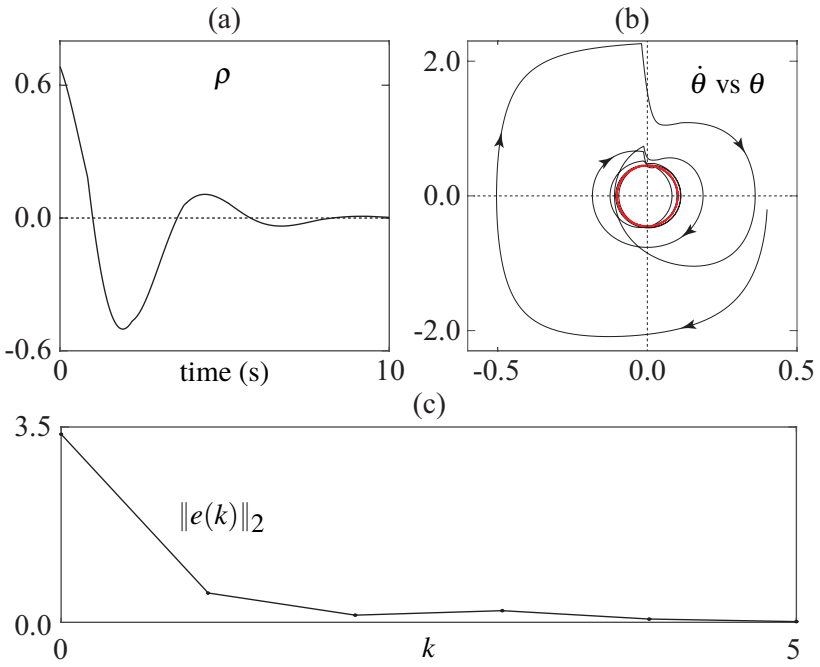

Figure 6.3: Orbital stabilization for the cart-pendulum system for the initial conditions in [3]: (a) plot of ρ with respect to time, (b) phase portrait of the pendulum, (c) plot of the norm of the error of the discrete-time system.

condition that lies far away from $\mathscr{O}_d$:

$$[x \quad \theta \quad \dot{x} \quad \dot{\theta}] = [0.0 \quad 0.0 \quad 0.0 \quad 0.0] \tag{6.4.10}$$

We used the same controller gains as that used in the previous simulation. It can be seen from the results in Fig.6.4 that $\mathscr{O}_d$ is asymptotically stabilized. For the same initial conditions in (6.4.10), the control design in [3] fails to converge the pendulum trajectory to $\mathscr{O}_d$. Several other initial conditions yielded similar results. While this may be indicative of a larger region of attraction of $\mathscr{O}_d$ with the ICPM approach than with the approach in [3], the region of attraction has to be estimated for both designs and compared before any conclusion can be drawn. To demonstrate the generality of the ICPM approach, we consider the three DOF tiptoebot, which is presented next.

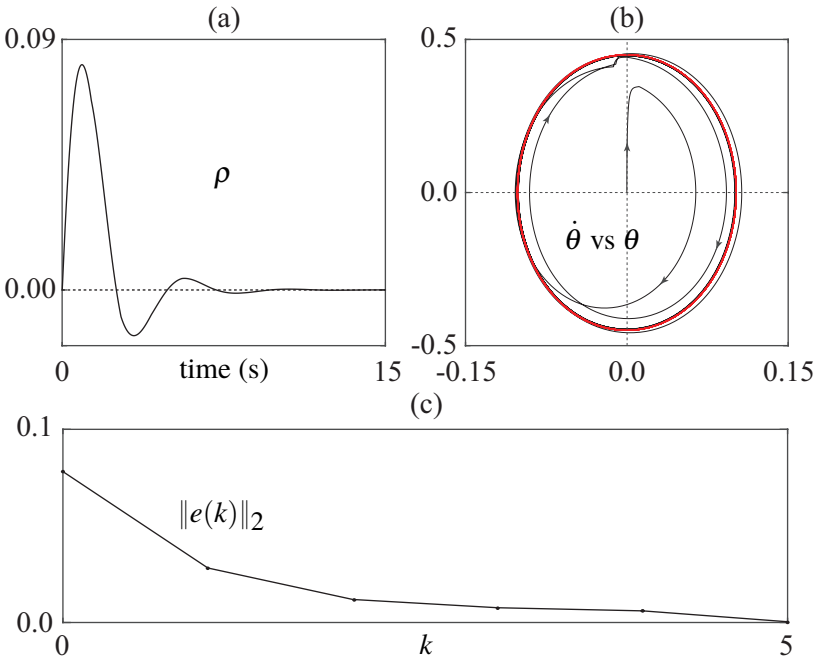

Figure 6.4: Orbital stabilization for the cart-pendulum system for the initial conditions in (6.4.10): (a) plot of ρ with respect to time, (b) phase portrait of the pendulum; $\mathscr{O}_d$ is shown in red, (c) plot of the norm of the error of the discrete-time system.

6.5 Illustrative Example - The Tiptoebot

6.5.1 System Description

Consider the three DOF tiptoebot [6]. Using the following definition for the joint angles and control inputs

$$q_1^T = [\ \theta_2 \quad \theta_3\ ]^T, \quad q_2 = \theta_1, \quad u = [\tau_2\ \tau_3]^T \tag{6.5.1}$$

Table 6.1: Tiptoebot lumped parameters in SI units

α_1	0.386	α_4	0.065	β_1	4.307
α_2	0.217	α_5	0.054	β_2	1.102
α_3	0.247	α_6	0.104	β_3	1.764

where $\theta_1 \in S^1$, $\theta_2, \theta_3 \in R$, the dynamics of the tiptoebot can be expressed in the form given in (2.2.1), where the components of the mass matrix and the potential energy are:

$$
\begin{aligned}
M_{11} &= \begin{bmatrix} \alpha_2+\alpha_3+2\alpha_5\cos\theta_3 & \alpha_3+\alpha_5\cos\theta_3 \\ \alpha_3+\alpha_5\cos\theta_3 & \alpha_3 \end{bmatrix} \\
M_{12} &= \begin{bmatrix} \alpha_2+\alpha_3+\alpha_4\cos\theta_2+2\alpha_5\cos\theta_3+\alpha_6\cos(\theta_2+\theta_3) \\ \alpha_3+\alpha_5\cos\theta_3+\alpha_6\cos(\theta_2+\theta_3) \end{bmatrix} \\
M_{22} &= \alpha_1+\alpha_2+\alpha_3+2\left[\alpha_4\cos\theta_2+\alpha_5\cos\theta_3+\alpha_6\cos(\theta_2+\theta_3)\right] \\
\mathscr{F} &= \beta_1\cos\theta_1+\beta_2\cos(\theta_1+\theta_2)+\beta_3\cos(\theta_1+\theta_2+\theta_3)
\end{aligned}
\tag{6.5.2}
$$

where α_i, $i = 1,2,\cdots,6$, and β_i, $i = 1,2,3$ are lumped physical parameters; their values are given in Table 6.1. It can be verified that Assumption 4 is satisfied for $\bar{q} = (0\ 0\ 0)^T$.

6.5.2 Imposing VHC and Selection of $\mathscr{O}_d$

The VHC in (6.2.5) is chosen as

$$
\rho = \begin{bmatrix} \rho_1 \\ \rho_2 \end{bmatrix} = \begin{bmatrix} \theta_2 + 2.0\,\theta_1 \\ \theta_3 - 0.1\,\theta_1 \end{bmatrix} = \begin{bmatrix} 0 \\ 0 \end{bmatrix} \tag{6.5.3}
$$

which satisfies Assumption 5 for $\bar{q} = (0\ 0\ 0)^T$. Also, it is stabilizable as it satisfies the condition in Remark 10. With the objective of enforcing the VHC, the gain matrices in (6.2.9) were chosen as

$$
k_p = \begin{bmatrix} 1.0 & 0.0 \\ 0.0 & 1.0 \end{bmatrix}, \quad k_d = \begin{bmatrix} 0.1 & 0.0 \\ 0.0 & 0.1 \end{bmatrix} \tag{6.5.4}
$$

The phase portrait of the zero dynamics in (6.2.12) is shown in Fig.6.5. It can be seen that the equilibrium $(\theta_1, \dot{\theta}_1) = (0,0)$ is a center, surrounded by a dense set of closed orbits. We choose the desired orbit $\mathscr{O}_d$ to be the one that passes through $(\theta_1, \dot{\theta}_1) = (0.0, 3.0)$.

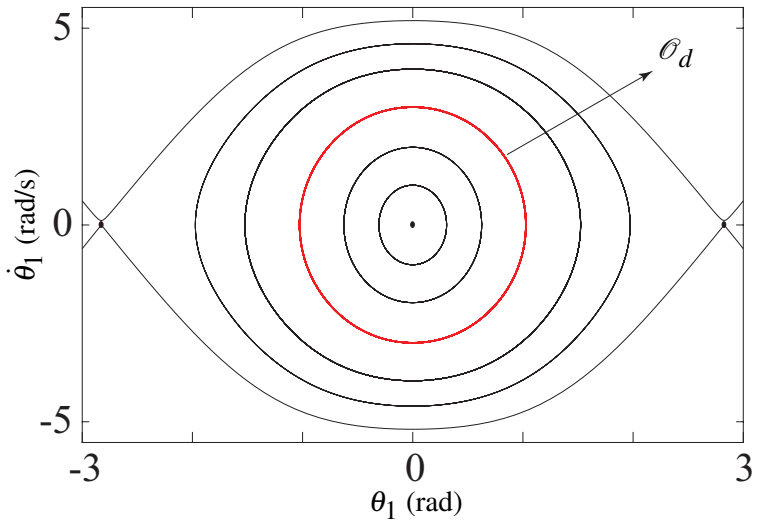

Figure 6.5: Phase portrait of tiptoebot zero dynamics. The desired orbit $\mathscr{O}_d$ is shown in red.

6.5.3 Stabilization of $\mathscr{O}_d$

We define the Poincaré section of $\mathscr{O}_d$ as follows

$$\Sigma = \{x \in \mathbb{Q}^3 \times R^3 \,:\, \theta_1 = 0,\ \dot{\theta}_1 \geqslant 0\} \tag{6.5.5}$$

The states on Σ are

$$z = [\theta_2 \quad \theta_3 \quad \dot{\theta}_1 \quad \dot{\theta}_2 \quad \dot{\theta}_3]^T$$

Substituting $(\theta_1, \dot{\theta}_1) = (0.0, 3.0)$ in (6.5.3) and its derivative gives

$$z^* = [0.0 \quad 0.0 \quad 3.0 \quad -6.0 \quad 0.3]^T \tag{6.5.6}$$

Using the values of $\varepsilon_1 = 0.01$ and $\varepsilon_2 = 0.004$, the matrices $\mathscr{A}$ and $\mathscr{B}$ in (6.3.15) and (6.3.16) were obtained as

$$\mathscr{A} = \begin{bmatrix} -0.380 & -0.080 & 1.530 & 0.800 & 0.050 \\ 0.000 & -0.460 & -0.080 & -0.003 & 0.730 \\ 1.230 & 1.890 & 6.120 & 2.770 & 4.050 \\ -3.210 & -3.770 & -13.360 & -6.090 & -8.100 \\ 0.120 & -0.560 & 0.670 & 0.280 & 0.100 \end{bmatrix}$$

$$\mathscr{B} = \begin{bmatrix} 1.525 & -3.700 & -17.700 & 34.325 & 0.875 \\ 4.875 & -8.650 & 22.650 & -43.850 & -0.325 \end{bmatrix}^T$$

All eigenvalues of $\mathscr{A}$ do not lie inside the unit circle but the pair $\{\mathscr{A},\mathscr{B}\}$ is controllable and satisfy Proposition 2. Using LQR, the gain matrix $\mathscr{K}$ in (6.3.14) is obtained as

$$\mathscr{K} = \begin{bmatrix} 0.028 & 0.024 & 0.197 & 0.094 & 0.138 \\ -0.034 & -0.051 & 0.116 & -0.049 & -0.055 \end{bmatrix} \tag{6.5.7}$$

The eigenvalues of $(\mathscr{A}+\mathscr{B}\mathscr{K})$ are located at 0.14, $-0.47 \pm 0.73i$ and $-0.12 \pm 0.56i$; thus $\mathscr{O}_d$ is exponentially stable under the impulsive feedback.

6.5.4 Simulation Results

The initial configuration of the tiptoebot is taken as

$$[\theta_1 \;\; \theta_2 \;\; \theta_3 \;\; \dot{\theta}_1 \;\; \dot{\theta}_2 \;\; \dot{\theta}_3] = [-0.1 \;\; 0.2 \;\; 0.05 \;\; 3.3 \;\; -6.0 \;\; 0.4]$$

For the controller gains in (6.5.4) and (6.5.7), simulation results of the ICPM approach are shown in Fig.6.6. The plots of ρ_1, ρ_2, $\dot{\rho}_1$ and $\dot{\rho}_2$ with time are shown in Figs.6.6 (a)-(d); it can be seen that the continuous controller u_c in (6.2.9) stabilizes the constraint manifold $\mathscr{C}$. The phase portrait of the passive joint θ_1 is shown in Fig.6.6 (e) for $0 \leqslant t \leqslant 20$ s and Fig.6.6 (f) for $t > 20$ s. To asymptotically stabilize the desired orbit $\mathscr{O}_d$, shown in red in both Figs.6.6 (e) and (f), the impulsive controller in (6.3.14) is implemented using the high-gain feedback in (6.3.19); Λ was chosen to be an identity matrix and μ was chosen as 0.0001. To show the convergence of system trajectories to $\mathscr{O}_d$, $\|e(k)\|_2$ is plotted with respect to k in Fig.6.6 (e). It can be seen that for large values of k, $\|e(k)\|_2 \to 0$; this implies that $\mathscr{O}_d$ is exponentially stable.

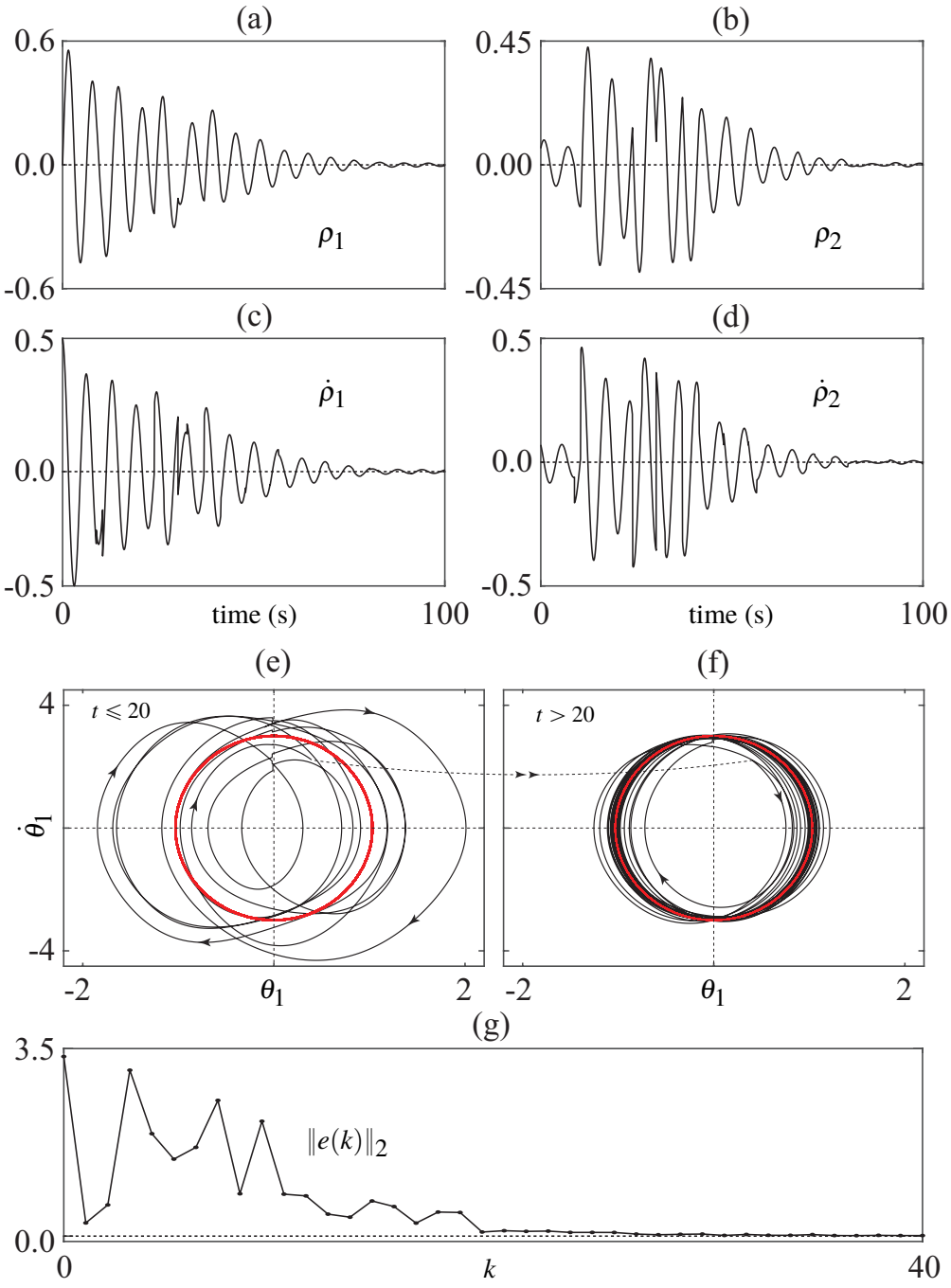

Figure 6.6: Orbital stabilization for the tiptoebot using ICPM: (a) and (b) provide plots of ρ_1 and ρ_2, (c) and (d) provide plots of $\dot{\rho}_1$ and $\dot{\rho}_2$, (e) and (f) provide the phase portrait of the passive joint, (g) provides the norm of the error for the discrete-time system.

CHAPTER 7

CONCLUSION AND FUTURE WORK

In this work we investigated several problems where impulsive inputs were exploited to stabilize equlibria and orbits of underactuated robotic systems. In chapter 2, using both simulations and experiments, we demonstrated a method for stabilizing the equilibria of underactuated systems from configurations lying outside the estimate of their region of attraction. The method, known as the IMM, uses impulsive inputs to force the configuration of the system to move inside the region of attraction along a manifold of dimension equal to the number of active degrees-of-freedom. Justified by singular perturbation theory [23], the impulsive inputs were implemented using high-gain feedback. In the general case, the region of attraction is not known and the IMM requires an estimate of the region, which is computed off-line. If the initial configuration of the system is outside this estimate, the IMM can be used if the impulse manifold intersects this region. The likelihood of intersection improves if the size of the estimated region is large, and therefore, a procedure for obtaining large estimates was developed by combining the SOS and trajectory reversing methods. For a fixed order of the stabilizing controller, the SOS method maximizes the estimate of the region of attraction and this estimate is further enlarged using an algorithm (CHART) based on the method of trajectory reversing. The advantage of combining the two methods was demonstrated in simulations using a three-link underactuated system (Tiptoebot) and in experiments with a pendubot. For both systems, it was shown that the impulse manifold may intersect the enlarged estimate but not the estimate obtained using the SOS method, implying that the CHART enhances the utility of the IMM. In another simulation with the Tiptoebot, it was shown that the combination of SOS, CHART and IMM requires a lower magnitude of the impulsive input compared to the combination of SOS and IMM. In addition to providing a large estimate, the CHART makes it possible to generalize the results to higher-dimensional systems. In the literature, several algorithms have been proposed for estimating the region of attraction using trajectory reversing, but the CHART is the only algorithm that has been demonstrated for a system with as

many as six states. Earlier experimental results [23] relied on finding the boundary of the region of attraction through trial and error and used the IMM to move the configuration of the system from a point lying immediately outside the region to inside the region. The experimental results presented here are more meaningful and practical as they are based on an estimate of the region of attraction and points chosen outside this region are not very close to the boundary. Experimental results of stabilization from two different initial conditions using the SOS, CHART and IMM were presented. In one of the experiments, through trial and error, the initial condition was purposely chosen to lie outside the region of attraction; it was shown that the equilibrium could not be stabilized with the SOS controller alone but was stabilized by the combination of SOS, CHART and IMM. Future work will investigate the possibility of extending the approach to multiple impulsive inputs. This will be useful in situations where the impulse manifold does not intersect the estimated region of attraction: a first impulsive input may be used to take the configuration closer to the boundary of the estimate and additional impulses may be applied to move the system configuration inside the region in future time. Of course, this would require real-time computation of the intersection of the impulse manifold with the boundary of the estimated region. Compared to the SOS method, which provides an analytical representation of the estimate of the region of attraction, the trajectory reversing method provides a numerical representation and will involve higher computational cost. Considering the fact that the trajectory reversing method provides the opportunity to enlarge the estimate, it is necessary to investigate the trade-off between computational cost and size of the estimate for real-time applications.

In chapter 3, rest-to-rest maneuvers of the inertia-wheel pendulum was studied in the framework of impulsive control. Assuming a set of discrete impulsive inputs, optimal sequences were designed to minimize their infinity-norm. It was shown analytically that a sequence with an odd number of inputs is less optimal than the two adjacent sequences with even number of inputs. Analytical and simulation results with two inputs were used to explain the high wheel velocities and large continuous torques associated with methods that attempt to take the pendulum directly to its desired configuration and minimize overshoot. Implementation of impulsive control using high-

gain feedback also results in large torques but they act over short intervals of time; therefore, feasibility of impulsive control is determined by the peak torque rating of the actuator, which is always larger than the continuous torque rating. It was shown that the number of impulsive inputs can be increased to not exceed the peak torque rating of the actuator; this, of-course, increases the time required for swing-up. Simulation results for swing-up showed similarities between the optimal trajectories and the trajectories obtained using the energy-based controllers. Future work will investigate the possibility of extending the method presented here to other underactuated systems.

Using impulsive forces only, the problem of juggling a devil-stick was presented in chapter 4. Impulsive forces were applied intermittently for juggling the stick between two symmetric configurations. A dynamic model of the devil-stick and a control design for the juggling task was presented for the first time. The control inputs are the impulse of the impulsive force and its point of application on the stick. The control action is event-based and the inputs are applied only when the stick has the orientation of one of the two symmetric configurations. The dynamics of the devilstick due to the control action and torque-free motion under gravity is described by two Poincaré sections; the symmetric configurations are fixed points of these sections. A coordinate transformation is used to exploit the symmetry and convert the problem into that of stabilization of a single fixed point. A dead-beat controller is designed to convert the nonlinear system into a controllable linear discrete-time system with input constraints. LQR and MPC methods are used to design the control inputs and achieve symmetric juggling. The LQR method has a closed-form solution and is easier to implement but requires trial and error to satisfy the input constraints. The MPC method has no closed-form solution as it is obtained by solving an optimization problem online. However, the optimization problem directly takes into account the input constraint. The computational cost of the MPC method, which can be a concern for many problems, is not a concern for the juggling problem since the time between consecutive control actions is relatively large.Simulation results validate both control designs and demonstrate non-prehensile manipulation solely using impulsive forces. Our future work will focus on robotic juggling; this includes design of experimental hardware,

feedback compensation of energy losses due to inelastic collisions between the devil-stick and hand sticks, and motion planning and control of the robot end-effector for generating the impulsive forces designed by the control algorithms.

In chapter 5, a hybrid control strategy was presented for orbital stabilization of underactuated systems with one passive DOF. The orbit is defined with the help of a Lyapunov-like function that has been commonly used in the literature. Unlike existing energy-based methods, that have relied on continuous control inputs alone, our control strategy uses continuous control inputs and intermittent impulsive brakings. The continuous control is designed to make the time derivative of the Lyapunov-like function negative semi-definite. When this condition cannot be enforced, the impulsive inputs are invoked. This results in negative jumps in the Lyapunov-like function and guarantees its negative semi-definiteness under continuous control for some finite time interval. Thus, a combination of continuous and impulsive inputs guarantees monotonic convergence of the system trajectories to the desired orbit, which can be periodic, or non-periodic as in the case of homoclinic orbits, depending on the choice of desired energy. More importantly, it allows us to develop a general framework for energy-based orbital stabilization, which is an important contribution of this work. A set of conditions, that impose constraints on the choice of controller gains, have to be satisfied for applicability of the control strategy. These conditions are easily satisfied by systems commonly studied in the literature such as the pendubot, acrobot, inertia-wheel pendulum, and pendulum on a cart. In this work, the hybrid control strategy was demonstrated in a three-DOF underactuated system using simulations and the two-DOF rotary pendulum using experiments. In experiments, impulsive brakings were not applied by the motor; instead, they were applied by a friction brake mounted co-axially with the motor shaft. This requires additional hardware but there are two important advantages of using the brake. In physical systems, impulsive inputs are implemented using high-gain feedback, which can result in actuator saturation. Since our impulsive control strategy requires the active velocities to be reduced to zero, a brake is a natural choice and it eliminates the possibility of motor torque saturation. The advantage of using a brake is also manifested in the time required for orbital stabilization. A comparison of our approach with

an approach in the literature shows significant reduction in the time for convergence for the same set of initial conditions.

Finally, the control design for stabilization of VHC based orbits was presented in chapter 6. Repetitive motion in underactuated systems are typically designed using VHCs. A VHC results in a family of periodic orbits and stabilization of a desired orbit is an important problem. A hybrid control design is presented to stabilize a VHC-generated periodic orbit for underactuated systems with one passive DOF. A continuous controller is first designed to enforce the VHC and stabilize the corresponding constraint manifold. The desired orbit on the constraint manifold is exponentially stabilized by applying the continuous inputs together with impulsive inputs that are periodically applied on a Poincaré section. The impulsive inputs alter the Poincaré map and this impulse controlled Poincaré map (ICPM) is described by a discrete LTI system. The problem of orbital stabilization is thus simplified to exponential stabilization of the fixed point of the ICPM. The controllability of the system can be easily verified and the control design can be easily carried out using standard techniques such as pole-placement and LQR. The identification of the linear system and computation of the controller gains are performed off-line. The complexity and computational cost of the ICPM approach is less than existing methods as it eliminates the need for on-line solution of a periodic Ricatti equation. The ICPM approach is demonstrated using standard cart-pendulum system; its applicability to higher-dimensional systems is demonstrated using the tiptoebot. Future work will focus on gait stabilization of legged robots and experimental validation.

BIBLIOGRAPHY

BIBLIOGRAPHY

[1] R. Olfati-Saber, Global stabilization of a flat underactuated system: the inertia wheel pendulum, in: Proc. IEEE Conference on Decision and Control, Vol. 4, 2001, pp. 3764–3765.

[2] M. W. Spong, P. Corke, R. Lozano, Nonlinear control of the reaction wheel pendulum, Automatica 37 (11) (2001) 1845–1851.

[3] A. Shiriaev, J. W. Perram, C. Canudas-de Wit, Constructive tool for orbital stabilization of underactuated nonlinear systems: Virtual constraints approach, IEEE Transactions on Automatic Control 50 (8) (2005) 1164–1176.

[4] M. W. Spong, D. J. Block, The pendubot: A mechatronic system for control research and education, in: Decision and Control, 1995., Proceedings of the 34th IEEE Conference on, Vol. 1, IEEE, 1995, pp. 555–556.

[5] M. W. Spong, The swing up control problem for the acrobot, IEEE Control Systems 15 (1) (1995) 49–55.

[6] N. Kant, R. Mukherjee, D. Chowdhury, H. K. Khalil, Estimation of the region of attraction of underactuated systems and its enlargement using impulsive inputs, IEEE Transactions on Robotics 35 (3) (2019) 618–632.

[7] F. Plestan, J. W. Grizzle, E. R. Westervelt, G. Abba, Stable walking of a 7-dof biped robot, IEEE Transactions on Robotics and Automation 19 (4) (2003) 653–668.

[8] F. B. Mathis, R. Mukherjee, Apex height control of a two-mass robot hopping on a rigid foundation, Mechanism and Machine Theory 105 (2016) 44–57.

[9] R. Ronsse, P. Lefevre, R. Sepulchre, Rhythmic feedback control of a blind planar juggler, IEEE Transactions on Robotics 23 (4) (2007) 790–802.

[10] R. Goebel, R. G. Sanfelice, A. R. Teel, Hybrid dynamical systems, IEEE Control Systems 29 (2) (2009) 28–93.

[11] Y. Aoustin, D. T. Romero, C. Chevallereau, S. Aubin, Impulsive control for a thirteen-link biped, in: 9th IEEE International Workshop on Advanced Motion Control, 2006, pp. 439–444.

[12] S. Weibel, G. W. Howell, J. Baillieul, Control of single-degree-of-freedom Hamiltonian systems with impulsive inputs, in: Proc. 35th IEEE Conference on Decision and Control, Vol. 4, 1996, pp. 4661–4666.

[13] A. M. Bloch, N. E. Leonard, J. E. Marsden, Controlled Lagrangians and the stabilization of mechanical systems. i. the first matching theorem, IEEE Transactions on Automatic Control 45 (12) (2000) 2253–2270.

[14] A. M. Bloch, D. E. Chang, N. E. Leonard, J. E. Marsden, Controlled Lagrangians and the stabilization of mechanical systems. ii. potential shaping, IEEE Transactions on Automatic Control 46 (10) (2001) 1556–1571.

[15] R. Ortega, M. W. Spong, F. Gómez-Estern, G. Blankenstein, Stabilization of a class of underactuated mechanical systems via interconnection and damping assignment, IEEE Transactions on Automatic Control 47 (8) (2002) 1218–1233.

[16] D. Auckly, L. Kapitanski, W. White, Control of nonlinear underactuated systems, Communications on Pure and Applied Mathematics 53 (3) (2000) 354–369.

[17] I. Fantoni, R. Lozano, M. W. Spong, Energy based control of the pendubot, IEEE Transactions on Automatic Control 45 (4) (2000) 725–729.

[18] M. Zhang, T.-J. Tarn, Hybrid control of the pendubot, IEEE/ASME Transactions on Mechatronics 7 (1) (2002) 79–86.

[19] T. Albahkali, R. Mukherjee, T. Das, Swing-up control of the pendubot: An impulse-momentum approach, IEEE Transactions on Robotics 25 (4) (2009) 975–982.

[20] R. Jafari, F. B. Mathis, R. Mukherjee, Swing-up control of the acrobot: An impulse-momentum approach, in: Proc. American Control Conference, 2011, pp. 262–267.

[21] J. Lee, R. Mukherjee, H. K. Khalil, Output feedback stabilization of inverted pendulum on a cart in the presence of uncertainties, Automatica 54 (2015) 146–157.

[22] F. Andreev, D. Auckly, S. Gosavi, L. Kapitanski, A. Kelkar, W. White, Matching, linear systems, and the ball and beam, Automatica 38 (12) (2002) 2147 – 2152.

[23] R. Jafari, F. B. Mathis, R. Mukherjee, H. Khalil, Enlarging the region of attraction of equilibria of underactuated systems using impulsive inputs, IEEE Transactions on Control Systems Technology 24 (1) (2016) 334–340.

[24] F. B. Mathis, R. Jafari, R. Mukherjee, Efficient swing-up of the acrobot using continuous torque and impulsive braking, in: Proc. American Control Conference, 2011, pp. 268–273.

[25] F. B. Mathis, R. Jafari, R. Mukherjee, Impulsive actuation in robot manipulators: Experimental verification of pendubot swing-up, IEEE/ASME Transactions on Mechatronics 19 (4) (2014) 1469–1474.

[26] D. Davidson, S. A. Bortoff, Enlarge your region of attraction using high-gain feedback, in: Proc. IEEE Conference on Decision and Control, 1994, pp. 634–639.

[27] C. Reboulet, C. Champetier, A new method for linearizing non-linear systems: the pseudo-linearization, International Journal of Control 40 (4) (1984) 631–638.

[28] T. Hu, Z. Lin, Composite quadratic Lyapunov functions for constrained control systems, IEEE Transactions on Automatic Control 48 (3) (2003) 440–450.

[29] R. Bakhtiari, M. Yazdanpanah, Designing a linear controller for polynomial systems with the largest domain of attraction via LMIs, in: Proc. IEEE International Conference on Control and Automation, Vol. 1, 2005, pp. 449–453.

[30] A. I. Zečević, D. D. Šiljak, Estimating the region of attraction for large-scale systems with uncertainties, Automatica 46 (2) (2010) 445–451.

[31] P. A. Parrilo, Structured semidefinite programs and semialgebraic geometry methods in robustness and optimization, Ph.D. thesis, California Institute of Technology (2000).

[32] W. Tan, A. Packard, Stability region analysis using polynomial and composite polynomial Lyapunov functions and sum-of-squares programming, IEEE Transactions on Automatic Control 53 (2) (2008) 565–571.

[33] U. Topcu, A. Packard, P. Seiler, Local stability analysis using simulations and sum-of-squares programming, Automatica 44 (10) (2008) 2669–2675.

[34] U. Topcu, A. K. Packard, P. Seiler, G. J. Balas, Robust region-of-attraction estimation, IEEE Transactions on Automatic Control 55 (1) (2010) 137–142.

[35] A. Majumdar, A. A. Ahmadi, R. Tedrake, Control design along trajectories with sums of squares programming, in: Proc. IEEE International Conference on Robotics and Automation, 2013, pp. 4054–4061.

[36] A. Majumdar, R. Tedrake, Funnel libraries for real-time robust feedback motion planning, The International Journal of Robotics Research 36 (8) (2017).

[37] R. Genesio, A. Vicino, New techniques for constructing asymptotic stability regions for nonlinear systems, IEEE Transactions on Circuits and Systems 31 (6) (1984) 574–581.

[38] R. Genesio, M. Tartaglia, A. Vicino, On the estimation of asymptotic stability regions: State of the art and new proposals, IEEE Transactions on Automatic Control 30 (8) (1985) 747–755.

[39] M. Loccufier, E. Noldus, A new trajectory reversing method for estimating stability regions of autonomous nonlinear systems, Nonlinear dynamics 21 (3) (2000) 265–288.

[40] F. Hamidi, H. Jerbi, W. Aggoune, M. Djemai, M. N. Abdkrim, Enlarging region of attraction via LMI-based approach and genetic algorithm, in: Proc. IEEE International Conference on Communications, Computing and Control Applications, 2011, pp. 1–6.

[41] D. Chowdhury, N. Kant, R. Mukherjee, H. K. Khalil, Enlarging the region of attraction of equilibria of underactuated systems using sum of squares and impulse manifold method, in: Proc. American Control Conference, 2017, pp. 893–898.

[42] N. Kant, D. Chowdhury, R. Mukherjee, H. K. Khalil, An algorithm for enlarging the region of attraction using trajectory reversing, in: Proc. American Control Conference, 2017, pp. 4171–4176.

[43] M. Ryalat, D. S. Laila, A simplified ida-pbc design for underactuated mechanical systems with applications, European Journal of Control 27 (2016) 1–16.

[44] N. Qaiser, N. Iqbal, A. Hussain, Stabilization of non-linear inertia wheel pendulum system using a new dynamic surface control based technique, in: IEEE International Conference on Engineering of Intelligent Systems, 2006, pp. 1–6.

[45] A. Khoroshun, Stabilization of the upper equilibrium position of a pendulum by spinning an inertial flywheel, International applied mechanics 52 (5) (2016) 547–556.

[46] A. Zhang, C. Yang, S. Gong, J. Qiu, Nonlinear stabilizing control of underactuated inertia wheel pendulum based on coordinate transformation and time-reverse strategy, Nonlinear Dynamics 84 (4) (2016) 246702476.

[47] HNWpodcasts, Five easy devil stick tricks with instructions, https://www.youtube.com/watch?v=Z7Pv-p-nEYo, [Online; accessed 01-May-2020] (2013).

[48] N. Duinker, Devilstick tutorial - basic tricks to get you started, https://www.youtube.com/watch?v=MAuAtwZ7BF4, [Online; accessed 01-May-2020] (2015).

[49] H. Hirai, F. Miyazaki, Dynamic coordination between robots: Self-organized timing selection in a juggling-like ball-passing task, IEEE Transactions on Systems, Man, and Cybernetics, Part B (Cybernetics) 36 (4) (2006) 738–754.

[50] J. Kober, M. Glisson, M. Mistry, Playing catch and juggling with a humanoid robot, in: 12th IEEE-RAS International Conference on Humanoid Robots (Humanoids 2012), IEEE, 2012, pp. 875–881.

[51] A. Tornambe, Modeling and control of impact in mechanical systems: Theory and experimental results, IEEE Transactions on Automatic Control 44 (2) (1999) 294–309.

[52] K. M. Lynch, C. K. Black, Recurrence, controllability, and stabilization of juggling, IEEE Transactions on Robotics and Automation 17 (2) (2001) 113–124.

[53] A. Zavala-Rio, B. Brogliato, Direct adaptive control design for one-degree-of-freedom complementary-slackness jugglers, Automatica 37 (7) (2001) 1117–1123.

[54] B. Brogliato, M. Mabrouk, A. Z. Rio, On the controllability of linear juggling mechanical systems, Systems & control letters 55 (4) (2006) 350–367.

[55] R. Goebel, R. G. Sanfelice, A. R. Teel, Hybrid Dynamical Systems: modeling, stability, and robustness, Princeton University Press, 2012.

[56] M. W. Spong, Impact controllability of an air hockey puck, Systems & Control Letters 42 (5) (2001) 333–345.

[57] S. Schaal, C. G. Atkeson, Open loop stable control strategies for robot juggling, in: Proc. IEEE International Conference on Robotics and Automation, IEEE, 1993, pp. 913–918.

[58] R. G. Sanfelice, A. R. Teel, R. Sepulchre, A hybrid systems approach to trajectory tracking control for juggling systems, in: Decision and Control, 2007 46th IEEE Conference on, IEEE, 2007, pp. 5282–5287.

[59] S. Nakaura, Y. Kawaida, T. Matsumoto, M. Sampei, Enduring rotary motion control of devil stick, IFAC Proceedings Volumes 37 (13) (2004) 805–810.

[60] A. Shiriaev, A. Robertsson, L. Freidovich, R. Johansson, Generating stable propeller motions for devil stick, in: 3rd IFAC Workshop on Lagrangian and Hamiltonian Methods for Nonlinear Control, 2006, 2006.

[61] J. Zhao, M. W. Spong, Hybrid control for global stabilization of the cart–pendulum system, Automatica 37 (12) (2001) 1941–1951.

[62] M. Maggiore, L. Consolini, Virtual holonomic constraints for Euler- Lagrange systems, IEEE Transactions on Automatic Control 58 (4) (2013) 1001–1008.

[63] A. Mohammadi, M. Maggiore, L. Consolini, Dynamic virtual holonomic constraints for stabilization of closed orbits in underactuated mechanical systems, Automatica 94 (2018) 112–124.

[64] E. R. Westervelt, C. Chevallereau, J. H. Choi, B. Morris, J. W. Grizzle, Feedback Control of Dynamic Bipedal Robot Locomotion, CRC press, 2007.

[65] A. S. Shiriaev, L. B. Freidovich, A. Robertsson, R. Johansson, A. Sandberg, Virtual-holonomic-constraints-based design of stable oscillations of Furuta pendulum: Theory and experiments, IEEE Transactions on Robotics 23 (4) (2007) 827–832.

[66] L. Freidovich, A. Robertsson, A. Shiriaev, R. Johansson, Periodic motions of the pendubot via virtual holonomic constraints: Theory and experiments, Automatica 44 (3) (2008) 785–791.

[67] X. Xin, T. Yamasaki, Energy-based swing-up control for a remotely driven acrobot: Theoretical and experimental results, IEEE Transactions on Control Systems Technology 20 (4) (2012) 1048–1056.

[68] I. Fantoni, R. Lozano, M. Spong, Stabilization of the reaction wheel pendulum using an energy approach, in: European Control Conference (ECC), IEEE, 2001, pp. 2552–2557.

[69] R. Lozano, I. Fantoni, D. J. Block, Stabilization of the inverted pendulum around its homoclinic orbit, Systems & Control Letters (2000) 197–204.

[70] H. Oka, Y. Maruki, H. Suemitsu, T. Matsuo, Nonlinear control for rotational movement of cart-pendulum system using homoclinic orbit, International Journal of Control, Automation and Systems 14 (5) (2016) 1270–1279.

[71] I. Fantoni, R. Lozano, Stabilization of the Furuta pendulum around its homoclinic orbit, International Journal of Control 75 (6) (2002) 390–398.

[72] X. Xin, M. Kaneda, Swing-up control for a 3-dof gymnastic robot with passive first joint: design and analysis, IEEE Transactions on Robotics 23 (6) (2007) 1277–1285.

[73] H. K. Khalil, Nonlinear control, Prentice Hall, 2014.

[74] N. Kant, R. Mukherjee, H. K. Khalil, Stabilization of homoclinic orbits of two degree-of-freedom underactuated systems, in: 2019 American Control Conference (ACC), 2019.

[75] J. W. Grizzle, C. Chevallereau, R. W. Sinnet, A. D. Ames, Models, feedback control, and open problems of 3d bipedal robotic walking, Automatica 50 (8) (2014) 1955–1988.

[76] J. W. Grizzle, G. Abba, F. Plestan, Asymptotically stable walking for biped robots: Analysis via systems with impulse effects, IEEE Transactions on automatic control 46 (1) (2001) 51–64.

[77] C. Canudas-de Wit, On the concept of virtual constraints as a tool for walking robot control and balancing, Annual Reviews in Control 28 (2) (2004) 157–166.

[78] C. Chevallereau, G. Abba, Y. Aoustin, F. Plestan, E. R. Westervelt, C. Canudas-De-Wit, J. W. Grizzle, RABBIT: A testbed for advanced control theory, IEEE Control Systems Magazine 23 (5) (2003) 57–79.

[79] C. Chevallereau, J. W. Grizzle, C.-L. Shih, Asymptotically stable walking of a five-link underactuated 3-D bipedal robot, IEEE Trans. on Robotics 25 (1) (2009) 37–50.

[80] E. R. Westervelt, J. W. Grizzle, D. E. Koditschek, Hybrid zero dynamics of planar biped walkers, IEEE Transactions on Automatic Control 48 (1) (2003) 42–56.

[81] C. Canudas-de Wit, B. Espiau, C. Urrea, Orbital stabilization of underactuated mechanical systems, in: Proc. 15th IFAC World Congress, 2002.

[82] A. Mohammadi, E. Rezapour, M. Maggiore, K. Y. Pettersen, Maneuvering control of planar snake robots using virtual holonomic constraints, IEEE Trans. on Control Systems Technology 24 (3) (2015) 884–899.

[83] A. Shiriaev, A. Robertsson, J. Perram, A. Sandberg, Periodic motion planning for virtually constrained Euler-Lagrange systems, Systems & Control Letters 55 (11) (2006) 900–907.

[84] A. S. Shiriaev, L. B. Freidovich, S. V. Gusev, Transverse linearization for controlled mechanical systems with several passive degrees of freedom, IEEE Trans. on Automatic Control 55 (4) (2010) 893–906.

[85] A. Mohammadi, Virtual holonomic constraints for Euler-Lagrange control systems, Ph.D. thesis, University of Toronto (2016).

[86] L. L. Flynn, R. Jafari, R. Mukherjee, Active synthetic-wheel biped with torso, IEEE Transactions on Robotics 26 (5) (2010) 816–826.

[87] A. Majumdar, A. A. Ahmadi, R. Tedrake, Control and verification of high-dimensional systems with DSOS and SDSOS programming, in: Proc. 53rd IEEE Conference on Decision and Control, 2014, pp. 394–401.

[88] C. B. Barber, D. P. Dobkin, H. Huhdanpaa, The quickhull algorithm for convex hulls, ACM Transactions on Mathematical Software 22 (4) (1996) 469–483.

[89] J. D'Errico, Inhull, mathworks.com Updated on 06 Sep 2012 (March 2006).

[90] M. J, Analyze n-dimensional polyhedra in terms of vertices or (In)Equalities, mathworks.com Updated on 16 Sep 2015 (March 2011).

[91] M. Ester, H.-P. Kriegel, J. Sander, X. Xu, et al., A density-based algorithm for discovering clusters in large spatial databases with noise, in: Kdd, Vol. 96, 1996, pp. 226–231.

[92] Yarpiz, Dbscan clustering algorithm, mathworks.com 06 Sep 2015 (March 2011).

[93] N. Kant, R. Mukherjee, H. K. Khalil, Swing-up of the inertia wheel pendulum using impulsive torques, in: 2017 IEEE 56th Annual Conference on Decision and Control (CDC), IEEE, 2017, pp. 5833–5838.

[94] H. A. Toliyat, G. B. Kliman, Handbook of electric motors, Vol. 120, CRC press, 2004.

[95] N. Kant, R. Mukherjee, Impulsive dynamics and control of the inertia-wheel pendulum, IEEE Robotics and Automation Letters 3 (4) (2018) 3208–3215.

[96] S. Wiggins, Introduction to applied nonlinear dynamical systems and chaos, Vol. 2, Springer Science & Business Media, 2003.

[97] J. Guckenheimer, K. Hoffman, W. Weckesser, The forced Van der Pol equation i: The slow flow and its bifurcations, SIAM Journal on Applied Dynamical Systems 2 (1) (2003) 1–35.

[98] K. Bold, C. Edwards, J. Guckenheimer, S. Guharay, K. Hoffman, J. Hubbard, R. Oliva, W. Weckesser, The forced Van der Pol equation ii: Canards in the reduced system, SIAM Journal on Applied Dynamical Systems 2 (4) (2003) 570–608.

[99] P. J. Antsaklis, A. N. Michel, A Linear Systems Primer, Birkhauser, 2007.

[100] L. Wang, Model predictive control system design and implementation using MATLAB®, Springer Science & Business Media, 2009.

[101] W. M. Haddad, V. Chellaboina, S. G. Nersesov, Impulsive and hybrid dynamical systems, Princeton Series in Applied Mathematics (2006).

[102] B. Brogliato, R. Lozano, B. Maschke, O. Egeland, Dissipative Systems Analysis and Control, Springer, 2020.

[103] D. Liu, W. Guo, J. Yi, D. Zhao, Passivity-based-control for a class of underactuated mechanical systems, in: IEEE International Conference on Intelligent Mechatronics and Automation, 2004, pp. 50–54.

[104] B. Brogliato, Nonsmooth Mechanics. Models, Dynamics and Control, Springer Nature Switzerland AG, 2020.

[105] B. Brogliato, S. . Niculescu, P. Orhant, On the control of finite-dimensional mechanical systems with unilateral constraints, IEEE Transactions on Automatic Control 42 (2) (1997) 200–215.

[106] R. I. Leine, N. Van de Wouw, Stability and Convergence of Mechanical Systems with Unilateral Constraints, Vol. 36, Springer Science & Business Media, 2007.

[107] D. D. Bainov, P. S. Simeonov, Systems with Impulse Effect: Stability, Theory, and Applications, Ellis Horwood, 1989.

[108] R. G. Sanfelice, R. Goebel, A. R. Teel, Invariance principles for hybrid systems with connections to detectability and asymptotic stability, IEEE Transactions on Automatic Control 52 (12) (2007) 2282–2297.

[109] R. Ortega, J. A. L. Perez, P. J. Nicklasson, H. J. Sira-Ramirez, Passivity-based control of Euler-Lagrange systems: Mechanical, Electrical and Electromechanical Applications, Springer Science & Business Media, 2013.

[110] L. Consolini, A. Costalunga, M. Maggiore, A coordinate-free theory of virtual holonomic constraints, Journal of Geometric Mechanics 10 (4) (2018) 467–502.

[111] N. Nekhoroshev, The Poincaré-Lyapunov-Liouville-Arnol'd theorem, Functional Analysis and Its Applications 28 (1994) 128–129.

[112] H. K. Khalil, Nonlinear Systems, 2nd Edition, Prentice Hall, Upper Saddle River, NJ, 1996.

[113] S. H. Strogatz, Nonlinear dynamics and chaos: With applications to physics, biology, chemistry, and engineering, CRC Press, 2018.

[114] E. Ott, C. Grebogi, J. A. Yorke, Controlling chaos, Physical Review Letters 64 (11) (1990) 1196.

[115] J. Grizzle, E. Westervelt, C. Canudas-de Wit, Event-based PI control of an underactuated biped walker, in: 42nd Int. Conference on Decision and Control, Vol. 3, IEEE, 2003, pp. 3091–3096.

[116] P. Kokotović, H. K. Khalil, J. O'reilly, Singular perturbation methods in control: analysis and design, SIAM, 1999.